

UTILIZATION OF COLLOIDAL PRINCIPLES IN CARBON COATING OF
ELECTROACTIVE MATERIALS

A THESIS SUBMITTED TO
THE GRADUATE SCHOOL OF NATURAL AND APPLIED SCIENCES
OF
MIDDLE EAST TECHNICAL UNIVERSITY

BY

YASEMİN AŞKAR

IN PARTIAL FULFILLMENT OF THE REQUIREMENTS
FOR
THE DEGREE OF MASTER OF SCIENCE
IN
METALLURGICAL AND MATERIALS ENGINEERING

SEPTEMBER 2022

Approval of the thesis:

**UTILIZATION OF COLLOIDAL STABILIZATION PRINCIPLES IN
CARBON COATING OF ELECTROACTIVE MATERIALS**

submitted by **YASEMİN AŞKAR** in partial fulfillment of the requirements for the degree of **Master of Science in Metallurgical and Materials Engineering, Middle East Technical University** by,

Prof. Dr. Halil Kalıpçılar
Dean, Graduate School of **Natural and Applied Sciences**

Prof. Dr. Ali Kalkanlı
Head of the Department, **Met. and Mat. Eng., METU**

Assoc. Prof. Dr. Simge Çınar Aygün
Supervisor, **Metallurgical and Materials Eng., METU**

Prof. Dr. Bora Maviş
Co-Supervisor, **Mechanical Eng., Hacettepe University**

Examining Committee Members:

Prof. Dr. Mehmet Kadri Aydınol
Metallurgical and Materials Eng., METU

Assoc. Prof. Dr. Simge Çınar Aygün
Metallurgical and Materials Eng., METU

Assist. Prof. Dr. Irmak Sargın
Metallurgical and Materials Eng., METU

Assoc. Prof. Dr. Emre Büküşoğlu
Chemical Engineering, METU

Prof. Dr. Ziya Esen
Dept. of Inter-Curricular Courses, Çankaya University

Date: 01.09.2022

I hereby declare that all information in this document has been obtained and presented in accordance with academic rules and ethical conduct. I also declare that, as required by these rules and conduct, I have fully cited and referenced all material and results that are not original to this work.

Name Last name: Yasemin Aşkar

Signature:

ABSTRACT

UTILIZATION OF COLLOIDAL PRINCIPLES IN CARBON COATING OF ELECTROACTIVE MATERIALS

Aşkar, Yasemin

Master of Science, Metallurgical and Materials Engineering

Supervisor: Assoc. Prof. Dr. Simge Çınar Aygün

Co-Supervisor: Prof. Dr. Bora Maviş

September 2022, 130 pages

The increasing energy demand requires battery systems with high volumetric energy density, therefore one of the current aims is to maximize the amount of active material that can be loaded per unit volume. This situation is directly related to the particle agglomeration state and dispersible particles are required to achieve high volumetric energy density. Carbon coating, which is used to increase the electrical conductivity of active materials, also plays a significant role in the agglomeration of the particles. For this reason, in this thesis, it was aimed to develop a suitable carbon coating procedure in such a way that individual electroactive materials maintain their dispersibility. Herein, as a novel approach, colloidal principles and a proceeding pyrolysis step were used to synthesize dispersible particles with full carbon coverage.

LiFePO₄ (LFP) electroactive material was chosen as the model system. Individually dispersible LFP particles were produced with the polyol method. After zeta potential analyses on pristine LFP particles, CTAB (cetyltrimethylammonium bromide) was chosen as the surfactant and used as a carbon source for pyrolysis. The critical ratio of CTAB to LFP at which zeta potential reverses sign and stabilizes were determined

and a two-stage pyrolysis procedure was designed. The optimal carbon-coated individual particles produced in this process and bare LFP were compared in terms of their dispersibility, tap density, and electrochemical performance. The tap density of the pristine LFP ($1.11 \text{ g}\cdot\text{cm}^{-3}$) and carbon-coated LFP particles ($1.16 \text{ g}\cdot\text{cm}^{-3}$) was obtained quite similar. Results demonstrate the applicability of the zeta potential analysis-based approach utilized herein producing homogeneous carbon coating without any losses in tap density and dispersibility.

Keywords: Carbon Coating, Colloidal Stabilization, Dispersible Electroactive Material Synthesis, Lithium Iron Phosphate, Cetyltrimethylammonium Bromide

ÖZ

ELEKTROAKTİF MALZEMELERİN KARBON KAPLANMALARINDA KOLOİDAL İLKELERİN KULLANILMASI

Aşkar, Yasemin
Yüksek Lisans, Metalurji ve Malzeme Mühendisliği
Tez Yöneticisi: Assoc. Prof. Dr. Simge Çınar Aygün
Ortak Tez Yöneticisi: Prof. Dr. Bora Maviş

Eylül 2022, 130 sayfa

Artan enerji talebi, yüksek hacimsel enerji yoğunluğuna sahip batarya sistemlerini gerektirmektedir, bu nedenle mevcut hedeflerden biri, birim hacim başına yüklenebilecek aktif malzeme miktarını maksimize etmektir. Bu durum doğrudan partiküllerin dağıtıklık durumu ile ilgilidir ve yüksek hacimsel enerji yoğunluğunu elde etmek için dağılıbilir partiküller gereklidir. Aktif malzemelerin elektriksel iletkenliğini arttırmak için kullanılan karbon kaplama, partiküllerin aglomerasyonunda önemli rol oynamaktadır. Bu nedenle bu tezde, tekil elektroaktif malzemelerin dağıtılabirliğini koruyacak şekilde uygun bir karbon kaplama prosedürünün geliştirilmesi amaçlanmıştır. Burada, yeni bir yaklaşım olarak, tam karbon kaplamalı, dağılıbilir parçacıkları sentezlemek için koloidal ilkelerin kullanımı ve ardından piroliz işlemi gerçekleştirilmiştir.

Model sistem olarak LiFePO_4 (LFP) elektroaktif malzemesi seçilmiştir. İlk olarak, polyol yöntemi ile tekil olarak dağıtık LFP parçacıkları üretilmiştir. Yalın LFP parçacıkları üzerindeki zeta potansiyel analizlerinden sonra, CTAB (setiltrimetilamonyum bromür) yüzey aktif madde olarak seçilmiş ve bir karbon kaynağı olarak kullanılmıştır. CTAB'in LFP'ye kritik oranı zeta potansiyelinin işaretinin değiştiği ve stabilize olduğu nokta ile belirlenmiştir ve iki aşamalı bir

piroliz prosedürü tasarlanmıştır. Bu proseste üretilen optimum karbon kaplı tekil parçacıklar ve yalın LFP numuneleri dağıtılabirlik, doldurma yoğunluğu, ve elektrokimyasal performans açıdan karşılaştırıldı. Yalın LFP ($1.11 \text{ g}\cdot\text{cm}^{-3}$) ve karbon kaplı LFP parçacıklarının ($1.16 \text{ g}\cdot\text{cm}^{-3}$) doldurma yoğunluğu oldukça benzer elde edilmiştir. Sonuçlar, burada kullanılan zeta potansiyeli analizine dayalı yaklaşımın uygulanabilirliğini doldurma yoğunluğunda ve dağıtılabirlikte herhangi bir kayıp olmaksızın homojen karbon kaplama üretimi ile göstermektedir.

Anahtar Kelimeler: Karbon Kaplama, Koloidal Stabilizasyon, Dağıtık Elektroaktif Malzeme Sentezi, Lityum Demir Fosfat, Setiltrimetilamonyum Bromür

To my family...

ACKNOWLEDGMENTS

I sincerely thank my advisor, Dr. Simgе Çınar Aygün for her patience, guidance, and support throughout my research. Also, the comments she gave me a new perspective on life. Collaborating with such a woman standing on her feet motivated and inspired me during my graduate education.

I am heartily grateful to Dr. Bora Maviş for his patience, guidance, encouragement, and for getting me excited about research. He always inspires me in science and life, also broadens my vision. It is a pleasure and honor to collaborate with him. Brainstorming is so fun with him. Thanks to him for all his contributions and comments not only in my research but also in my self-improvement.

I would like to thank my thesis committee: Prof. Dr. Kadri Aydınol, Assoc. Prof. Dr. Emre Büküşođlu, Assist. Prof. Dr. Irmak Sargın and Prof. Dr. Ziya Esen for their insightful and supportive comments, as well as positive attitudes. I would also like to thank Prof. Dr. Mehmet Kadri Aydınol and Prof. Dr. Caner Durucan for providing their lab facilities.

Thanks to Bayram Yıldız for his guidance, support in my research and for being such a good teammate.

Thanks to my other valuable lab mates Elif Coşkun, Mert Ulusel, Orçun Dinçer, Emre Altın, Ekin Kurşun, Duygu İnce, Burak Cengiz, Dođu Şeyda, Doruk Siyanüç, İbrahim Egemen Küçük and Mert Oral because they make the lab a more enjoyable place to work.

Special thanks to my other valuable supporters in my thesis; Süha Tirkeş, Mustafa Utku Yıldırım, Muhammed Mustafa Balcılar and Loay Akmal Madbouly.

Lastly, my dear parents and beloved brothers, I am grateful to have you, thanks for your endless support.

TABLE OF CONTENTS

ABSTRACT.....	v
ÖZ	vii
ACKNOWLEDGMENTS	x
TABLE OF CONTENTS.....	xi
LIST OF TABLES	xiii
LIST OF FIGURES	xiv
LIST OF ABBREVIATIONS.....	xviii
CHAPTERS	
1 INTRODUCTION	1
2 LITERATURE REVIEW	3
2.1 Lithium-ion Based Electrochemical Battery Systems	3
2.2 Carbon Coating of Electroactive Materials.....	5
2.2.1 Advantages of Carbon Coating	5
2.2.2 Carbon Coating Methods and Optimizations	11
2.2.3 Pyrolysis in Carbon Coating	21
2.3 Volumetric Energy Density of a Battery System and Properties of Carbon Coated Electroactive Materials	32
2.4 Colloidal Principles.....	37
2.4.1 Colloidal Stabilizations	37
2.4.2 Surfactants	39

2.4.3	Interparticle Interaction Control with Surfactants and Colloidal Stabilization in an Aqueous Medium	43
2.4.4	Zeta Potential	45
3	MATERIALS AND METHODS	47
3.1	Materials	49
3.2	LFP Particle Synthesis.....	49
3.3	Coating of LFP Particles with CTAB.....	50
3.3.1	Preparation of Dilute Suspensions of LFP and CTAB	50
3.3.2	Preparation of Concentrated Suspensions of LFP and CTAB	51
3.4	Preparation of CTAB-Coated LFP Powders	51
3.5	Pyrolysis of the LFP Particles with/without CTAB Coating.....	51
3.6	Characterizations	52
3.7	Electrode Preparation and Electrochemical Tests	55
3.8	Thesis Objectives.....	47
4	RESULTS & DISCUSSION	57
4.1	Properties of As-synthesized LFP particles.....	57
4.2	Investigation of the Interactions with CTAB and LFP.....	59
4.3	Pyrolysis of the CTAB-Coated LFP Particles	70
5	CONCLUSIONS AND FURTHER RECOMMENDATIONS.....	97
	REFERENCES	101
	APPENDIX	
A.	Suspension Properties of the Dilute (0.01 wt. % LFP) and Concentrated (0.1 wt. % LFP) LFP-CTAB Systems	127

LIST OF TABLES

TABLES

Table 2.1 Examples of Some Common Surfactants	41
Table 4.1 Mean tap density values of as-synthesized LFP, carbon coated LFP samples; LFP _B /C -600 and LFP _E /C -600	96

LIST OF FIGURES

FIGURES

Figure 2.1. Li-ion based electrochemical battery systems:	3
Figure 2.2. Electron transfer pathways when there is a) complete coating b) partial coating ^[38]	5
Figure 2.3. Schematic representation of effect of carbon layer thickness on ionic and electronic conductivity of an electroactive material (LiMePO ₄ ; Me= Mn, Ni, Fe) ^[42]	6
Figure 2.4. Surface degradation of an electroactive material with the (a) absence and (b) existence of carbon layer ^[5]	8
Figure 2.5. Dispersed particles (I) agglomerated (II) and aggregated (III) particles. In the agglomeration process (A), the initially dispersed particles interact with each other in a reversible way by weak forces, whereas they are held tightly together by strong forces, in an irreversible way, upon aggregation (B) ^[60]	10
Figure 2.6. <i>in-situ</i> carbon-coated LFP particles with different morphologies using various carbon sources of glucose (G), carboxy methyl cellulose (CMC), ascorbic acid (AA) and polyacrylic acid (PAA) ^[70]	12
Figure 2.7. Effect of <i>in-situ</i> carbon coating of LFP on the dispersion quality: with the changing amount of sucrose ^[73]	13
Figure 2.8. <i>in-situ</i> carbon coating of LFP with similar type of carbon sources glucose (C-LFP-G), fructose (C-LFP-F), sucrose (C-LFP-S) ^[74]	14
Figure 2.9. <i>in-situ</i> carbon coating of different electroactive materials with two different precipitation order (a and b), SEM images of the Fe (c), Mn (d) and Ni (e) containing particles resulting in different CTAB adsorption and carbonization degree (f) ^[42]	16
Figure 2.10. Carbon distribution on different electroactive materials ^[42]	17

Figure 2.11. TEM and HRTEM nano-graphs of <i>ex-situ</i> carbon-coated LFP particles with varied amount of sucrose; (a) and (b) using 18 wt.% sucrose ^[84] , (c) and (d) using 9 wt.% sucrose ^[85]	18
Figure 2.12. SEM images of <i>ex-situ</i> carbon-coated LFP particles with various amounts of sucrose a) 0.1 M b) 0.5 M and c) 1 M sucrose, and corresponding d) initial charge and discharge curves at 0.1 C rate of powders ^[86]	19
Figure 2.13. TEM and HRTEM images of the <i>ex-situ</i> carbon-coated (a), (b) nanorod shaped ^[87] and (c), (d) nanosphere shaped ^[88] LFP particles using dopamine, respectively	20
Figure 2.14. Carbon Structure of a) Amorphous and b) Graphitic Carbon ^[99]	22
Figure 2.15. Electrical conductivity of carbon-coated Li ₄ Ti ₅ O ₁₂ prepared under different temperatures a) and corresponding TEM nanographs of carbon coated Li ₄ Ti ₅ O ₁₂ under b) 650, c) 800, and d) 900 °C temperatures ^[100]	23
Figure 2.16. HRTEM images of carbon-coated LFP after pyrolysis performed at (a)700 and (b)750 °C and Electrochemical profiles at C/12, of the coated and uncoated LFP samples at pyrolyzed at 700 °C for 6 hours ^[102]	25
Figure 2.17. TEM images of a) bare LFP particles, and carbon coated LFP particles using b) asphalt, c) glucose carbon sources ^[127]	29
Figure 2.18. Commercial LFP powders supplied from the same company, showing different flowability; the former was suspended in the aqueous slurry (a) and the latter was gelled (b) ^[135]	31
Figure 2.19. Particle size distribution effect on tap density with (a) higher packing in the presence of smaller particles that fills the spaces between particles and (b) less packing in the absence of small particles ^[141]	34
Figure 2.20. Tap density of carbon coated particles in the forms of a) aggregated, b) carbon bridges between particles and c) dispersible/individual (blue colored forms and black colored thin forms represent electroactive material and carbon layer, respectively)	35
Figure 2.21. Colloidal stabilization methods: a) Electrostatic b) Steric and	37
Figure 2.22. a) Full and b) Partial graphene wrapping of LFP particle ^[155]	39

Figure 2.23. Structure of a surfactant monomer (unimer).....	40
Figure 2.24. Structural forms of surfactant a) molecule and b) micelle in a polar solvent.....	42
Figure 2.25. Assembly of CTAB onto citrate capped gold nanoparticles ^[175]	44
Figure 2.26. Schematic illustration of Zeta Potential ^[184]	46
Figure 3.1. The gradual heating procedure used in the pyrolysis experiments	52
Figure 4.1. Characterization of the as-synthesized LFP particles: a) XRD pattern, b) Sedimentation test within 6 hours and zeta potential measurements, c) and d) SEM micrographs	58
Figure 4.2. a) Zeta potential of LFP particles as a function of CTAB concentration and corresponding conductivities for dilute (0.01 wt. %) suspensions. The regions where the behavior change occurred was denoted as [1], [2] and [3],	60
Figure 4.3. Particle size distribution of 1 mM CTAB in water, LFP (0.01 wt.%) in water, and particles suspended in the turbid part of the [LFP (0.01 wt. %) + CTAB (1 mM)] suspension after a day of sedimentation in water	64
Figure 4.4. Schematics of the corresponding zeta potential stages denoted by [1] monolayer, [2] bilayer, [3] bilayer + excess free CTAB	65
Figure 4.5. Concentrated system a) Zeta Potential and Conductivity change at different CTAB concentrations b) Sedimentation test of corresponding suspension	67
Figure 4.6. Particle size distribution of CTAB (10 mM), LFP particles (at 0.1 wt. %) and LFP (0.1 wt. %) + CTAB (10 mM) suspension in DIW, taken from the turbid part of the suspension after a day of sedimentation in water	68
Figure 4.7. ATR - FTIR spectra of the samples: EG, CTAB, LFP,	70
Figure 4.8. TGA of CTAB with 2 °C/min and 10 °C/min	71
Figure 4.9. TGA of LFP, LFP _B and LFP _E samples with 2 °C/min	72
Figure 4.10. TGA of LFP, LFP _B and LFP _E samples with 10 °C/min	74
Figure 4.11. XRD patterns of samples, pyrolyzed at a) 500 °C, b) 600 °C, and c) 700 °C, indexed by LiFePO ₄ , JCPDS Card No: 83-2092, asterisk states the secondary phase of lithium phosphate (*: Li ₃ PO ₄).....	76

Figure 4.12. SEM micrographs of the samples at different CTAB concentration and temperature	78
Figure 4.13. Sedimentation photos of the corresponding SEM micrographs	79
Figure 4.14. Galvanostatic charge/discharge profiles of the as-synthesized LFP and samples of 500°C and 600°C heat treatment samples	80
Figure 4.15. a) Electrochemical Impedance Spectroscopy of the as-synthesized LFP and samples of 500 °C and 600 °C heat treatment samples.....	82
Figure 4.16. The charge/discharge voltage curves of a) LFP, and samples treated at 500 °C; b) LFP-HT-500, d) LFP _B /C-500, f) LFP _E /C-500 and 600 °C; c) LFP-HT-600, e) LFP _B /C-600, g) LFP _E /C-600.....	85
Figure 4.17. HRTEM images of the samples after 600°C heat treatment a) LFP-HT-600 b) LFP _B /C-600 c) LFP _E /C-600 d), e) and f) are corresponding high magnification images, respectively.....	86
Figure 4.18. The ATR-FTIR spectra of the samples before heat treatment, LFP, and after 600°C heat treatment; LFP-HT-600 LFP _B /C-600 and LFP _E /C-600	88
Figure 4.19. XPS spectra of the samples LFP and after 600°C heat treatment; LFP-HT-600 LFP _B /C-600 and LFP _E /C-600.....	90
Figure 4.20. XPS spectra and deconvoluted peaks of the samples; a) LFP, b) LFP-HT, c) LFP _B /C-600 and d) LFP _E /C-600.....	92
Figure 4.21. Raman analyses of the samples: LFP, LFP-HT-600, LFP _B /C -600, LFP _E /C -600.....	93
Figure 4.22. Deconvolution of Raman spectra in the wavenumber range of 900-2000 cm ⁻¹ for a) LFP-HT-600, b) LFP _B /C-600 and c) LFP _E /C-600.....	95
Figure A.1. Changes in a) Zeta Potential and b) Conductivity of the Dilute (0.01 wt.% LFP) and Concentrated (0.1 wt. % LFP) LFP-CTAB Suspension System .	127
Figure A.2. a) Measurement of Sedimentation Length using ImageJ Software, b) Sedimentation Rate of the Dilute (0.01 wt.% LFP) and Concentrated (0.1 wt. % LFP) LFP-CTAB Suspension System.....	129
Figure A.3. pH changes in the Dilute (0.01 wt.% LFP) and Concentrated (0.1 wt. % LFP) LFP-CTAB Suspension System	130

LIST OF ABBREVIATIONS

ABBREVIATIONS

LIBs: Lithium-ion Batteries

Li-ion, Li⁺: Lithium-ion

SFB: Suspension Flow Battery, Semi-solid/ Slurry Flow Battery

LFP: Lithium Iron Phosphate. LiFePO₄

LFP/C: Carbon coated LFP

CTAB: Cetyltrimethylammonium Bromide

CMC: Critical Micelle Concentration

EG: Ethylene Glycol

XRD: X-Ray Diffraction

DLS: Dynamic Light Scattering

TGA: Thermogravimetric Analysis

SEM: Scanning Electron Microscopy

XPS: X-Ray Photoelectron Spectroscopy

EIS: Electrochemical Impedance Spectroscopy

HRTEM: High Resolution Transmission Electron Microscopy

ATR- FTIR: Attenuated Total Reflectance - Fourier Transmission Infrared Spectroscopy

CHAPTER 1

INTRODUCTION

Energy storage materials and systems are being more critical than ever due to the increase in energy demand and depletion in fuel-based resources. Lithium-ion (Li-ion) based electrochemical energy storage systems, suspension flow and conventional lithium-ion batteries, are promising candidates due to their safety^[1], high energy density^[2] and environmental friendliness^[3]. Nonetheless, electronic and ionic conductivities of the cathode electroactive materials are intrinsically low^[4]. The most prevalent and proven method to improve these inherently low conductivities of the electroactive materials is carbon coating. Carbon coating further provides: (i) protective layer between the electroactive material and external environment (electrolyte or air)^[5] (ii) mechanical integrity (structural stability) during charging/discharging^[5]. As a result, most, if not all, of the commercially available Li-ion based electroactive materials are currently carbon coated.

Carbon coating process is based on mixing the electroactive material and the carbon source either via *ex-situ* (after particle synthesis)^{[4],[6]} or *in-situ* (during particles synthesis)^{[4],[6]} methods and followed by pyrolysis process. In studies reported in the literature, the synthesis of carbon coated electroactive materials were mainly based on crude parameter optimization (carbon source type, amount, temperature *etc.*) with the main aim of achieving high gravimetric energy density ($\text{Wh}\cdot\text{kg}^{-1}$). With perfectly designed particles, examples of which are few, the high theoretical capacity is accessible with the added advantage of carbon coating putting less emphasis on particle design. Yet, with the recent developments in stationary (grid) energy storage^{[7],[8]}, the electrical vehicles and portable electronics^{[9],[10]}, ultimate goal has become to squeeze in higher amounts of electroactive materials in smaller volumes,

i.e., increasing the volumetric energy density ($\text{Wh}\cdot\text{l}^{-1}$) besides gravimetric energy density. Therefore, the compactness (packing density or tap density)^{[11],[12]} of the system becomes a critical design parameter. In order to improve the volumetric energy density, the effects of particle design parameters such as size^{[13],[14]} and morphology^{[15],[16]} on the tap density of electroactive materials have been investigated. Even though, the highest tap densities were achieved when individual particles were used^{[17],[18]}, the effect of agglomeration state of electroactive particles has not been explicitly studied. Moreover, the influence of carbon coating process parameters on the agglomeration state of particles is lacking.

In this study, it is hypothesized that the carbon coating of electroactive materials can be engineered by promoting colloidal interactions between individual particles and carbon source, and by thorough optimization of the pyrolysis conditions. When the critical parameters were determined, such a carbon coating process will then, have a potential to be adopted for other particle systems. In the subsequent sections, firstly fundamental concepts of carbon coating, tap density and colloidal stabilization regarding with Li-ion batteries are reviewed (Chapter 2). Experimental details to achieve objectives of the thesis are presented in Chapter 3 and results of the study were reported and discussed in Chapter 4. The conclusions and the potential future directions of this thesis work were summarized in Chapter 5.

CHAPTER 2

LITERATURE REVIEW

2.1 Lithium-ion Based Electrochemical Battery Systems

With the depletion of fossil fuels and their detrimental effects on the environment, the need for alternative energy storage and conversion systems is growing rapidly. Among various options, Li-ion based batteries offer high capacity, safety, lower cost, cycling performance etc. advantages^[4]. Therefore, rechargeable Li-ion batteries (LIBs) are being extensively investigated and integrated to various aspects of everyday life. Depending on the application/utilization area, required LIB types vary. While conventional LIBs (Figure 2.1-a) are desired in portable devices and transportation (electrical vehicles, hybrid electric vehicles), flow assisted LIBs (suspension flow battery or semi solid LIBs)^[19] (Figure 2.1-b), which are yet to be commercialized, would be preferred in large scale energy storage systems due to their potential flexibility in design and competency in scaling cost.

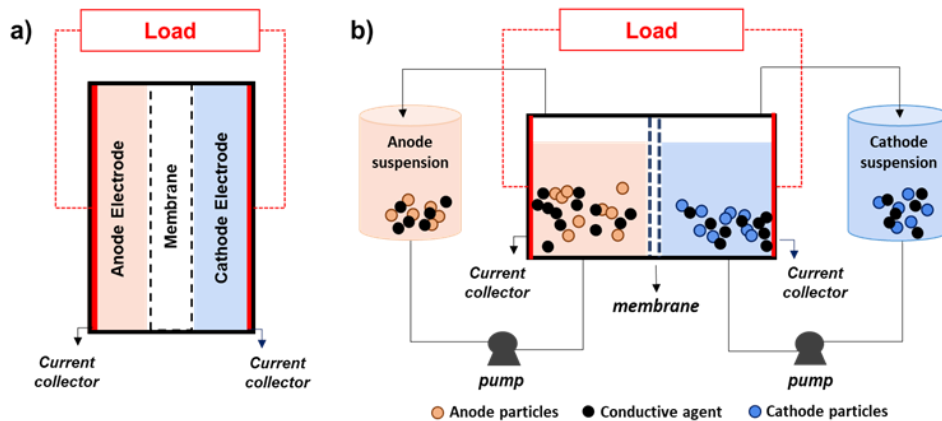


Figure 2.1. Li-ion based electrochemical battery systems:
a) Conventional Li-ion Battery, b) Suspension Flow Battery

Commonly, battery systems consist of cathode and anode electrodes in an electrolyte, a membrane in between, and current collectors connected to an external circuit (Figure 2.1-a and b). The working principle is based on the oxidation and reduction (redox) reactions between anode and cathode sides^[20]. Transfer of lithium ions and electrons takes place during charging and discharging between anode and cathode sides, also, since these reactions are reversible these battery systems are rechargeable. The following electrochemical reactions can be used to describe the charge and discharge mechanism of a lithium-ion battery. Here, as an example LFP and graphite are the cathode and anode, respectively^[21, 22]:



The electrochemical reaction in LIBs involves the migration of Li^+ into (insertion/intercalation) and out of (extraction/deintercalation) cathode and anode materials. During discharging, Li^+ travels from anode, then through the electrolyte, to cathode meanwhile electron is released for every Li^+ involved in the reaction to an external circuit where it can power a device and vice versa happens during charging. Regarding these reactions, the efficiency of electrochemical energy storage and conversion during charging/discharging is strongly dependent on the ionic and electronic conductivity of the electroactive materials^[23]. In other words, both ionic and electronic conductivities of the electroactive materials directly determine electrochemical performance and rate capability (*i.e.*, how quickly battery charge and discharge) of the batteries. Additionally, depending on the electroactive materials used in both anode and cathode sides, volumetric and specific energy density of the systems changes. Lithium ion has the lowest reduction potential, compared to other elements and it is one of the lightest elements, having small ionic radius. Due to these advantages, using Li-ion based cathode materials in these systems, allows having theoretically higher gravimetric and volumetric capacity, as well as high power density compared to other chemistries^[24]. However, Li-ion based

cathode materials have low electronic and ionic conductivities and have limitations in achieving theoretical electrochemical performance^[23, 25, 26]. To overcome these drawbacks, doping^[27-29], size reduction^[30, 31], morphology control^[6, 32, 33], metal oxide coating^[34, 35] approaches have been studied. Among these, the most common method has been carbon coating of electroactive materials^[36, 37].

2.2 Carbon Coating of Electroactive Materials

2.2.1 Advantages of Carbon Coating

The main purpose of the carbon coating is to accelerate electron transfer by creating new conductive paths on the surface of the particles^[38]. If the electroactive materials are fully covered with carbon as schematized in Figure 2.2-a, the electrons are carried over the conductive layer on the surface of the particles instead of passing through the electroactive material with the low electrical conductivity. Hence, the electron transfer is facilitated. Otherwise, when the particles are uncoated (bare) or partially coated, electron transport would be limited as it occurs through the particles and over the partially existing carbon layer (Figure 2.2-b). For this reason, fast electron transfer requires not only the presence of carbon, but also complete carbon coverage around particle.

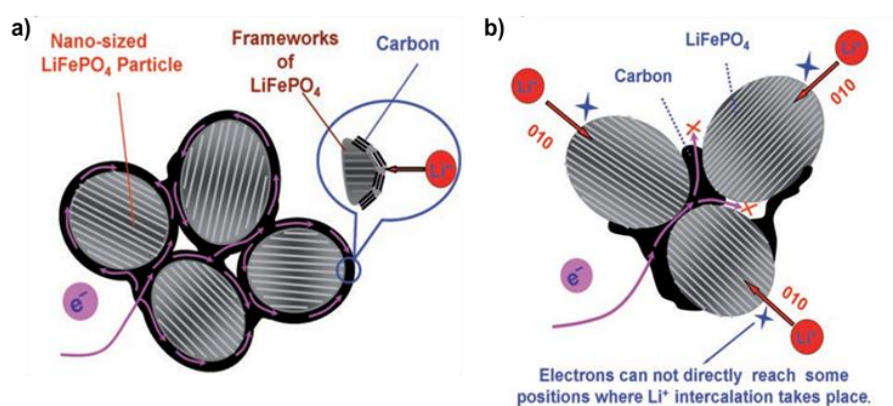


Figure 2.2. Electron transfer pathways when there is a) complete coating b) partial coating^[38]

Besides enhanced electrical conductivity, ionic conductivity of the particles is increased concomitantly as a result of the carbon coating. When the full coverage of carbon coating is achieved, electrons move homogeneously around the particle and leads to attraction of positively charged lithium ions from the electrolyte. Hence, it allows the particles to access lithium ions from all directions and ionic conductivity of the particles are improved^[5]. In addition to the overall surface coverage of carbon layer, its thickness has a remarkable effect on both ionic and electrical conductivities. Electrical conductivity is improved with more amount of carbon (a thick carbon layer), whereas lithium-ion diffusivity into/out of an electroactive material would be poorer since thick layer acts as a physical barrier (Figure 2.3). Thus, the thickness of the carbon coating should be adjusted in such a way that it does not prevent ionic diffusion while increasing electronic conductivity^[39]. In addition, too thick of a carbon coating layer decreases the volumetric energy density of battery system due to inactive material loading^[40]. Consequently, full carbon coverage with optimal thickness is required for faster electronic and ionic transport as well as high volumetric energy density^[25, 41, 42].

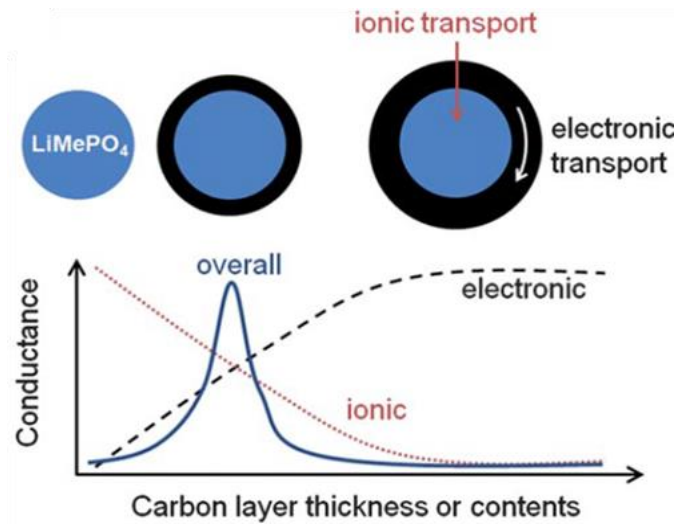


Figure 2.3. Schematic representation of effect of carbon layer thickness on ionic and electronic conductivity of an electroactive material (LiMePO₄; Me= Mn, Ni, Fe)^[42]

Furthermore, electrochemical polarization, linked to internal resistance of a battery during charging/ discharging, decreases the power density and lengthens charging

times^[43, 44]. The continuous and uniform carbon coating allows the particles to undergo electrochemical reaction homogeneously across the surface and leads to the uniform transport of both ions and electrons. Hence, the homogeneous carbon coating aids in minimizing the polarization phenomenon^[45, 46].

Under the conditions batteries are generally exposed to, secondary reactions between the surface of the electroactive material and electrolyte (aqueous or organic) or air can be expected and detrimental to performance^[5, 47, 48]. Another advantage of the carbon coating is creating a protective layer on the surface of the particles against these reactions^[5, 47, 48]. Because carbon has a chemically stable structure, a complete carbon coverage forms a physical barrier on the electroactive material surface and avoids direct contact of the particles with the electrolyte and surface oxidation.

One of the most common salt electrolytes used in batteries is LiPF_6 . When it decomposes HF (Hydrofluoric Acid) is formed and hydrolysis of HF give rise to dissolution of transition metals and corrosion of the surface of the electroactive material (Figure 2.4-a). As a result, the cathode structure is destroyed and the capacity of the battery declines. The shielding carbon layer that surrounds the particles inhibits the dissolution of the metal ions^[5, 47] and it provides an improvement in the specific capacity and cycle performance of the particles as well as maintaining the energy density of the battery system. The carbon layer also keeps oxygen and moisture in the air away from the active cathode material (Figure 2.4-b) and structural stability of the electroactive material is sustained^[5, 47]. Thus, side reactions are minimized, surface degradation is suppressed, the electrochemical performance is improved, and also capacity fading is reduced through the complete carbon coverage of the particle^[47, 49]. From another point of view, organic electrolytes, which are flammable and toxic, are attempted to be replaced by aqueous electrolytes in order to enhance the safety of next generation energy storage systems^[50-52]. Although using aqueous electrolyte results in poor cycle life and low energy density, it is still under investigation for the mentioned safety concern. For this reason, both anode and cathode materials are carbon coated and a protective

layer is formed against water, minimizing the degradation of electrochemical performance in aqueous LIBs^[53, 54].

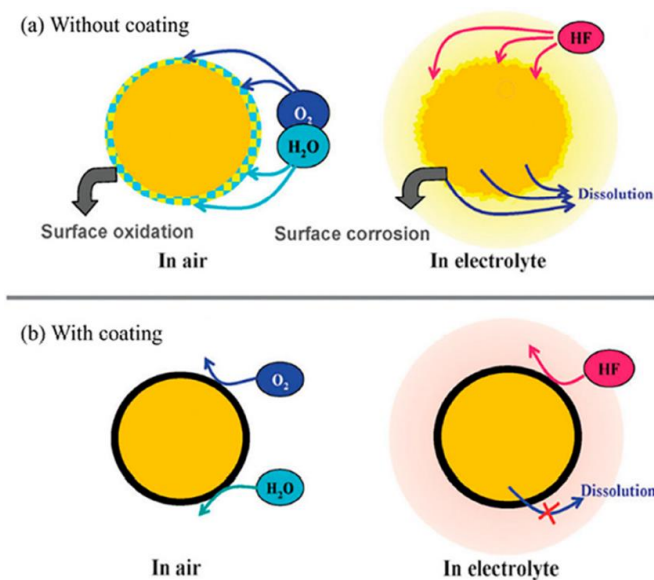


Figure 2.4. Surface degradation of an electroactive material with the (a) absence and (b) existence of carbon layer^[5]

One further advantage of the carbon coating is that it helps the particle maintain its structural integrity^[55, 56]. Phase transitions and repetitive lithiation and de-lithiation that occur during charge/discharge cycles, lead to repeated expansion and contraction in an electroactive material. Accordingly, structural, and volumetric changes occur in the material during cycling. As a result, the electroactive material may break down and lose its integrity. The carbon sheath allows the electroactive material to preserve its structure for a longer time and prolongs its service life^[57].

All in all, the carbon coating of electroactive materials is advantageous in three major mechanisms: enhancing conductivity (electronic and ionic), chemical stability, and structural stability. As these three advantages of carbon coating will affect and support each other during battery operation, carbon coating is critical in obtaining a structurally stable electroactive material and high electrochemical performance.

To fully benefit from the merits of the carbon coating, the previously discussed characteristic of the particles (*i.e.*, dispersibility) and coating (*i.e.*, optimum thickness with full coverage) must be considered in designing the carbon coating method.

2.2.1.1 Agglomeration State of the Particles

The physical properties of the electroactive materials (*i.e.*, agglomeration state of the particles) determine how they influence the properties of materials dispersions and, in turn, the electrochemical performance of a battery system. Accordingly, before addressing the physical properties of the carbon coated particles, it should be understood the meaning of dispersed, agglomerated, and aggregated particle systems^[58, 59].

A well-dispersed system consists of individually separated particles and is stable in the liquid phase due to interparticle repulsive forces (Figure 2.5 - I). The formation of agglomerates (Figure 2.5- II) is due to attractive or weakly repulsive interactions between particles in the liquid, whereas the formation of aggregates (hard agglomerates, fused, unbreakable particles) (Figure 2.5- III) is usually chemical and often occurs during the synthesis and/or preparation of particles. Thus, agglomerates are reversible (Fig. 2.5-A) and can be redistributed within the system, while aggregated particles create an irreversible system and cannot be initially separated into dispersed particles (Fig. 2.5-B).

The irregular cluster of particles forms in both agglomerated and aggregated system. In agglomerated system, external surface area tends to approach the sum of the surface areas of the individual components, whereas in aggregated system external surface area is significantly smaller than the sum of calculated surface areas of the individual components. Thus, aggregated system, particularly, cause underutilization of the particles due to reduced available surface area and leads to losses in capacity and rate capability.

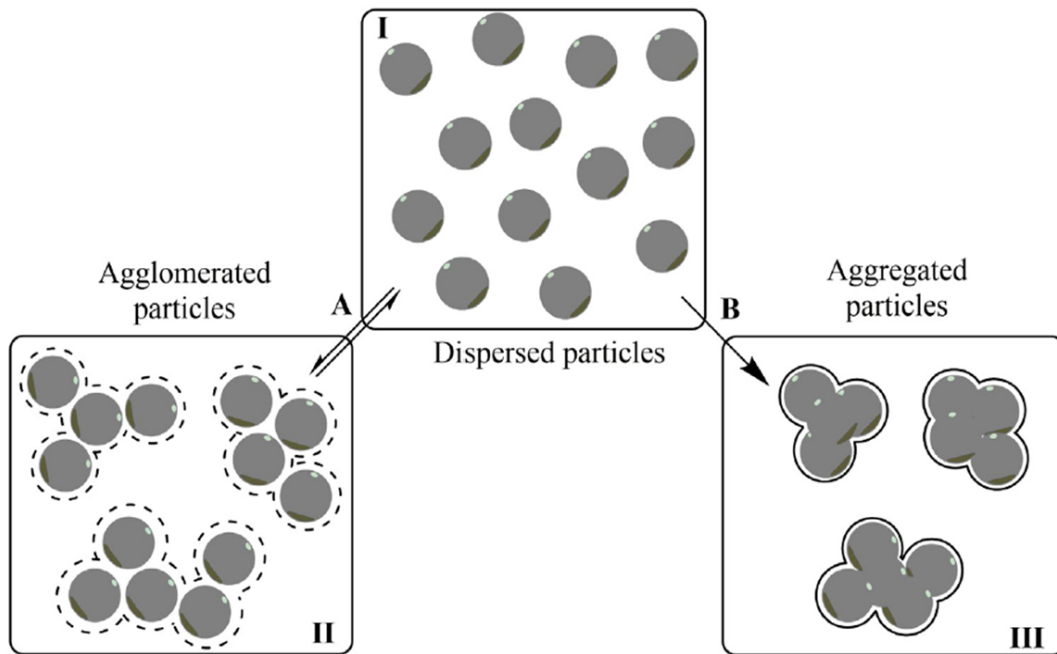


Figure 2.5. Dispersed particles (I) agglomerated (II) and aggregated (III) particles. In the agglomeration process (A), the initially dispersed particles interact with each other in a reversible way by weak forces, whereas they are held tightly together by strong forces, in an irreversible way, upon aggregation (B)^[60]

Furthermore, aggregated carbon coated particles decrease the tap density, which, in turn, causes reduced energy density in the full battery cells^[40]. Besides, severe aggregation creates detrimental problems in the processability of electrodes in conventional LIBs^[61, 62], while it requires high pump energy in SFBs, leading to lower efficiency in both types of LIBs^[63]. Since SFBs are flow-assisted systems, the effect of aggregation will be much more pronounced in SFBs than in the case of conventional LIBs^[64]. As a result, the physical properties of the carbon coated particles are critical in achieving high energy density battery systems.

2.2.2 Carbon Coating Methods and Optimizations

The carbon coating process responsible for the particle agglomeration state directly and affects the processability of an electrode and, in turn, the electrochemical performance of a battery system. Thus, in this section, each carbon coating procedure was addressed in terms of particles' physical properties.

Carbon coating process can be employed in two ways: *in-situ* and *ex-situ* carbon coating.

In the *in-situ* carbon coating, all the precursors of an electroactive material are mixed with a carbon source, which is generally an organic molecule, and treated under the reaction conditions. Then, heat treatment is applied for crystallization of the active material and carbonization of the carbon source^[4, 47]. During heat treatment, pyrolysis takes place in which organic compounds decompose and amorphous carbon transforms into graphitic carbon. Presence of an organic molecule that has inherent functional groups or a potential of hydrogen bonding with crystal surfaces can intermingle with both the nucleation and growth of the crystallites and secondary particles. In some cases, this may even lead to nanosized particles^[47, 65]. Small particles commonly exhibit better electrochemical performance than the larger ones due to their higher ionic conductivity and narrowed the diffusion path of Li⁺ ^[65]. Recent studies have shown that special morphological and surface design of the active materials is advantageous in terms of Li-ion diffusion, structural stability, and electrochemical performance during battery cycling^[66-69]. In line with this, *in-situ* carbon coating method is useful in synthesis of carbon coated electroactive materials, having a wide range of morphologies. Despite these advantages, *in-situ* carbon coating requires fine tuning of the reaction parameters such as precursor type and ratio, feeding sequence of the precursor, carbon source type and amount, temperature, pressure in some synthesis conditions, stirring the reaction medium, pH, time, reaction kinetics and so on.

In the study of Bhuvaneshwari and Kalaiselvi, for example, it was shown that by setting the reaction pH and reagent to carbon source ratio, *in-situ* carbon coating of LFP electroactive material and various particle morphologies could be achieved with different carbon sources^[70]. While using glucose as a carbon source led to irregularly shaped LFP particles, using carboxy methyl cellulose, ascorbic acid and polyacrylic acid resulted in microrods, flakes and platelet morphologies, respectively (Figure 2.6). In connection with the carbon sources, the carbon layer of the samples displayed different uniformity and graphitization degree. Thus, different morphology and carbon layer features of the particles resulted in different electrochemical performance and tap density. Also, it was stated that the carbon coated electroactive materials were synthesized hydrothermally in an autoclave. It is well known that in a sealed reaction system, pressure is a significant parameter and addition of carbonaceous material into the system helps reducing the atmospheric gas pressure and thus maintaining the concentration of the reagents^[71]. For this reason, the combination of the reagents as well as the reaction conditions direct and control the properties of the resulting powders.

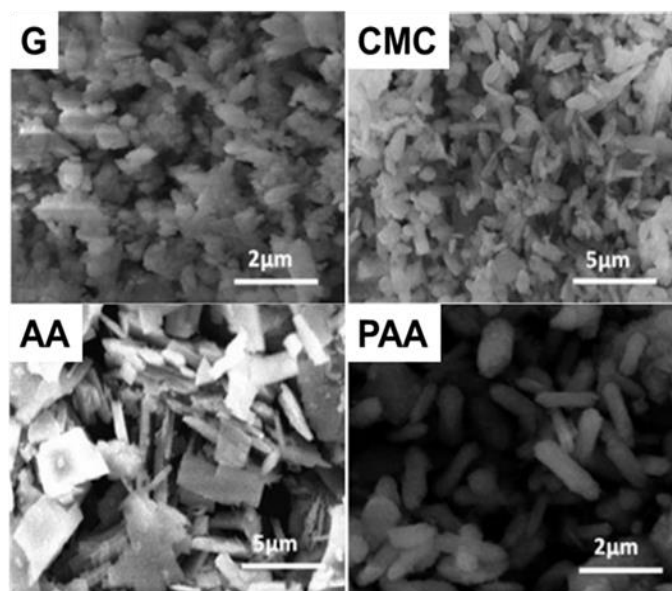


Figure 2.6. *in-situ* carbon-coated LFP particles with different morphologies using various carbon sources of glucose (G), carboxy methyl cellulose (CMC), ascorbic acid (AA) and polyacrylic acid (PAA)^[70]

Because there are multiple parameters to manage in the *in-situ* method controlling the size, shape, and coating layer at the same time becomes relatively complicated with this method^[70], and thus, tuning the electroactive particle characteristics is not a straightforward process^{[38],[72]}.

The study of Qi's *et. al.* compared pristine LFP, and *in-situ* carbon coated LFP particles, synthesized in an autoclave^[73]. The pristine particles were synthesized in microsphere morphology with the aim of close packing. *In-situ* carbon coated particles were synthesized with different amounts of sucrose (with the 10 and 15 wt. % of LFP) (Figure 2.7). The resulting particles were sphere-like but agglomerated. As a result, *in-situ* carbon coated particles showed poor dispersion quality compared to the pristine one, but carbon coated particles exhibited higher initial discharge capacity ($\sim 80, 118, 130 \text{ mAh}\cdot\text{g}^{-1}$ at 0.1 C with increasing sucrose amount of 0, 10 and 15 wt. % sucrose, respectively). In other words, optimization of the coating with the amount of sucrose led to the highest specific capacity, but at the cost of aggregation of the particles and irregular distribution of carbon between the particles.

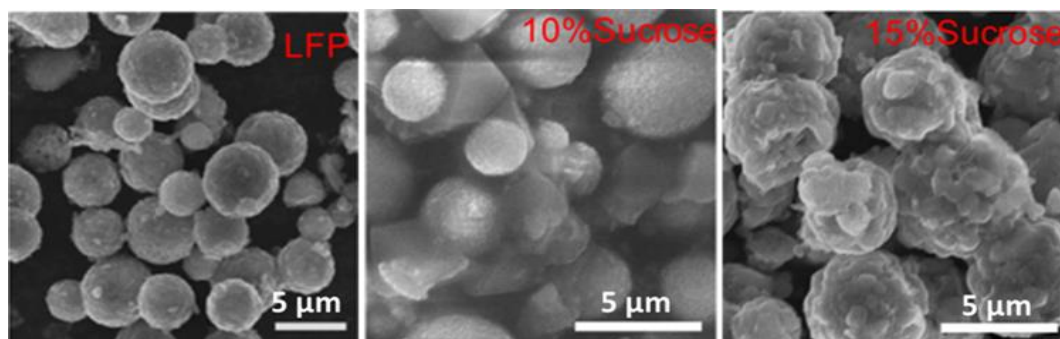


Figure 2.7. Effect of *in-situ* carbon coating of LFP on the dispersion quality: with the changing amount of sucrose^[73]

Obviously, the increasing amount of carbon affected the dispersion of the particles even though it enhanced the battery performance. Control on spherical morphology was possible during bare electroactive material synthesis, however dispersibility of the particles was affected in samples with *in-situ* carbon coating. This is an indication

that introducing the carbonaceous material into the reaction medium requires a meticulous design of the reaction parameters to preserve dispersibility of particles.

Apart from the amount of the carbon, type of the carbon source remarkably changes the physical and chemical properties of the electroactive materials. In the study of Pratheesksha *et. al.*, LFP particles were *in-situ* carbon coated with similar type of carbons; glucose, fructose, and sucrose under same synthesis and pyrolysis conditions^[74]. Glucose and fructose are both monosaccharides having equivalent formula but distinct isomeric forms. They can also act as reducing agents. Sucrose on the other hand, is a disaccharide. It has more carbon and does not have a reduction power. Even when similar types of carbon sources (glucose and fructose) were used in the synthesis, the particles showed huge differences in morphology, size, and dispersion characteristics (Figure 2.8).

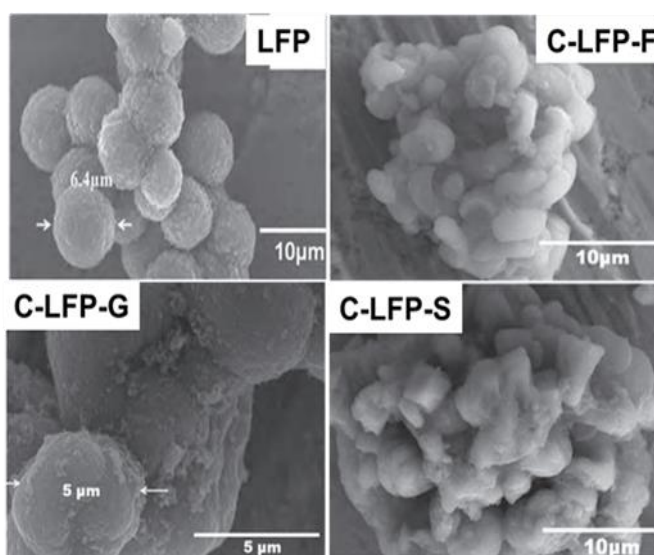


Figure 2.8. *in-situ* carbon coating of LFP with similar type of carbon sources glucose (C-LFP-G), fructose (C-LFP-F), sucrose (C-LFP-S)^[74]

Although the carbon-coated particles with sucrose exhibited the highest initial discharge capacity ($116 \text{ mAh}\cdot\text{g}^{-1}$) than those coated using fructose ($98 \text{ mAh}\cdot\text{g}^{-1}$) and glucose ($63 \text{ mAh}\cdot\text{g}^{-1}$) at 0.1 C, at a higher current rate (at 1 C), carbon-coated particles using sucrose faded out quickly and carbon coated particles using fructose

had the higher capacity ($42 \text{ mAh}\cdot\text{g}^{-1}$) than using the glucose ($24 \text{ mAh}\cdot\text{g}^{-1}$). Thus, it was stated that because the carbon layer was more uniform and conductive in the carbon coating using fructose, these particles had higher stability at 1 C.

In the above-mentioned studies, it should be noted that besides properties like particle size or agglomeration state, the primary crystallite characteristics may also change in the base electroactive material. Therefore, with *in-situ* carbon coating, it is hard to attribute any electrochemical improvement solely to the effect of the carbon clearly. Although it can lead to carbon-coated active materials with enhanced electrochemical performance, there would always be a high risk of synthesizing fused and aggregated particles in the absence of a described reaction mechanism^[74, 75].

Another *in-situ* carbon coating study was done with phospho-olivine family of electroactive materials^[42] (LiMePO_4 , Me (transition metal) = Fe, Mn, Co, Ni or mixed transition metal ratio Mn_xFe_y) and indicated materials were synthesized with two different precipitation order, sequential (s) and coprecipitation (c) ((Figure 2.9 - a and b). During the precipitation stage, they were treated with the same amount of carbon source, CTAB, regardless of the mixing order. Resulting powders showed similarly shaped particles, with severe aggregation (Figure 2.9-c and d). Depending on type of the transition metal and the precipitation order, both adsorption and carbonization of the carbon source, CTAB, varied considerably with distinct carbonization efficiencies (η_c denotes the carbonization degree of the adsorbed carbon (Figure 2.9)).

Fe-containing electroactive materials exhibited higher adsorption and carbonization degree with more carbon content, others had almost no carbon. Uniform distribution of carbon was obtained in Fe and Mn containing electroactive materials, but there is uneven coating on Ni-containing active material (Figure 2.10). Homogeneity of the carbon layer changed depending on the transition metal type of the electroactive materials.

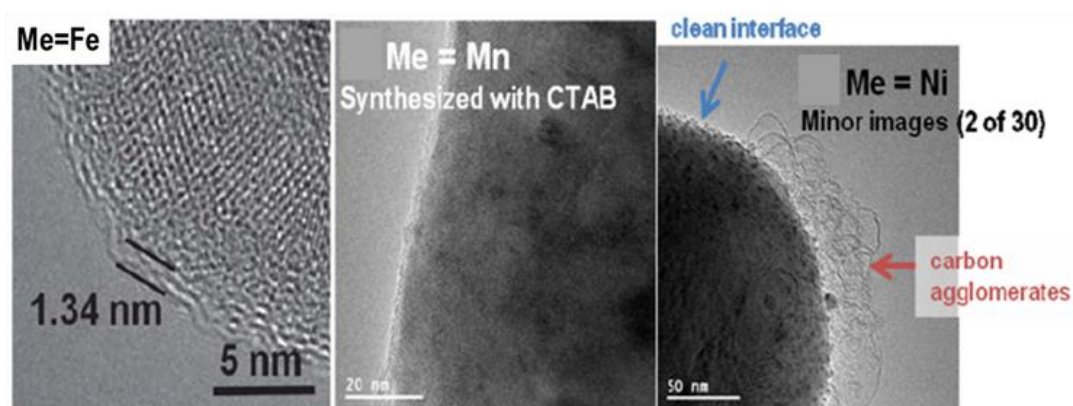


Figure 2.10. Carbon distribution on different electroactive materials^[42]

The *in-situ* carbon coating method is unique to the reaction medium, and the materials used. The coating procedure is specific to the synthesized material and has to be re-invented for almost any type of material to be coated^{[76],[42]}. Due to fact that in an electroactive material synthesis, there is no consensus on the method in practical use, it was concluded that this method is specific to materials used in the reaction, and it is tricky to adapt the formulation for various kinds of electroactive materials. Furthermore, *in-situ* carbon coating method obviously requires unique synthesis conditions with specific reagents for each type of the active materials.

In the *ex-situ* carbon coating, an electroactive material that is already synthesized is combined with a carbon source and a heat treatment employed for pyrolysis to take place^[4, 47]. Since the coating step is employed separately, electroactive particle characteristics (*i.e.*, particle size, shape and dispersibility) become independent from the carbon coating step and can freely be tuned^[77, 78]. For academic purposes, this

process also allows one to investigate the sole effect of carbon coating on the properties of electroactive particles as all the other characteristics of the particles can be kept constant^[77-79].

As a convenient option, sugar-based carbon sources were often used in this method as well ^[80-83]. In the study of Murugan *et. al*, as-synthesized nanorod shaped LFP particles were mixed with 18 wt.% of sucrose (with respect to LFP) and carbonized to achieve carbon coating^[84]. In Figure 2.11 (a) and (b), it was shown that carbon coated particles were dispersible and had homogeneous carbon layer. In another study using *ex-situ* carbon coating, it was stated that 9 wt.% sucrose was used to coat nanorod shaped LFP active materials and 149 mAh·g⁻¹ initial discharge capacity (at 0.1 C) was obtained after the coating process. It was seen in Figure 2.11-c and d that carbon layer around the particles were homogeneous, and particles were crystalline. These studies used similarly shaped and sized crystalline LFP particles, however different amount of sucrose was used in the coating solutions. Even though different amount of sucrose was resulted in dispersible particles, having high specific capacity, how to determine the amount of carbon sources is questionable.

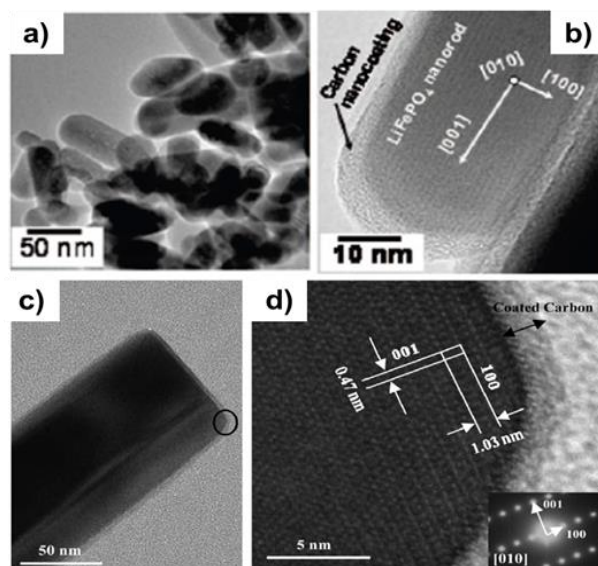


Figure 2.11. TEM and HRTEM nano-graphs of *ex-situ* carbon-coated LFP particles with varied amount of sucrose; (a) and (b) using 18 wt.% sucrose^[84], (c) and (d) using 9 wt.% sucrose^[85]

In the study of Su *et. al.*, *ex-situ* coating were done with various amounts of sucrose^[86] and it was reported that amount of the sucrose changed both the dispersion and specific capacity of the powders (Figure 2.12). Despite the same carbon source, different amount of it caused aggregation among particles, as it can be seen in the SEM images in Figure 2.12-a, b, and c.

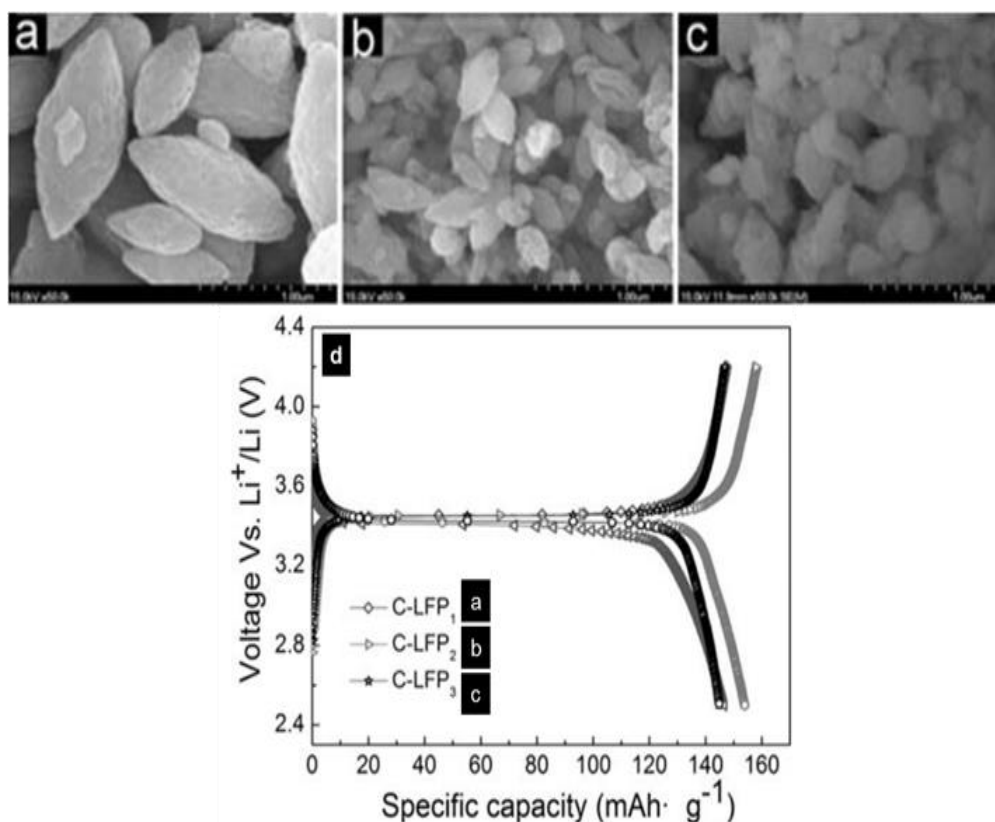


Figure 2.12. SEM images of *ex-situ* carbon-coated LFP particles with various amounts of sucrose a) 0.1 M b) 0.5 M and c) 1 M sucrose, and corresponding d) initial charge and discharge curves at 0.1 C rate of powders^[86]

The optimal amount of sucrose was chosen based on the powders' specific capacity. In Figure 2.12-d showed that carbon-coated particles coated with 0.5 M sucrose (Figure 2.12-b) had highest specific capacity ($\sim 154 \text{ mAh}\cdot\text{g}^{-1}$). However, no information was indicated related to carbon layer and its effects on agglomeration state of the powders. Similar situations were also valid for various kinds of carbon

sources. For instance, in the studies of Ding *et al.*^[87] and Xiong *et al.*^[88], LFP was carbon coated with different amounts of dopamine using *ex-situ* method. In Figure 2.13, particles can be seen as dispersible and carbon layer was uniformly distributed with similar thickness, between 2.5-3 nm. However, while there were carbon bridges between nanorod shaped LFP particles, nanosphere shaped particles were coated individually. Even though the same kinds of active materials were carbon coated with the same method and carbon source, the dispersion of the powders was not the same.

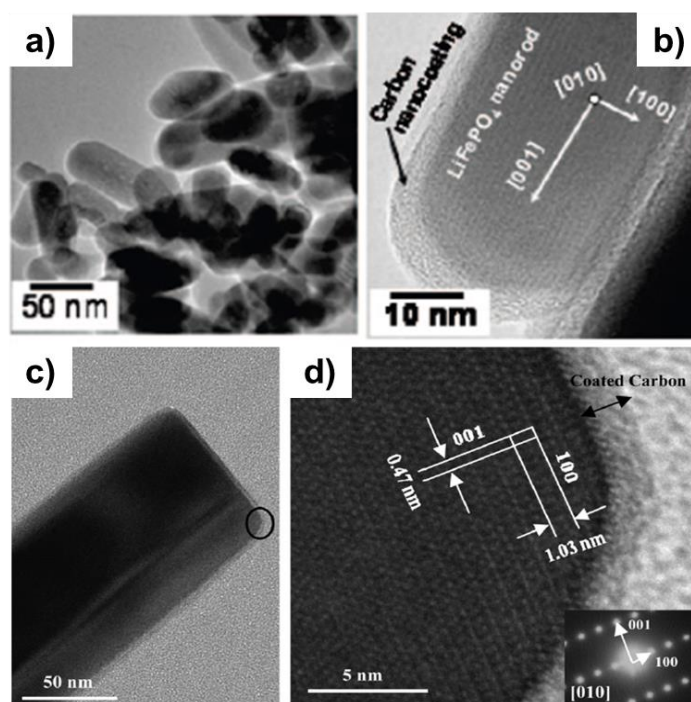


Figure 2.13. TEM and HRTEM images of the *ex-situ* carbon-coated (a), (b) nanorod shaped^[87] and (c), (d) nanosphere shaped^[88] LFP particles using dopamine, respectively

In the literature, it can be noticed that how the type and amount of the carbon sources were determined was unclear and is difficult to find the optimum amount of carbon with respect to synthesized dispersible particles, as it can vary with the type of the electroactive materials, type, and amount of the carbon source in either method. Although there are numerous studies investigating the carbon coating of

electroactive particles in the literature, there is no well-defined straight-forward methodology, neither for *in-situ* nor *ex-situ* coating methods, which can be applied to any material.

2.2.3 Pyrolysis in Carbon Coating

Pyrolysis is a thermal degradation/decomposition of carbonaceous material, mostly organic compounds, in an inert atmosphere (or very low oxygen/ vacuum) ^[89, 90]. During pyrolysis, large complex hydrocarbon molecules of the carbon source break down into relatively smaller and simpler molecules, *i.e.*, some of carbon and non-carbon atoms release in various forms and some remain as pyrolysis products in different forms. The product and the yield of pyrolysis change depending on the type and chemical structure of the precursor, its decomposition kinetics, applied pressure (if any), temperature, time, heating rate and thermodynamic stability of pyrolysis products ^[91-94]. Depending on these parameters, some of the pyrolysis precursors can be converted to solid carbon residues (carbon rich solid) or carbonaceous gaseous species or their mixture with pyrolysis^[91]. During pyrolysis of carbonaceous materials, sp^3 , sp^2 , and sp hybridizations of carbon take place. Depending on these hybridizations, it becomes possible to obtain carbon-based materials with the desired properties in terms of mechanical, thermal, optical, or electrical aspects ^[95, 96] and these carbon-based materials with outstanding properties can be used for various applications ^[97, 98].

Pyrolysis of any organic material, whether synthetic or biological, results in a carbon rich solid (carbonization), with the diverse chemistry and structure ^[95, 99]. Most of these carbon materials involve amorphous carbon structure (Figure 2.13-a), containing a mixture of sp^2 and sp^3 hybridized carbon atoms and has no long-range crystalline order throughout their structure and its surface typically has many reactive, dangling bonds. Some of these carbon materials, on the other hand, involves graphitic carbons (Figure 2.13-b), comprised of sp^2 hybridized carbon atoms, and display long range order. The surface of carbon materials including graphitic carbon

is more chemically stable than the amorphously structured counterparts. With this motivation, there are considerable number of attempts to synthesize and develop nanostructured graphitic carbon materials [98, 99].

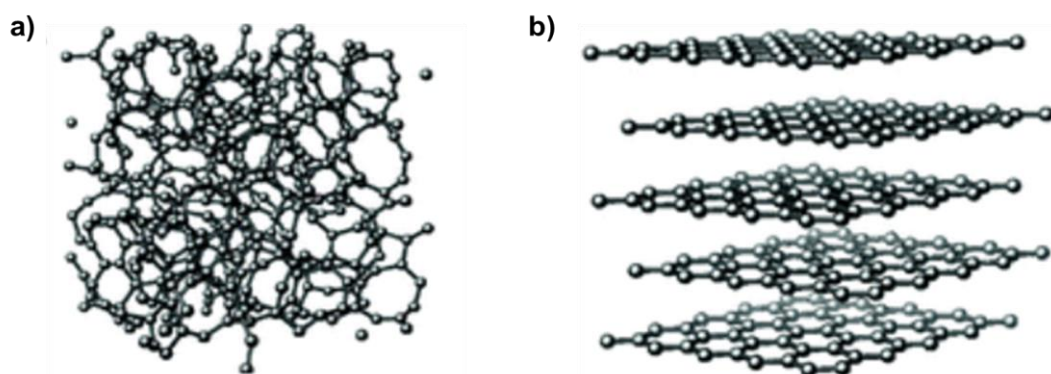


Figure 2.144. Carbon Structure of a) Amorphous and b) Graphitic Carbon^[99]

Nanostructured graphitic carbons are highly preferred in energy storage and conversion applications due to their high chemical stability, large accessible surface areas as well as high thermal and electronic conductivity. In the carbon coating of an electroactive material, for example, graphitic carbon structure is required primarily to obtain an electrically conductive layer and to enhance electrochemical performance. An amorphous carbon (disordered/non-graphitic) source can be converted into a graphitic carbon structure (ordered/ graphitized) with pyrolysis, which depends on the heating conditions and the nature of the precursor, therefore the pyrolysis parameters, such as temperature, time, and heating rate, have been extensively studied to obtain electronically conductive (graphitic) carbon.

The heat treatment temperature to be applied during pyrolysis has a direct effect on the crystal structure of the electroactive material and the electrical conductivity (graphitization) of the carbon coated on it. To this end, high temperatures are preferred [90, 91, 96, 100, 101]. However, in some cases, electroactive materials tend to decompose and lose its structure or unwanted byproducts are formed. In the study of Cheng *et. al.*^[100] $\text{Li}_4\text{Ti}_5\text{O}_{12}$ (lithium titanate oxide, LTO) particles were carbon coated

at different temperatures and it has been shown that increasing the temperatures resulted in higher electrical conductivity (Figure 2.15-a). The corresponding TEM nano-graphs obtained at 650, 800 and 900 °C (Figure 2.15- b, c, and d, respectively) showed that when the temperature was increased, the coating layer was much more clearly seen as a result of the increase in carbon graphitization. It was also indicated that no secondary phase was detected in the XRD analysis and LTO particles were stable at these temperatures, even at 900 °C.

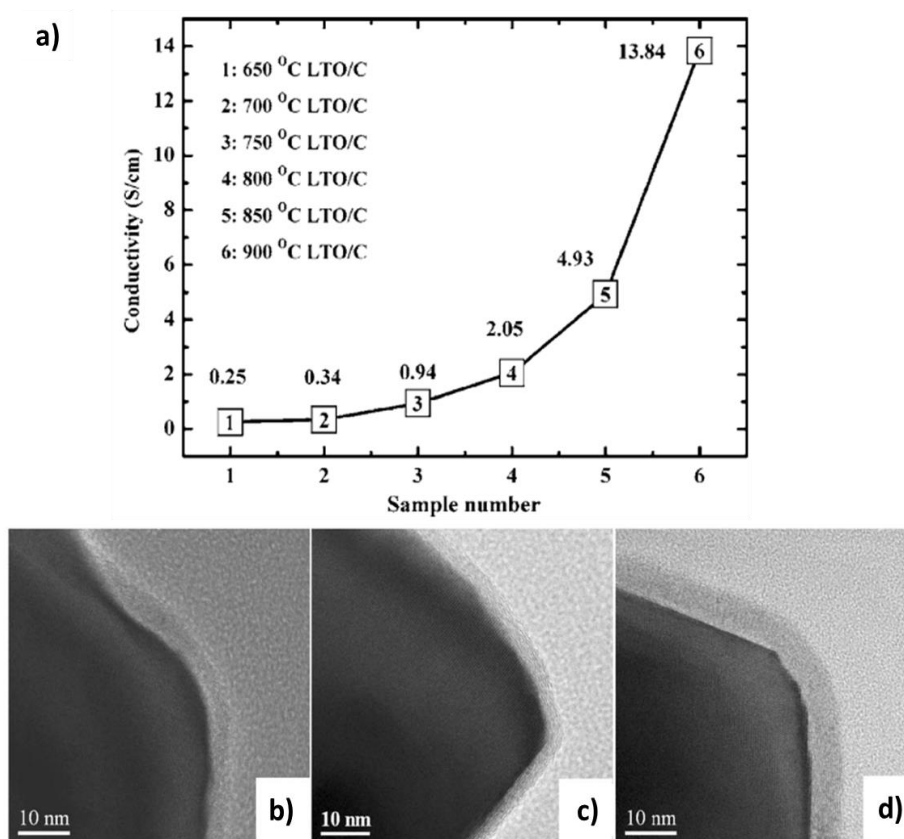


Figure 2.155. Electrical conductivity of carbon-coated $\text{Li}_4\text{Ti}_5\text{O}_{12}$ prepared under different temperatures a) and corresponding TEM nanographs of carbon coated $\text{Li}_4\text{Ti}_5\text{O}_{12}$ under b) 650, c) 800, and d) 900 °C temperatures^[100]

One of the studies investigated the effects of the pyrolysis temperature on the carbon coating on material using *in-situ* high-resolution transmission electron microscopy (HRTEM) under a nitrogen atmosphere^[102]. It was shown that LFP started to form

at 400 °C and did not show significant crystallographic changes up to 700 °C; however, at higher temperatures, LFP began to lose its crystalline structure and secondary phases formed. When the structure of carbon coated on the LFP was examined (Figure 2.16), the carbon also showed changes in this temperature range. The carbon layer formed on the LFP surface at 700 °C (Figure 2.16-a) was more homogeneous and graphitized than the one formed at 750 °C (Figure 2.16-b), therefore, it was expected to conduct electricity better. In the light of these results, the ideal temperature for carbon coating was reported as 700 °C to obtain homogeneous and conductive coating. The electrochemical performance of the bare and carbon coated LFP particles was also investigated before and after the heat treatment (Figure 2.16-c). While the bare LFP particles had 76 mAh·g⁻¹ specific capacity, this value increased to 94 mAh·g⁻¹ after the heat treatment at 700 °C for 6 hours. Under the same pyrolysis conditions, the carbon-coated particles exhibited the specific capacity as high as 141 mAh·g⁻¹.

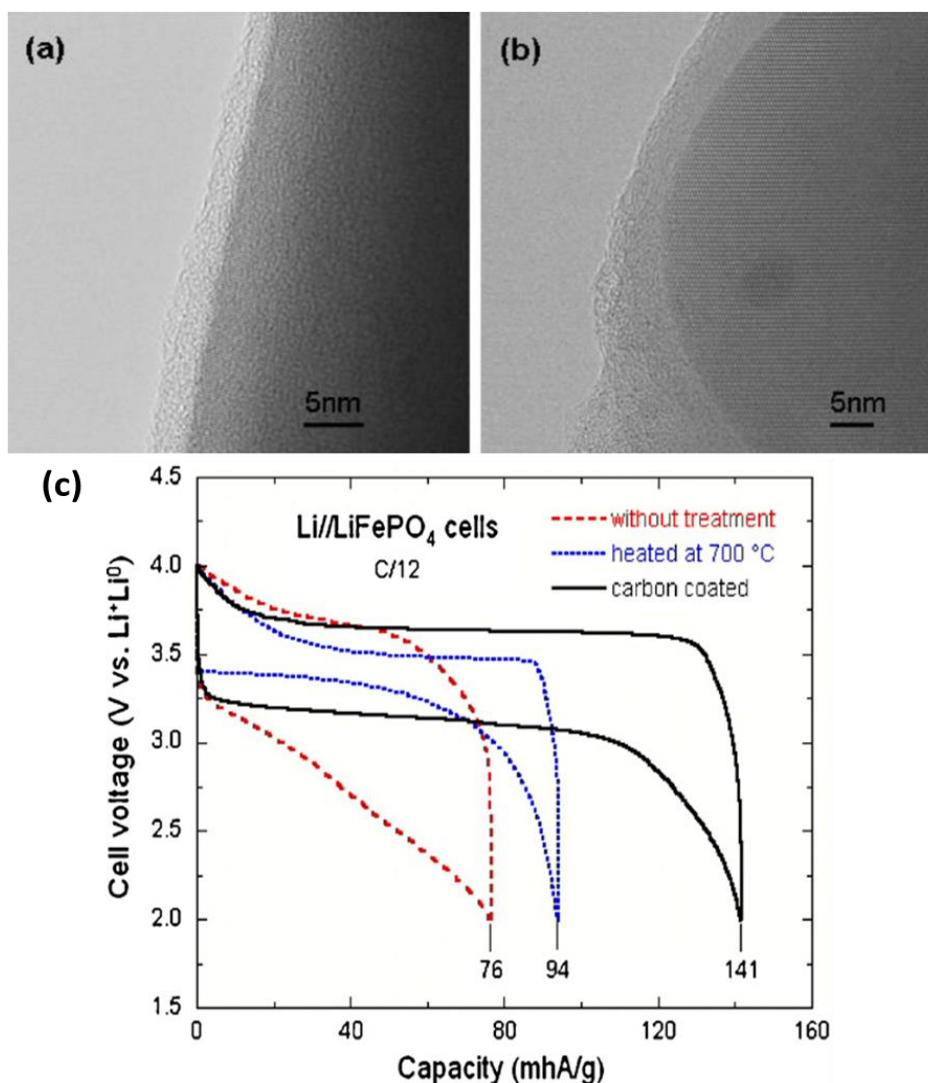


Figure 2.166. HRTEM images of carbon-coated LFP after pyrolysis performed at (a)700 and (b)750 °C and Electrochemical profiles at C/12, of the coated and uncoated LFP samples at pyrolyzed at 700 °C for 6 hours ^[102]

In addition to the temperature, the exposure time of the material to the pyrolysis conditions directly affect the electrochemical properties of the material. In the above-mentioned study^[102], The samples were kept at 700 °C for 180 minutes, however, it was also noted that the graphitization of the carbon source on the electroactive material started after only 45 minutes. In another, but similar study^[103], it was shown

that the carbon coating can be stable up to 700 °C but decomposes at higher temperatures, and it was observed that the carbon coating peeled off from the LFP surface as the LFP expanded and leaving hollow carbon sphere. In other studies presented in the literature, different temperature ranges have been specified for homogeneous carbon coating of LFP, and it has been stated that temperature may create different impurities and negatively affect battery performance depending on the type of impurity formed ^[102-108]. These studies are found critical as they explicitly showed that high temperature heat treatments were not only effective on the graphitization of the carbon source, but also changes the crystallinity of the electroactive material.

Reducing atmosphere used during carbon coating was also effective on the carbon coating mechanism and may cause the formation of impurities ^[106, 109]. In the study of Wang *et. al.* ^[107] it has been reported that the carbon coating properties changed according to the pyrolysis atmosphere, namely argon, argon/hydrogen, and argon/ammonia, when LFP particles ranging in size from 60 nm to 100 µm were used and heat treatment employed in the temperature range of 300-1000 °C. It was also reported that even for particles with the same chemistry and phase structure, the graphitization reaction and coating quality might differ with the difference in particle size or in crystal orientation. For this reason, the pyrolysis parameters should be optimized for each electroactive material.

Another important variable in the pyrolysis method is the heating rate. Heating rate ^[101, 110] determines the kinetics of carbon source decomposition, it does not only affect the yield of the carbon content ^[91] but also affects the fusion of the particles ^[111-113]. As the heating rate gets slower ^[114, 115] and temperature ^[116, 117] is kept high for long times, graphitization degree (high quality, conductive carbon) increases, but particles are prone to fusing and necks may form between particles. This problem results in aggregated particles and leads to low volumetric energy density in battery systems. In the study of Oh *et. al.*, *in-situ* carbon coated LFP particles were pyrolyzed at different temperatures and it was reported that while particles pyrolyzed at 800 °C

had $1.09 \text{ g}\cdot\text{cm}^{-3}$ tap density, the particles pyrolyzed at other temperatures of 650, 700, 750 and 850 °C led to particles having lower tap density ^[15]. Thus, determining pyrolysis conditions is vital in carbon coating process also due to its detrimental effects on the particle dispersibility. In addition, during the conversion of the carbon source to graphite, different gases may be released depending on the carbon source used. The formation of carbon-based gases, such as carbon monoxide (CO) or carbon dioxide (CO₂), reduces the amount of carbon that will remain on the particle, and even in some conditions can completely prevent the formation of the carbon coating. Studies in the literature show that carbon-containing gas formation is triggered at high heating rates ^[118]. Therefore, it may be necessary to reach the high temperatures required for the conversion of the carbon source to graphite on electroactive materials with low heating rates. Different heat treatment profiles can be applied to optimize the dwell time ^[91, 94, 119].

2.2.3.1 Pyrolysis Conditions and Secondary Phase Formation

Byproducts have a significant impact on the electrochemical performance of electroactive materials ^[103, 106-108]. Depending on which secondary phase is formed, their impacts on the battery performance may be positive or negative. Because these formations are mostly determined by the pyrolysis conditions, the optimization of the heat treatment is required in battery material synthesis.

. Rho *et. al.*^[109], for example, reported that LFP synthesis under inert or reducing atmosphere led to surface reduction of LFP and Li₃PO₄, Fe₂P and FeP phases were formed. The samples synthesized under argon atmosphere at 600 °C did not show any peaks of secondary phases at the XRD analysis, yet Mössbauer and XPS analyses showed the presence of both Li₃PO₄, Fe₂P and FeP phases originating from either carbothermal reaction and/or hydrogen reduction of carbon source. Depending on the reducing degree of the atmosphere and temperature, the amount of the Fe₂P changed and contributed greatly to the battery performance whereas FeP remained almost constant and did not affect the battery performance. It was also reported that

Li₃PO₄ phase was formed on the outer surface of the LFP particles unlike Fe₂P phase which was located in the cross section of the LFP particles. The authors did not present any relation between the presence of Li₃PO₄ and the battery performance. Yu *et. al.*^[120] claimed that Li₃PO₄ coming from synthesis conditions can be eliminated by an appropriate washing. When it was removed, specific discharge capacity of LFP increased. Therefore, they presented the Li₃PO₄ as an inactive material, decreasing the energy density of the LFP because of the volume it occupied.

The literature is controversial about the influences of second phases. While there are studies supporting the above-mentioned positive effects of the impurities on the electrochemical performance^[108, 121], there are also articles that claimed the opposite^[122, 123]. Some researchers reported that iron phosphide^[124] was formed frequently at high temperatures (> 600 °C), or various other impurities, *e.g.*, LiFe(P₂O₇)^[125], Fe (II, III) pyrophosphates or phosphates Li₃Fe₂(PO₄)₃^[126] and Li₃PO₄^[1], might be formed depending on the pyrolysis conditions.

2.2.3.2 Type of The Carbon Source and Pyrolysis Parameter Optimization

A few studies attempt to use already synthesized, highly graphitized carbon sources in the carbon coating process of electroactive materials so that there is no need to apply high pyrolysis temperature to increase the graphitization degree of the carbon sources. Inorganic carbon sources (*e.g.*, carbon nanotubes, graphene, acetylene black, *etc.*) offer higher carbon quality (higher graphitization degree, higher electrical conductivity) than the organic carbon sources (*e.g.*, sucrose, glucose, lactose, citric acid, *etc.*, which are mostly amorphous), therefore, the efforts have been made to coat electroactive materials with already graphitic carbon. Studies showed that this approach is not as effective as using organic compounds and subsequent pyrolysis of this source to carbon, because the organics can cover the surface of the particles more homogeneously. While inorganic carbon materials can form a three dimensional (3D) conductive network, organic carbon materials may still be needed to form local conductive paths between particles` surfaces. Organic

compounds usually offer the advantage of a uniform coating layer structure (homogeneity in thickness, full coverage) on electroactive materials when the conditions were optimized and can be easily transformed into carbon during the pyrolysis process, but the carbon quality (including conductivity and graphitization degree) is difficult to control. Since the chemical structures of the organic compounds are different, the chemistry of carbonization during pyrolysis varies. While some carbon sources are easily graphitized (graphitizing or soft carbon sources), some carbon-based materials resist graphitization (non-graphitizing or hard carbon sources). Even though the same pyrolysis procedure was applied to those materials, the response of the carbonization changes. In the study of Jiang *et.al.* [127], LFP particles were carbon coated with asphalt (soft carbon source) and glucose (hard carbon source) at 700 °C for 6 hours in a vacuum oven.

As observed in Figure 2.17-b and 2.17-c, the soft carbon coating (asphalt), was more uniform than the hard carbon coating (glucose). The analysis of the graphitization on the carbon coated samples analyzed by Raman spectroscopy and asphalt coated sample showed higher graphitization degree than the glucose coated LFP particles.

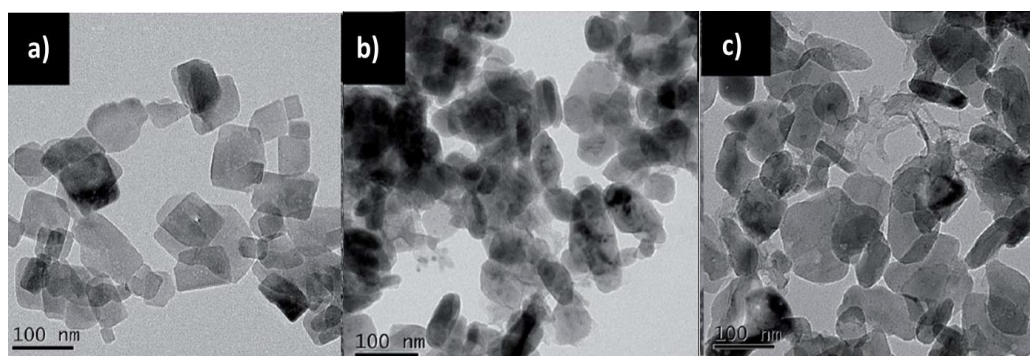


Figure 2.17. TEM images of a) bare LFP particles, and carbon coated LFP particles using b) asphalt, c) glucose carbon sources [127]

In line with these results, while the former one had $156.3 \text{ mAh}\cdot\text{g}^{-1}$, the latter one had $131 \text{ mAh}\cdot\text{g}^{-1}$ at 0.1 C. Better electrochemical performance and more uniform carbon layer were obtained with soft carbon. On the other hand, even though particles were dispersible before (Figure 2.17-a), they were aggregated after carbon coating process

regardless from the carbon sources of being asphalt or glucose, and thus have limitations in the utilization of the particles when used in cathode. Different carbon sources do not necessarily lead to the same graphitization degree due to differences in the bonding characteristics, network forming capabilities and the type of the defects forming during the pyrolysis.

2.2.3.3 Substrate Effects on Pyrolysis

In order to reduce the pyrolysis temperature depending on the carbon source and the electroactive material used, and to reduce the energy loss during production, catalysts can be used during the carbon coating. In this context, the additives containing iron (such as iron nitrate, ferrocene) or polyaromatic material (such as pyromellitic acid) were used during carbon coating and these additives changed the amounts and quality of carbon remaining on the surface of the electroactive material [128, 129]. Although iron is the most studied catalyst for graphitization, many other elements are known to drive graphitization. Transition metals, especially iron, cobalt and nickel, are known to be the most efficient. Among these three metals, the highest catalytic activity is normally found for iron, followed by cobalt, and then nickel. In the same studies, it was also reported that different amounts of catalyst and polyaromatic additives during the heat treatment required for carbon coating differ in the quality of the produced particles, thus different conductivity values, and thus the specific discharge capacity, can be obtained. Furthermore, the presence of heterogeneous atoms in the carbon layer, such as metal (Pt, Fe, Co, Ni, Zn, and Mo) and some nonmetal atoms (B, N, O, S, and P), contributes to the electrical conductivity and specific energy density of the carbon [98, 120]. These elements modify the electron structure of carbons, improving their performance in energy storage materials. Nitrogen (N) doping into sp^2 hybridized carbon materials, in particular, tailors the local electron structures and/or induces substitutional defects in carbon materials, thereby increasing their chemical activity. It was reported that existence

of N, for instance, in the carbon layer can improve the electrochemical performance of the electroactive materials ^[88, 130].

2.2.3.4 Advantages of High Graphitization Degree

Graphitization degree of the carbon source is advantageous in different aspects aside from the electrical conductivity. Graphitized carbon presents fewer defects in the structure. Accordingly, the highly graphitized carbon layer offers higher ionic transport as well as electrical transport with more ordered structure of the carbon layer^[131]. Moreover, poorly graphitized carbon layer has some functional groups on the surface, and these groups causes high viscosity in water-based electrode slurries due to interactions between the functional groups and water. It was stated that the commercial electroactive materials, having different graphitization degree showed inconsistent flow behavior even if the powders were supplied from the same company ^[132-135] (Figure 2.18- a and b). Therefore, the graphitization degree of the carbon layer is essential for the processability of the electrodes.

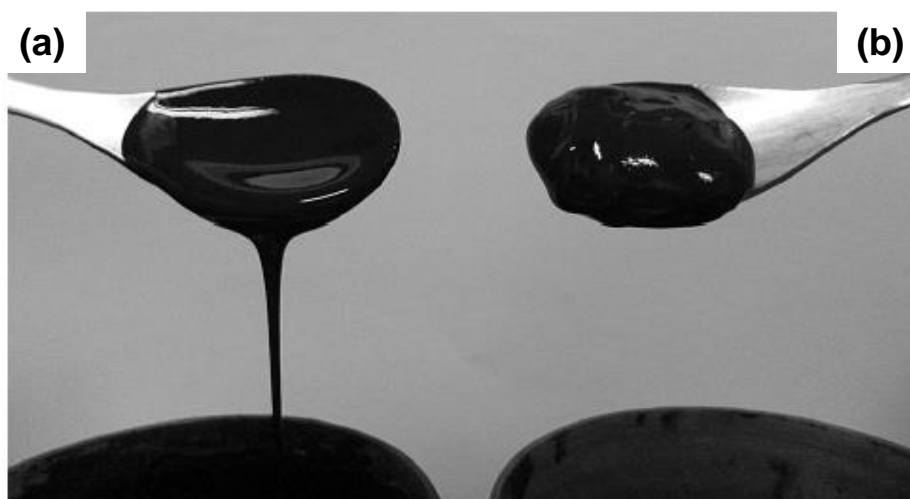


Figure 2.18. Commercial LFP powders supplied from the same company, showing different flowability; the former was suspended in the aqueous slurry (a) and the latter was gelled (b) ^[135]

In order to obtain individually carbon coated electroactive materials having high electrochemical performance and better processability, take-home messages of this section can be summarized as following:

- The carbon source should be selected appropriately,
- The pyrolysis process variables (atmosphere, temperature, heating rate, pyrolysis time) should be studied carefully,
- The crystal structure of electroactive materials should be examined before and after pyrolysis for phase purity,
- Additional substrate/ catalyst used in the carbon coating might be helpful to adjust the temperature and offer high graphitization degree.

2.3 Volumetric Energy Density of a Battery System and Properties of Carbon Coated Electroactive Materials

Volumetric energy density of a battery system is the amount of energy that can be delivered from per unit volume of electrode materials and one of the most critical design parameters for new generation batteries^[136, 137]. Increasing the volumetric energy density of the electrode is critical, because when the same amount of energy can be stored in smaller volume, the electrode occupies less space, the overall size, weight, and manufacturing cost of the battery decrease. Moreover, more energy can be stored in the same volume, therefore designing smaller devices with longer battery life becomes possible. In electrical vehicles, for example, longer distances can be travelled without a need for charging.

One way to increase the volumetric energy density is to pack the electroactive particles more densely, i.e., increasing its tap density. The tap density, the ratio of the mass of the powder to the volume it occupies, mainly depend on the size, size distribution and the morphology of the particles. Therefore, the particle design become a focus in studies to improve volumetric energy density.

The particle size, for example, inversely related to the tap density. Nano-sized electroactive particles have advantages due to their high-rate capacity and cycling performance originating from the shortened Li-ion transfer paths within the particle. However, for the same amount of particles, the tap density of nanoparticles are much lower compared to the micron-sized counterparts because of the more prominent interparticle interactions and higher agglomeration tendencies^[138]. Oh *et. al.* showed that dense carbon coated micron-sized LFP particles comprised of nano-sized particles (200-300 nm) had the tap density of 1.5 g·cm⁻³. This density value is much greater than the tap density value obtained for common nano-sized LFP, which is about 1.0 g·cm⁻³ ^[18, 139]. Even though they exhibited similar rate capability, the tap density was higher when the particles were packed efficiently^[140].

The study of Zhong *et al.* ^[141] showed the importance of particle size distribution on the tap density. In this study, first, two different Fe³⁺ precursors were used, and the resulting particles exhibited two different size distributions. Then, in one case the particles were mixed in different proportions and the tap density of 1.40 g/cm³ were obtained. When the micrometer-sized particles were used, on the other hand, the tap density was 1.19 g/cm³. This density difference was explained with the fact that the voids in the packs of micron-sized particles (Figure 2.19-b) were filled with nano-sized particles in the mixed particle case (Figure 2.19-a) and resulted in denser packing, and thus, higher tap densities.

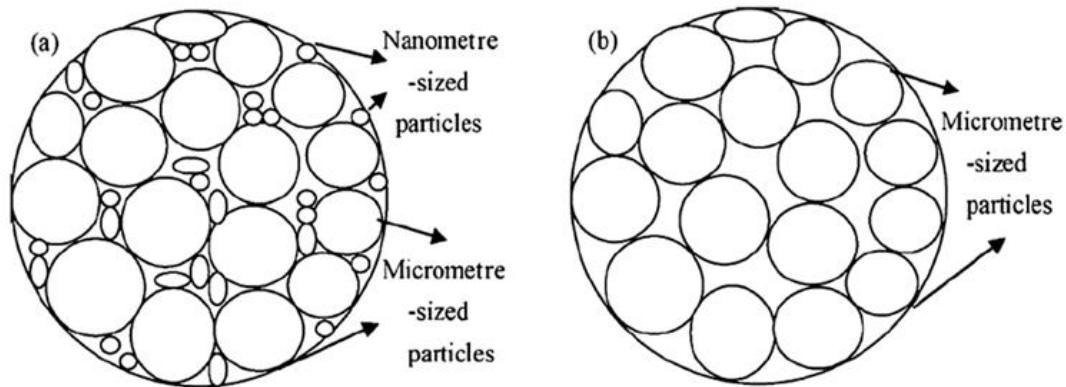


Figure 2.19. Particle size distribution effect on tap density with (a) higher packing in the presence of smaller particles that fills the spaces between particles and (b) less packing in the absence of small particles ^[141]

The particle morphology is also important in achieving high performance and volumetric energy density. The particles with low aspect ratio, particularly the spherical ones, lead to higher tap densities because of their high packing efficiencies^[139, 142]. In Liu *et al.*'s study ^[143], tap density of carbon coated 1 micron-sized spherical LFP and $\text{LiFe}_{0.9}\text{Mg}_{0.1}\text{PO}_4$ particles was measured as 1.75 and 1.77 $\text{g}\cdot\text{cm}^{-3}$ (theoretical density of LFP is $3.68 \text{ g}\cdot\text{cm}^{-3}$) and specific discharge capacities were recorded as 148 and 157 $\text{mAh}\cdot\text{g}^{-1}$ at 0.1 C (theoretical capacity of LFP = 170 $\text{mAh}\cdot\text{g}^{-1}$ at 1 C), respectively.

In the literature, the studies regarding to tap density of electroactive materials, the main focus was on particle design and the efforts made to synthesize perfect sized (in the micrometer range) and shaped (commonly spherical) individual, secondary particles to obtain a high tap density. On the contrary, there are examples where non-spherical particles were used yet high tap density values could be obtained based on their aspect ratio^[144-146].

In fact, one of the most critical properties of the particles that affects the tap density is the state of agglomeration of the particles. In an aggregated particle system, the size, shape, and size distribution of aggregate particles rather than individual particles becomes crucial in packing of particles. Fine powders have the tendency to form agglomerates or aggregates (during synthesis) [70]. Hard agglomerates (aggregates) which do not break up during processing leads to a nonuniform size distribution, which results in low tap density [71-73]. Therefore, when particles are severely aggregated, efficient packing cannot be obtained (Figure 2.19-a and b). Conversely, using dispersible particles in an electrode would provide higher solids loading per unit volume due to their narrower size distribution.

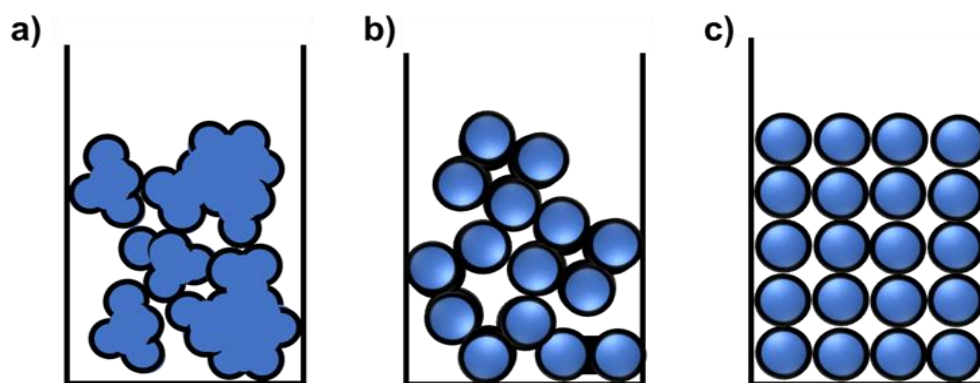


Figure 2.20. Tap density of carbon coated particles in the forms of a) aggregated, b) carbon bridges between particles and c) dispersible/individual (blue colored forms and black colored thin forms represent electroactive material and carbon layer, respectively)

The carbon-coated particles are mostly in the form of clusters: they are either composed of secondary particles that are chemically connected, then carbon coated (Figure 2.20-a) or they were dispersible at the beginning but agglomerated after carbon coated process through carbon bridges formed between particles (Figure 2.20-b). Even though the carbon coating step seems to have a direct effect on the agglomeration state of the electroactive particles, there is no study in the literature explicitly investigating the relation between carbon coating and the agglomeration

state of the particles. Even though there were relatively well carbon coated dispersible particles in the literature ^[17, 83, 86-88, 147], as schematized in Figure 2.20-c, the carbon coating procedure was overlooked, and commonly optimized to increase specific capacity of particles, rather than increasing their volumetric energy density. As discussed before, in order to achieve high volumetric energy density, the agglomeration state of the particles is critical because the packing density of the particles are determined based on the agglomeration state of particles (the characteristics of the secondary particles) rather than the characteristics of primary particles ^[148, 149]. Similarly, as the shape of the irregular aggregates or agglomerates deviates from sphericity, the tap density of the particles are significantly decreased, and a further reduction is observed for randomly packed systems. Alignment of the dispersible particles enables the system to have a high tap density^[150]. Dispersible (*i.e.*, individual) particles are required to obtain high tap density in electrodes.

The presence of carbon coating, on the other hand, has an adverse influence on the tap density. Since the carbon has lower specific density than electroactive materials and it is an inactive material, it decreases the tap density of electroactive materials. In Chang Z. *et al.*'s study^[151], it was found that the tap density of carbon-coated LFP particles decreased from 2.15 to 1.66 g·cm⁻³ with an increase in carbon content from 3 wt.% to 9 wt.%. Even though the carbon content effect on the electrochemical performance of the particles was reported, the impact of carbon content on the particle dispersion was not examined explicitly in this study.

Among samples with various carbon contents, the highest electrochemical performance attained with 7 wt. % carbon, which resulted in tap density of 1.8 g/cm³. The most of the commercially available electroactive materials reports the carbon content of 1-5 wt.% ^[135], tap density less than 1 g·cm⁻³ and specific discharge capacity of 120-160 mAh·g⁻¹ ^[18]. Particles with higher carbon content leads to capacity loss due to the dead mass ^[4, 79]. Thus, it might be said that uneven and irregular carbon coating results in low specific and volumetric capacity, thus amount and uniformity of the carbon should be optimized properly.

All in all, it is concluded that specific capacity and volumetric energy density can be increased by special particle designs, but there is a need for a common strategy that can be applied to all electroactive materials during carbon coating. Although carbon-coating of particles have been widely studied and even applied in the industrial scales, the relation between the carbon coating process and the agglomeration of particles during carbon coating is still a gap in the literature.

2.4 Colloidal Principles

2.4.1 Colloidal Stabilizations

Colloidal principles are employed to obtain homogeneously dispersed particle systems. Stability of a colloidal system can be achieved by tuning the interparticle interactions^[152]. When the total interparticle interaction is repulsive enough, particles resist to agglomerate, and more homogeneous dispersions can be obtained. Depending on the surface properties of particles, proper stabilizing agents can be selected. There are three main mechanism that can be used to stabilize particles in a solvent; electrostatic, steric and electrosteric stabilizations (Figure 2.20)^[153].

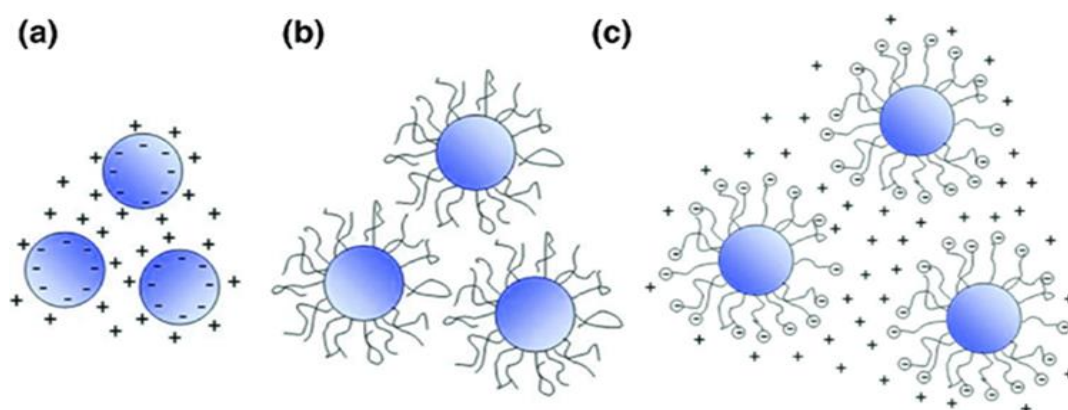


Figure 2.21. Colloidal stabilization methods: a) Electrostatic b) Steric and c) Electrosteric Stabilization^[153]

Electrostatic stabilization is the counterbalancing the attractive (van der Waals) forces by the repulsive (coulombic) forces acting between charged particles. Surface charge on the particles is either created or modified by pH adjustment or surface functionalization. At the end, particles become surrounded by the same positive or negative charges which leads to electrical repulsion between the particles and prevent their agglomeration (Figure 2.21-a).

Steric stabilization is creating repulsive forces between particles using organic molecules. Basically, the organic substance either dissolves in the suspension or adheres onto the surface of the particles and, by occupying space (as a physical barrier) between them, keeps the particles apart (Figure 2.21-b).

Electrosteric Stabilization is a combination of the electrostatic and steric stabilization methods. In this concept, polymers are used and depending on the pH, dielectric properties, and ionic strength of the solvent^[154], stabilization can be achieved (Figure 2.21-c).

The interactions used in the colloidal stabilizations could be applied in carbon coating. In the study of Wei *et. al.*^[155], for example, it has been shown that, full wrapping graphene oxide nanosheet (GON) onto electroactive material of LFP was driven by electrostatic interactions. For this purpose, two type of coating processes were designed. In Figure 2.22-a, it has been shown that the LFP and the carbon source, GONs, were oppositely charged, and thus, the full encapsulation of LFP would be provided by electrostatic interactions between LFP and GONs. Based on this scenario, the LFP particles which are negatively charged at $\text{pH} < 7$ was first coated with positively charged CTAB in acidic aqueous solution. Then, negatively charged GONs were added and wrapped the LFP surfaces. After GONs were converted into graphene nanosheets (GNs) by hydrazine, the leftover surfactant was removed by washing and thermally breakdown when heat treated at 600 °C for 2 hours. Afterall, it was stated that these electrostatic interactions resulted in perfectly GO wrapped LFP particle (Figure 2.22-c). In the second design (Figure 2.22-b), a similar route was followed, except the CTAB part. Then, partially coated particles

were obtained (Figure 2.22-c). It was reported that the insufficient driving force between GO and LFP was the reason to obtain partial coating. Even though full carbon coverage of LFPs were obtained by managing the electrostatic interactions, as seen in TEM nanographs, the resulting particles were chemically fused, and not dispersible, therefore they expected to have low tap density. Moreover, how the amount of CTAB or GONs was decided to be used to fully cover the particles surface was not reported.

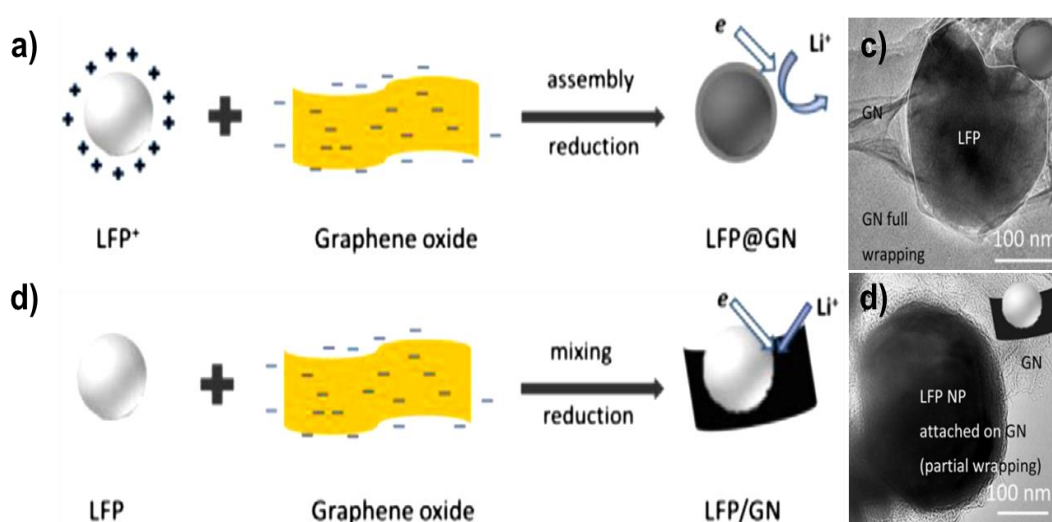


Figure 2.22. a) Full and b) Partial graphene wrapping of LFP particle^[155]

2.4.2 Surfactants

Surfactants are special molecules which are commonly used in colloidal stabilization^[156-160]. Surfactants exhibit amphiphilic characteristics due to their hydrophilic head groups and hydrophobic tail groups (Figure 2.22).

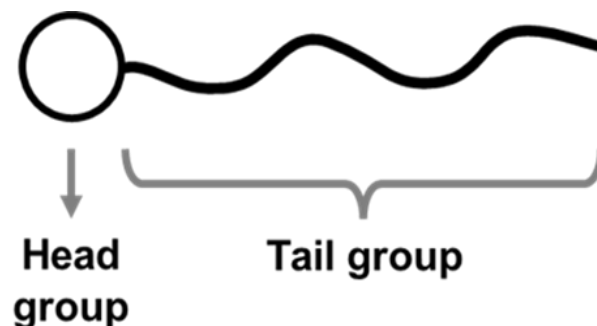
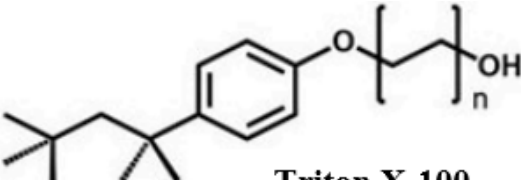
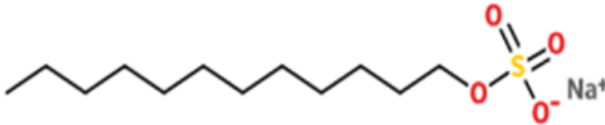
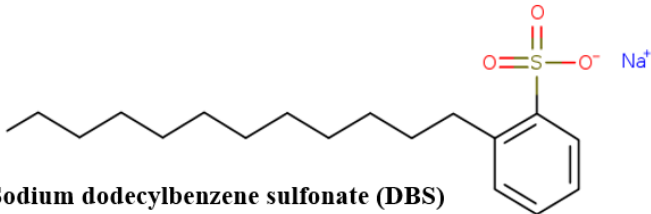
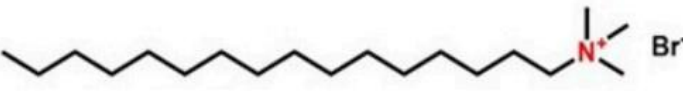
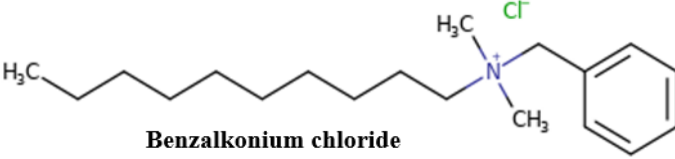
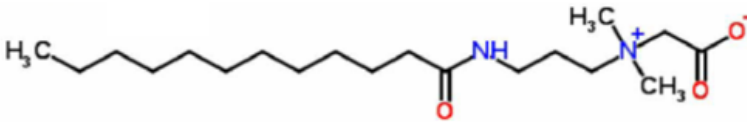


Figure 2.23. Structure of a surfactant monomer (unimer)

Head group molecules are polar, hydrophilic functional groups, whereas hydrophobic parts are nonpolar, hydrocarbon chains (alkyl chains). Depending on the type of the surfactant hydrophobic tail varies in length and number.

Surfactants can be classified into four groups based on their head group charge; non-ionic, anionic, cationic and zwitterionic ^[161, 162]. Non-ionic surfactants do not carry any charged groups and they are distinguished amongst themselves based on the length of the chain and commonly used examples include Triton X-100 (polyethylene oxide, $C_{14}H_{22}O(C_2H_4O)_n$ ($n = 9 - 10$), Tween 80 (Polysorbate 80, $C_{64}H_{124}O_{26}$) *etc.*. Anionic surfactants have a negatively charged head group and SDS (Sodium dodecyl sulphate, $NaC_{12}H_{25}SO_4$) and DBS (Sodium dodecylbenzene sulfonate, $C_{18}H_{29}NaO_3S$) can be given as examples, Cationic surfactants have a positively charged head group and CTAB (Cetyltrimethylammonium Bromide, $C_{19}H_{42}BrN$) and benzalkonium chloride ($[C_6H_5CH_2N(CH_3)_2R]Cl$) are the most common examples. Zwitterionic (Amphoteric) surfactants have both positively and negatively charged groups. Depending on the pH of the solution they can act as either like cationic or anionic surfactants (e.g., CAPB (cocamidopropyl betaine, $C_{19}H_{38}N_2O_3$) *etc.*). The corresponding chemical structures of the most commonly used surfactant examples for each group are presented in Table 2.1.

Table 2.1 Examples of Some Common Surfactants

Type of Surfactant	Chemical Structure	Ref.
Non-ionic	 <p>Triton X-100</p>	[163]
Anionic	 <p>Sodium dodecyl sulphate (SDS)</p>	[163]
	 <p>Sodium dodecylbenzene sulfonate (DBS)</p>	[164]
Cationic	 <p>Cetyltrimethylammonium Bromide (CTAB)</p>	[165]
	 <p>Benzalkonium chloride</p>	[166]
Zwitterionic	 <p>Cocamidopropyl betaine (CAPB)</p>	[167]

In a bulk solution, behavior of a surfactant is strongly affected by the type and amount of the surfactant in the solution. For example, when a surfactant is added into water, firstly it dissociates and hydrophilic head groups of the surfactants become charged, if soluble in water. After a threshold concentration (changing for each surfactant) of surfactants in a solvent was reached, surfactant monomers self-assemble into clusters. These clusters are called micelle and the threshold concentration is called critical micelle concentration (CMC) (Figure 2.24).

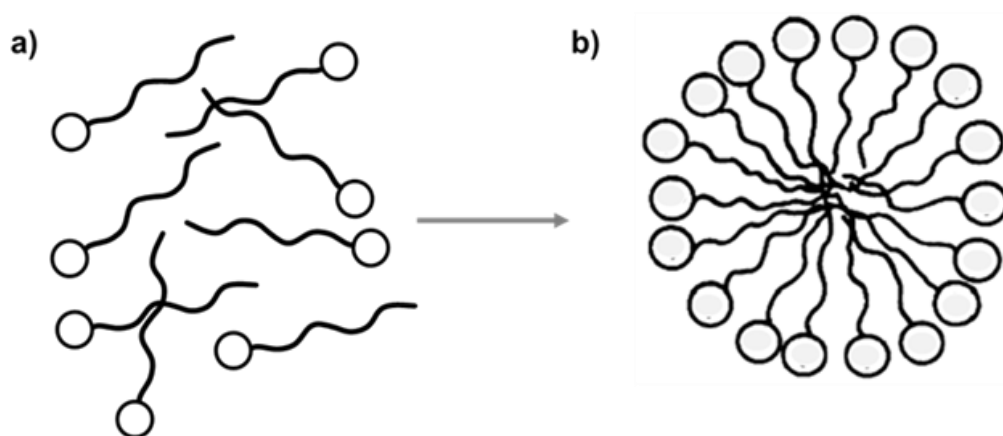


Figure 2.24. Structural forms of surfactant a) molecule and b) micelle in a polar solvent

The direction of the surfactant molecule is directed by the interaction of between themselves and the solvent molecules. In the case of water, which is a polar solvent and since the tail group of the surfactant is nonpolar, surfactants self-assemble in such a way that non-polar groups are directed to each other and protect themselves from the interaction with polar water molecules. The hydrophilic head groups of the surfactant are exposed to the bulk solution, since they are polar and favorably interact with polar water molecules. In the case of a nonpolar solvent, the micelle would be assembled in the opposite direction, *i.e.*, the hydrophilic head groups would be clustered towards each other, and the hydrophobic tails of the surfactants would be exposed to the non-polar solvent. This structure is called reverse micelle structure. The behavior of a surfactant is mainly dependent on these interactions. Depending on the chain length, branching and (if any) aromatic groups of a surfactant, its

hydrophobicity, solubility, micellization tendency (e.g., CMC for CTAB and SDS are 1, 8.2 mM, respectively^[163]), and adsorption efficiency vary^[160]. Therefore, surfactants offer a wide range of application areas^[160]. With the diverse chemical structures and properties surfactants offer, they were used in carbon coating of electroactive materials. To illustrate, type and amount of the surfactants are useful in regulating the graphitization degree of the carbon layer. In Li *et al.*'s study^[168], carbon coated LFP, electroactive materials, were synthesized with solid state reaction using surfactants, Tween 20, Tween 40, and Tween 80, as carbon sources. Graphitization rate of the carbon layer changed depending on the chain length of the surfactant used. It was indicated that the surfactant with shorter alkyl C-C chain length formed more graphene-like carbon during pyrolysis and consequently more graphitized carbon-coated particles exhibited better electrochemical performance. Although the surfactants were only used in few studies as a carbon source to coat electroactive materials^[169-173], all these studies were used *in-situ* coating methods and the advantage of specific interactions between a surfactant and electroactive materials on coating process were not designed or discussed explicitly.

2.4.3 Interparticle Interaction Control with Surfactants and Colloidal Stabilization in an Aqueous Medium

Surfactants can interact with a variety of hydrophobic and hydrophilic surfaces^[174]. Since they have two differently behaving groups, they can modify different kinds of surfaces. For example, when a charged surfactant is added in an aqueous environment, including charged particles, the interaction between the surfactant and particles is determined by colloidal principles. If the particles and the surfactants are oppositely charged, the interaction between them initially is driven by the electrostatic attractions. Surfactant molecules attach to the surface of the particles from the ionic head group and tail group (alkyl chains) exposed to the bulk solution. Addition of more surfactant molecules to the system continues to selectively interact with the particle surface due to the electrostatic attractions. After a certain

concentration of the surfactant, particle's surface is covered by a single layer of surfactant. The head group interacts with the particle's surface making the tail group exposed to the bulk solution. during monolayer coverage, the hydrophobicity of the particle's surface increases, and these hydrophobic particles destabilized in the polar aqueous media and separated. When additional surfactant molecules are introduced to the system, they preferentially orient in such a way that head groups are extended towards the bulk solution while the tail groups are interacted with the monolayer's tail group. After the bilayer formation, the system is stabilized again and possess an opposite potential with respect to the initial surface potential. In line with this, results of a thorough study conducted on assembly structures of CTAB on negatively charged citrate capped gold nanoparticles proposed that CTAB was adsorbed on the gold nanoparticles initially by forming an incomplete monolayer. With increasing concentrations of CTAB, a complete monolayer coverage was possible. After monolayer formation, assembly structure passed through an imperfect bilayer, perfect bilayer, a combination of perfect bilayer and micelles, with ever increasing CTAB concentrations with respect to the particles^[175] (Figure 2.25). It was indicated that after the optimization of the CTAB concentration the stability of the system was achieved.

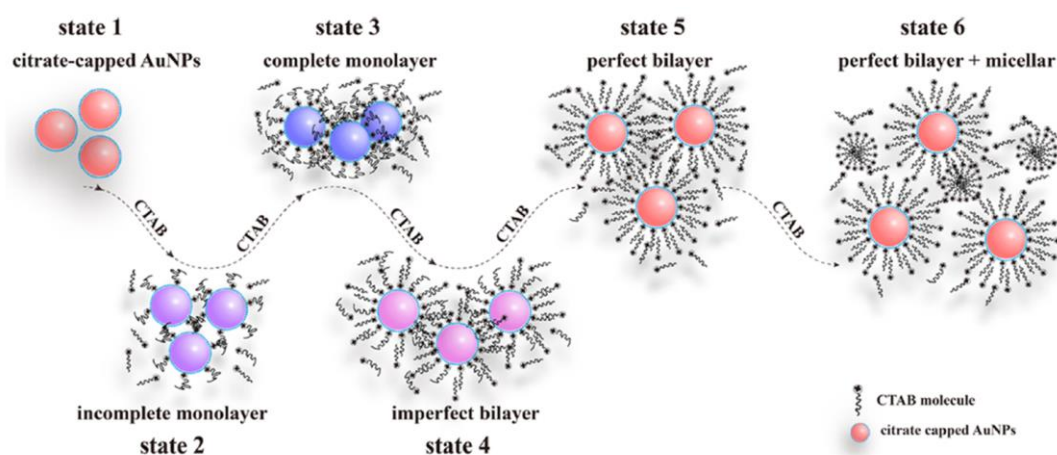


Figure 2.25. Assembly of CTAB onto citrate capped gold nanoparticles^[175]

In the case of oppositely charged particles and surfactants, this mechanism is dominant and for each type of surfactants there would be different mechanism to follow ^[176-179]. The main condition for stability against agglomeration starts by defining the possible interactions between the components and manipulating them accordingly. Further, these colloidally stabilized particles are surface modified and in a way the particles become coated with a carbon rich layer after stabilization.

2.4.4 Zeta Potential

The zeta potential is a commonly utilized metric to predict the stability of a suspension ^[152, 180-182] and understand charge on a particle surface. When a particle is dispersed in a liquid, two layers exist around the particle; the inner layer (Stern layer), where the ions are tightly bonded, and the outer layer (Diffuse layer), where the ions are loosely connected. There is a hypothetical border within the diffuse layer, where ions and particles are stable, and ions within this border moves with the particle as the particle moves in solution. The zeta potential is the potential at this interface called slipping plane (Figure 2.26).

The magnitude of the zeta potential provides information about the system's stability. In general, when zeta potential is (ζ -pot.) between -30 and +30 mV, the system is unstable. When zeta potential is more than +30 mV or less than -30 mV the system is electrostatically stable^[180]. At stable regions, there is often a sufficient repulsive force between particles that they can stay separated. In an unstable suspension on the other hand, particles that have low zeta potential tend to come together and sediment quickly ^[180, 183]. As such, the changes on a particle surface can be analyzed by changes in zeta potential measurements.

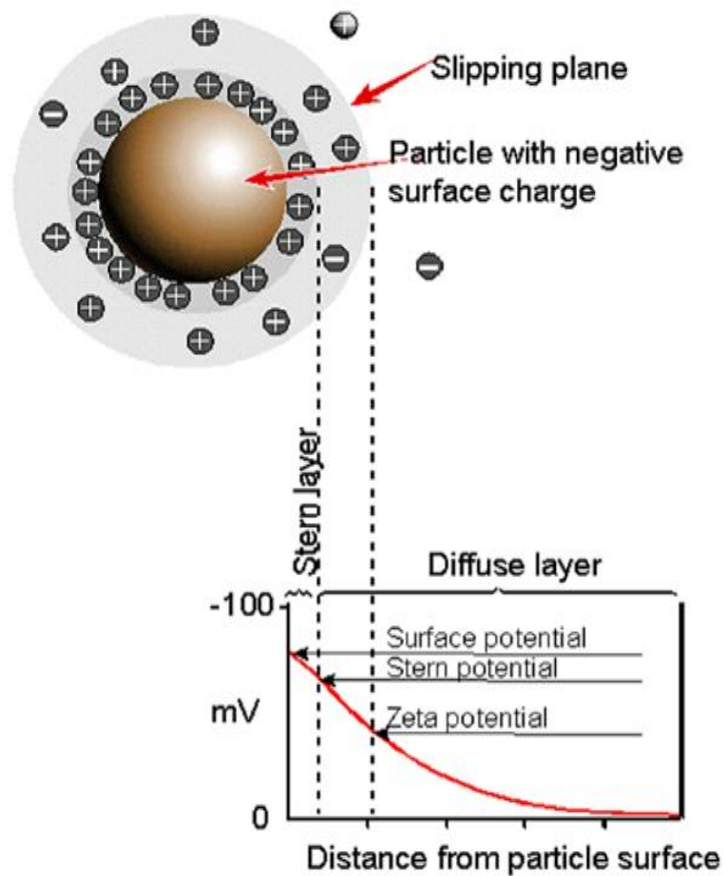


Figure 2.26. Schematic illustration of Zeta Potential ^[184]

By analyzing the zeta potential of a particle while increasing the concentration of a surfactant that has oppositely charged head groups, it should be possible to detect the surface assembly modes of the surfactant and detect the conditions of stability that would be reached upon bilayer formation. The quantitative determination of the optimum amounts of carbon source (*i.e.*, surfactant) can be useful when aiming to achieve the individual carbon coating.

2.5 Thesis Objectives

Carbon coating plays a crucial role in particle agglomeration state and affect the volumetric energy density of a battery system. Since a good dispersion of the particles is required for higher volumetric energy density, the carbon coating process should not intermingle with an already established agglomeration free particle system. Accordingly, it is hypothesized that by carefully selecting a surfactant and probing the bilayer formation conditions via zeta potential measurements and setting up the pyrolysis steps for carbonizing the surfactant layers and graphitizing this carbonized layer with high efficiency, it should be possible to obtain full carbon coverage.

Consequently, the aim of the thesis is

to design individual carbon coating process of an electroactive material using colloidal principles and to reveal the effects of carbon coating process parameters (primarily the amount of carbon source and pyrolysis conditions) on the particle dispersibility, crystal structure and the purity of LFP, the carbon coating characteristics (the degree of graphitization, amount, etc.), electrochemical behavior of particles and the tap density. As a result, it is aimed to design a carbon coating procedure enabling to produce individual particles and that can be generalized to other electroactive particles.

CHAPTER 3

MATERIALS AND METHODS

3.1 Materials

All materials were used as received, without any further purification. Ethylene glycol (EG, mono-ethylene glycol, $\geq 99.5\%$) and isopropyl alcohol (IPA, 99.5 %) were purchased from Tekkim. Lithium hydroxide (LiOH, 99%), ortho-phosphoric acid (H_3PO_4 , 85%), and iron (II) sulfate heptahydrate ($\text{FeSO}_4 \cdot 7\text{H}_2\text{O}$, 99+%,) were purchased from Merck. Deionized water (DIW) with resistivity of $18.2\text{ M}\Omega$ was used. Cetyltrimethylammonium bromide (CTAB, 98%) was purchased from Alfa Aesar.

3.2 LFP Particle Synthesis

LFP powders were synthesized by polyol method in a reflux setup. The stoichiometric ratio of Li:Fe:PO₄ was adjusted as 3:1:1 respectively (based on 0.14 M iron source) in the total volume of precursor suspension of 180 ml. EG was preheated to 50 °C to speed up the dissolution of the reagents and kept at that temperature during preparation of reagent suspensions.

EG was separated into two bottles, as 140 ml, and 40 ml. 0.08 mol LiOH and 0.08 mol of DIW was added into one bottle of EG (140 ml) and stirred for 30 minutes. Meanwhile, $\text{FeSO}_4 \cdot 7\text{H}_2\text{O}$ was added into the other EG bottle (40 ml) and stirred for 15 minutes, then 0.027 mol of H_3PO_4 was added and the mixture stirred for another 15 minutes. At the end of the 30 minutes, LiOH containing batch was added into this mixture containing Fe and PO₄ precursors. Black, viscous mixture was obtained.

After being stirred for another 15 minutes for homogenization, the mixture was transferred to the three-neck round bottom flask, heated up to 160 °C in a heating mantle, magnetically stirred and refluxed for 6 hours. The reaction temperature was controlled using the thermocouple connected to the heating mantle and double-checked with the thermometer placed into the reaction medium. At the end of the reaction, the suspension was cooled up to 25 °C in an ice filled ultrasonic bath (Sonamak Ultrasonic Cleaner). In order to wash out the particles from the mother liquor, the suspension was, first, centrifuged at 12,500 rpm for 15 minutes. Then, it was washed once with DIW, then once with IPA with centrifugation at 12,500 rpm for 15 minutes. After each centrifugation step, the supernatant removed, the sediment was mixed with solvent. To effectively wash the particles, the obtained suspension, first, magnetically stirred for 15 minutes, then mixed with ultrasonic horn (Bandelin, Sonopuls HD 2070, at 75 % power) for 5 minutes, and magnetically stirred again for another 15 minutes. At the end of the washing procedure, the sediment was collected and dried at 90 °C for 1.5 hours.

3.3 Coating of LFP Particles with CTAB

3.3.1 Preparation of Dilute Suspensions of LFP and CTAB

Dilute suspensions of LFP and CTAB were prepared to understand the mechanism of CTAB adsorption onto the LFP surface. For this purpose, aqueous suspensions with 0.01 wt.% of LFP and determined amount of CTAB were prepared. The CTAB concentration ([CTAB]) ranged between 0 and 1 mM. To adjust the CTAB concentration, first 0.1 wt. % of LFP powders were dispersed in DIW and homogenized with the ultrasonic horn for 5 minutes (75 % power). Simultaneously, a 9 ml of aqueous CTAB (CTAB(aq)) solution was taken from a stock solution and held in the ultrasonic bath for 5 minutes . Then, 1 ml of LFP suspension was introduced into 9 ml of CTAB(aq) and resulting 10 ml of suspension was kept in the ultrasonic bath for 5 minutes for homogenization.

3.3.2 Preparation of Concentrated Suspensions of LFP and CTAB

To increase the amount of the LFP powder coated with CTAB that can be prepared in one batch, more concentrated suspensions were needed to be prepared. In order to increase the amount of LFP by 10 times (0.1 wt. %) the CTAB to LFP ratio was kept constant. Unlike the dilute system's mixing sequence, in the concentrated system, 9 ml of CTAB_(aq) were added into the 1 ml LFP suspension. Then, the prepared 10 ml suspension was mixed magnetically for 5 minutes instead of an ultrasonic bath used in the dilute system in order to increase the probability of meeting of LFP and CTA⁺ molecules. In the end, 0.1 wt.% of LFP with [CTAB] between 0 -10 mM suspensions were prepared.

3.4 Preparation of CTAB-Coated LFP Powders

The suspensions prepared according to the procedure described above were centrifuged (Hermle, Z 36K, with 50 ml tubes) at 10,000 rpm for 20 min. After the supernatant was carefully separated from the sediment, the sediment was dried at 120 °C for 2 hours and the dried powders were used in further analyses.

3.5 Pyrolysis of the LFP Particles with/without CTAB Coating

The dried powders were heated in a tubular atmosphere-controlled furnace (Protherm, PTF 14/50/250) under Argon atmosphere (pure Ar, 99.995 %, Linde). Before heating the samples, the furnace was purged with Ar gas flowing with a rate of 25 l·min⁻¹ for 20 minutes, then the flow rate of the gas was decreased to 15 l·min⁻¹ during heating. A gradual heating procedure were performed as follows: the samples were heated from room temperature to 300 °C with rate of 2 °C/min, kept at that temperature for 1 hour, then the temperature increased up to the determined temperature (500, 600 and 700 °C) with a rate of 10 °C/min and held at that temperature for 3 hours (Figure 3.1). The samples were naturally cooled down to 100

°C under Ar atmosphere and taken out of the furnace. The heating profile is shown in Figure 3.1.

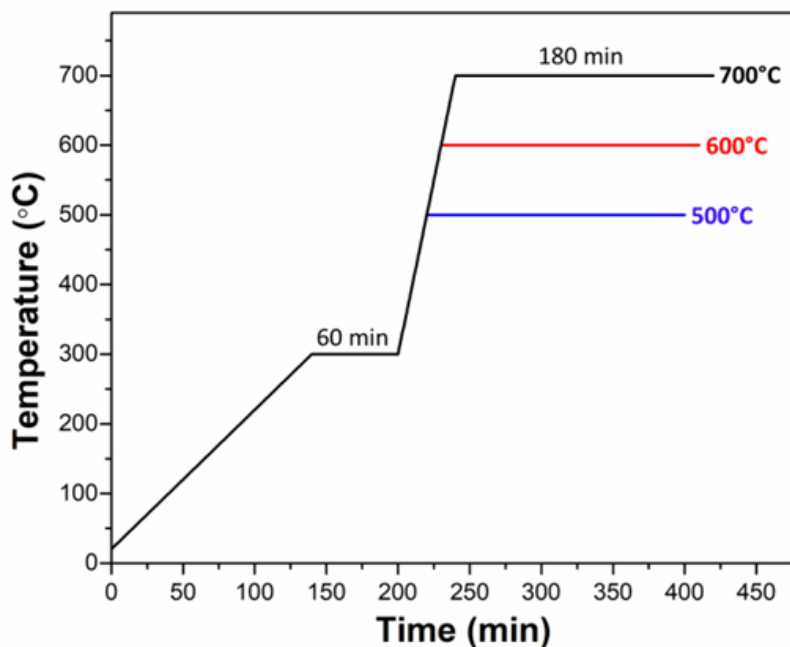


Figure 3.1. The gradual heating procedure used in the pyrolysis experiments

3.6 Characterizations

Crystal structure of the powders were analyzed by X-Ray Diffraction (XRD, Rigaku Ultima-IV) with Cu-K α radiation (0.154 nm), operating at 40 kV and 30 mV between 10° and 70° at a scanning speed of 2° min⁻¹.

To find the optimum CTAB concentration for carbon coating of individual LFP particles, the changes in the zeta potential of particles and the conductivity of the suspension were measured using Malvern, Zetasizer Ultra. The concentration of the samples was 0.01 wt. % for the dilute samples, and 0.1 wt.% for the concentrated ones. The measurements were conducted right after the sample preparation and at 25 °C. Three separate samples were prepared from the same batch, and the zeta potential

measurements of each sample were repeated three times to determine the reproducibility of results. Then, the pH of the suspensions was measured at room temperature. The pH values were recorded after keeping the pH probe in the suspension for 10 minutes due to fluctuations in the pH values.

Particle size analyses were conducted by dynamic light scattering (DLS) using Malvern, Zetasizer Ultra Instrument. The particle size of three different samples were measured and the sample preparation procedure for each type of sample was as following: (i) The pure LFP suspensions; desired concentration of LFP amount was first dispersed in water. For dispersion, first ultrasonic horn operating at 75 % power for 5 minutes was used. Then, the sample was kept in an ultrasonic bath for 5 minutes and the measurement was conducted. (ii) CTAB_(aq) solutions; CTAB was dissolved at interested concentration and after it dissolved it was kept in the ultrasonic bath for 5 minutes. (iii) Samples of CTAB and LFP suspensions were prepared according to the same procedure used in zeta potential measurements. After the suspensions left at rest for a day, the samples were taken from the turbid part that formed on the top of sediment layer. For each case described above, three different samples were taken from each batch and three different measurements were conducted from each sample. All analyses were conducted at 25 °C.

Sedimentation profile of the suspensions, as prepared in the zeta potential measurement, was determined using ImageJ software. The relative height of the suspensions was taken from the top of the suspensions up to clear point of the supernatants (Figure A.2).

Scanning electron spectroscopy (SEM, Nova, NanoSEM 430) was used to analyze morphology of the samples. For sample preparation, particles were dispersed in DIW (0.25 wt. %) and homogenized using the ultrasonic horn for 2 minutes. A drop of suspension was dropped on a silicon wafer and left to dry for 6 hours naturally. Then, a thin layer of gold deposited using Emitech SC7620 Sputter Coater operating at 1.5 V, 10 mA for 2 minutes (and the SEM analysis was carried out at 20 kV).

The Fourier transform infrared spectra were recorded in a wavenumber range between 4000 – 400 cm^{-1} using Frontier IR (Perkin Elmer) with ATR (attenuated total reflectance) attachment. The dried powders were used for analysis. (Section 3.4)

Thermogravimetric analyses (TGA, SII TG/DTA7300, Hitachi Exstar) were conducted in alumina crucibles under N_2 atmosphere, using 9 mg powder. The same heating profile used in pyrolysis experiments were used for the analysis.

The high-resolution transmission electron microscope (HRTEM) analysis was performed using Jeol 2100F (with Orius SC1000 Model 832 11 Megapixel CCD camera). The HRTEM samples were prepared by dispersing particles in ethanol. For dispersion, suspensions were kept in an ultrasonic bath (Bandelin RK-210H) for 45 minutes and dropped onto a carbon film grid and dried overnight.

The Raman analyses were performed with Renishaw, inVia Raman Microscope, using He-Ne laser, 633 nm wavelength at 10% power. Curve fitting was done using Fityk-Curve and Fitting software program^[185]. Pearson7A function was used for fitting.

Surface analyses of the powders were conducted by X-ray photoelectron spectroscopy (XPS), using XPS-PHI instrument, equipped with an aluminum monochromatic anode (Al , K_{α} = 1486.6 eV). Carbon C 1s peak at 284.6 was used as a reference for the correction. Curve fitting was done using Fityk-Curve and Fitting software program. Pearson7A function was used for fitting.

Carbon (C) and Sulfur (S) amounts of the powder samples were measured by ELTRA CS 800, Carbon Sulfur Analyzer.

Tap density was measured in a falcon tube with volume of 0.1 cm^3 . Powders were added gradually, and after each addition the tube was slowly hit to a laboratory bench (100 times). This was repeated until the entire volume was filled. For each sample the experiment repeated three times.

3.7 Electrode Preparation and Electrochemical Tests

Electroactive materials were mixed with carbon black (CB) and polyvinylidene difluoride (PVDF) (PVDF in N-methyl-2-pyrrolidone (NMP) (PVDF/NMP of 5:95 by weight)) in 80:10:10 weight fraction, LFP: CB: PVDF, respectively. The mixture was homogenized using a mixer mill (Retsch MM400) at frequency of 20 s^{-1} for 15 minutes. This cathode slurry was coated onto aluminum foil with a 200 μm electrode thickness using doctor blade and dried on a hot plate in a fume hood at $120\text{ }^{\circ}\text{C}$ for 2 hours. The foil was cut into discs ($\Phi=18\text{ mm}$) and were dried in a vacuum oven for 12 hours and directly transferred into Argon-filled glovebox. (Unilab mBraun, $\text{H}_2\text{O} < 0.1\text{ ppm}$; $\text{O}_2 < 0.1\text{ ppm}$).

All the electrochemical measurements were conducted using Bio-Logic instrument potentiostat/ galvanostat (Bio-Logic, VMP-300) at $25\text{ }^{\circ}\text{C}$. Half cells were fabricated in an Argon filled glovebox. LiPF_6 (1 M) dissolved in a mixture of ethylene carbonate (EC) and dimethyl carbonate (DMC) in 1:1 vol% was used as electrolyte. Whatman glass microfiber (GMF) was used as a separator. Li foil was used as reference and counter electrode. After assembled in the glove box, the cell was kept at room temperature for 2 hours to allow it to equilibrate. The cells were charged and discharged galvanostatically under different specific currents with a potential range of 2.5 - 4.2 V, at room temperature and cycled at different C rates (1 C= $170\text{ mAh}\cdot\text{g}^{-1}$). The electrochemical impedance spectroscopy measurements (EIS) were carried out between 20 kHz and 10 mHz, with AC amplitude of 5 mV.

CHAPTER 4

RESULTS & DISCUSSION

In order to obtain individual carbon coated LFP particles, first, dispersible LFP particles were synthesized and characterized. Then, the LFP particles were coated with a carbon source, CTAB, by controlling the interparticle interactions. For this reason, the changes in colloidal behavior of LFP particles with increasing CTAB concentration were thoroughly analyzed. In order to carbonize the CTAB on the LFP surface, the effects of pyrolysis conditions on the LFP characteristics were investigated. The individually carbon coated LFP particles under these optimized conditions were characterized. Lastly, the improvement in the tap density and the suspension rheology achieved using individual particles were demonstrated.

4.1 Properties of As-synthesized LFP particles

In this study, it is critical to use individual, dispersible bare LFP particles as a starting material for coating, so that the particle characteristics can be preserved during the carbon coating process and individual, dispersible carbon coated LFP particles can be obtained. For this reason, first, LFP particles were synthesized in EG using reflux, i.e., polyol route. The synthesized particles were characterized in terms of their crystal structure, morphology, sedimentation behavior and the surface zeta potential, and the results are presented in Figure 4.1. The XRD diffractogram in Figure 4.1a showed that the synthesized particles were crystalline and indexed to the orthorhombic olivine structure (space group Pnma, JCPDS Card No: 83-2092). The SEM micrographs in Figure 4.1-c and 4.1-d, the particles are in fusiform shape and mostly individual without any significant formation of chemical joints. As-synthesized particles are sub-micron sized ($\leq 1 \mu\text{m}$) and their zeta potential was

recorded as -50 ± 2 mV in DIW. As known from literature, $|\zeta\text{-pot.}|$ greater than 30mV generally allows to obtain electrostatically stable suspensions^[186]. As observed in Figure 4.1-b, the aqueous suspensions prepared with synthesized LFP particles did not completely sediment. The height of the suspension decreased by $\sim 1/3$, even after 6 hours, supporting that the particles are individually present and dispersed in an aqueous environment.

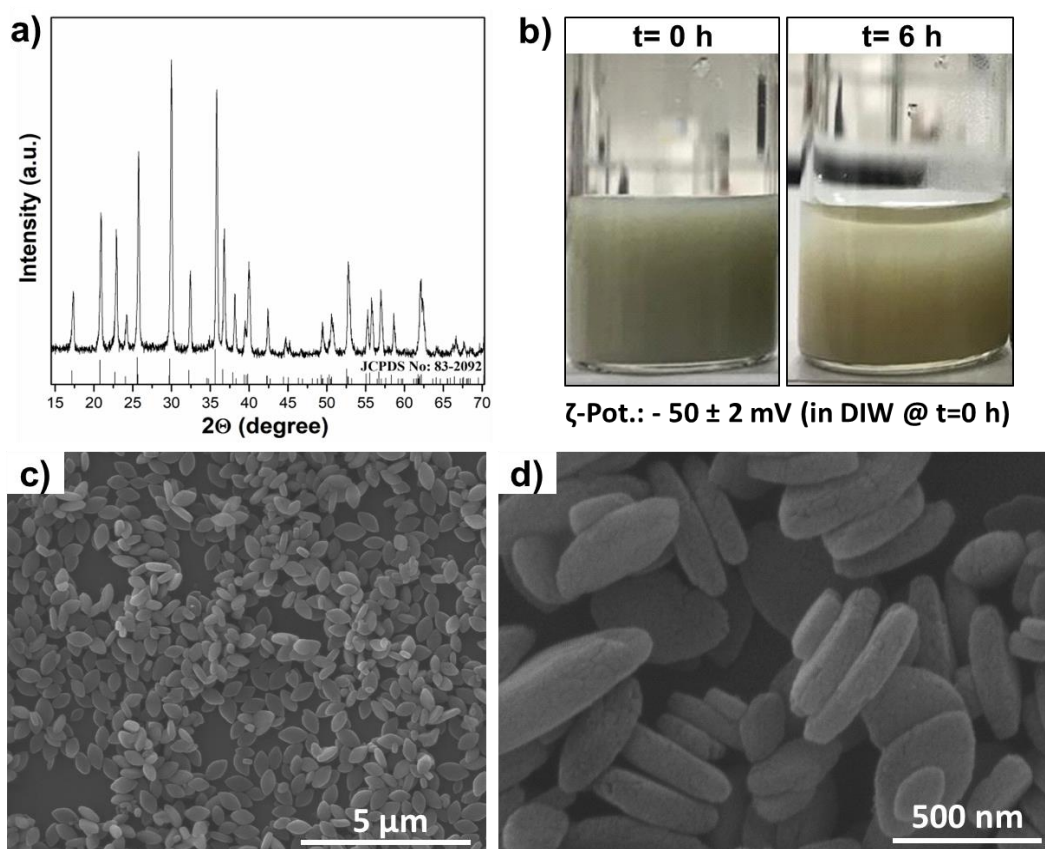


Figure 4.1. Characterization of the as-synthesized LFP particles: a) XRD pattern, b) Sedimentation test within 6 hours and zeta potential measurements, c) and d) SEM micrographs

4.2 Investigation of the Interactions with CTAB and LFP

After synthesis of individual LFP particles, the interactions between the carbon source and the LFP particles were investigated. Since the LFP particles were found to be negatively charged, a cationic surfactant, CTAB, was selected as a carbon source to enable specific adsorption of positively charged CTAB ions on LFP surfaces via electrostatic interactions. In order to reveal the extent of interactions between the LFP particles and CTAB, the changes in the zeta potential and colloidal stability of LFP particles occurred with increasing concentration of CTAB in solution were analyzed.

Figure 4.2-a (and Figure A.1-a and b) shows the change in zeta potential of LFP particles and the conductivity of suspensions with the addition of CTAB. In the absence of CTAB, the zeta potential of LFP particles was as high as -52 mV, while the zeta potential of the particles first sharply rose to zero with increasing amounts of CTAB, and at around 0.05 mM CTAB concentration, it reached a positive value of +10 mV, then gradually increased to +40 mV with further addition of CTAB. In line with zeta potential values, the particles were completely sedimented when the zeta potential values are between -30 mV and +30 mV, corresponding to the CTAB concentration of 0.02 mM and 0.09 mM, respectively (Figure 4.2-b and Figure A.2-a and b). The solution conductivity also showed a behavior change in this region. While the conductivity of the system increased very slowly up to 0.1 mM CTAB addition, the rate of increase in conductivity changed with further addition of CTAB to the system.

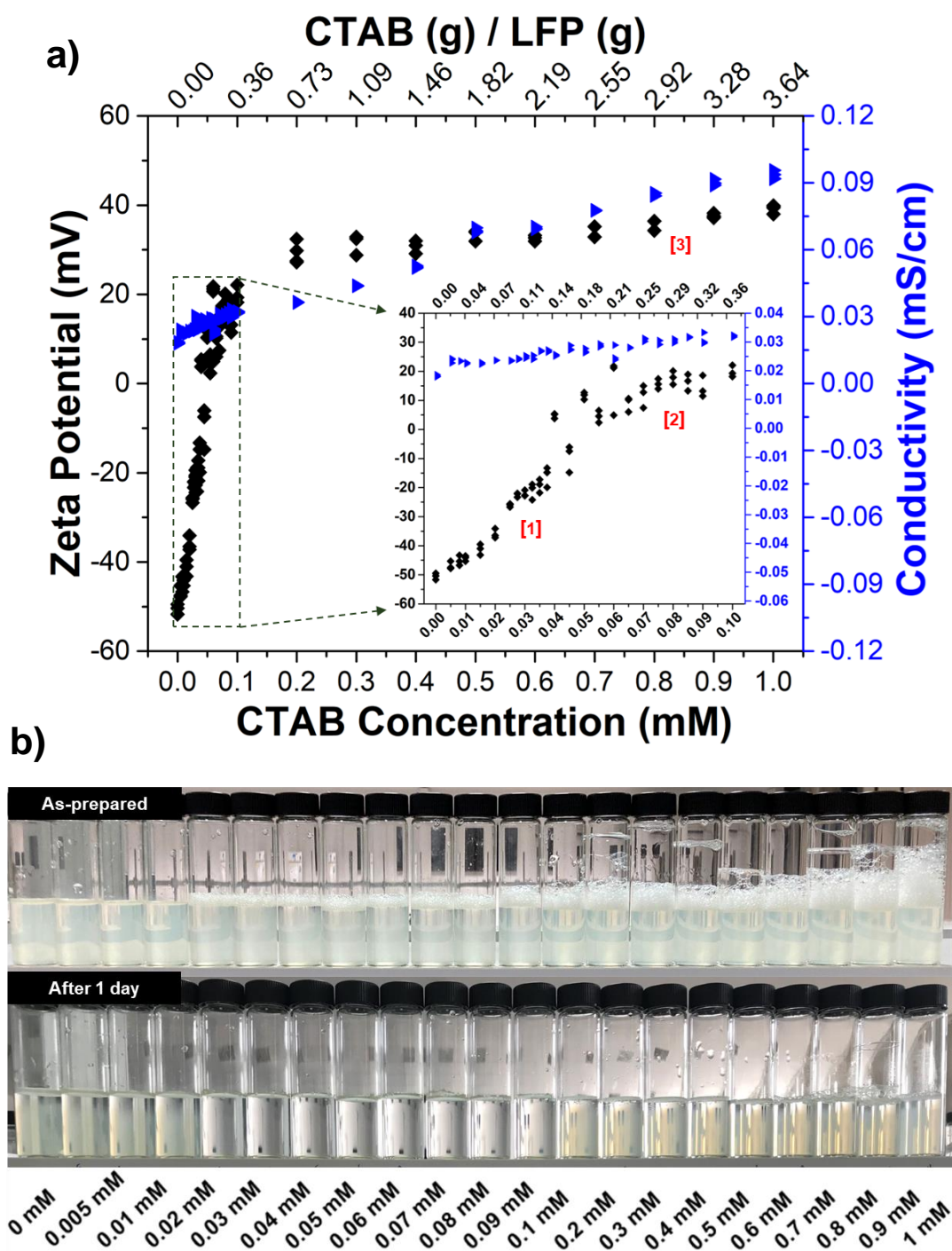


Figure 4.2. a) Zeta potential of LFP particles as a function of CTAB concentration and corresponding conductivities for dilute (0.01 wt. %) suspensions. The regions where the behavior change occurred was denoted as [1], [2] and [3],
 b) Sedimentation behavior of LFP particles with increasing CTAB concentration.

The first increase in solution conductivity with increasing CTAB concentration in Figure 4.2-a attributed to the dissolution of CTAB molecules in water. While the dissolved CTA^+ ions were expected to adsorb on negatively charged LFP surfaces, the remaining bromide (Br^-) ions are expected to be free in solution and increase its conductivity. The decreasing zeta potential of LFP particles with increasing CTAB concentration reveals the specific interactions between CTA^+ ions and the particle surfaces. Three distinct regions were detected in the concentration range of the study based on the changes in the slope of zeta potential and the solution conductivities in Figure 4.2-a: (i) 0 – 0.05 mM CTAB, (ii) 0.05 – 0.5 mM CTAB, and (iii) 0.5 – 1 mM CTAB.

In the first region (0 – 0.05 mM CTAB), the zeta potential changed from -52 mV to +10 mV and the solution conductivity increased. When the CTAB molecules were introduced to the system, it dissociates into CTA^+ and Br^- ions. The positively charged CTA^+ molecules conveniently position themselves on LFP surfaces due to electrostatic attraction as illustrated in Figure 4.3- [1] and free Br^- ions increased the solution conductivity. With adsorption of CTA^+ on LFP surfaces, the zeta potential values decreased towards zero. Similar linear change was also observed in the suspension pH, and it increased from 7.15 to 7.42 (shown in, Figure A.3.). Between CTAB concentration of 0.04 and 0.05 mM and at pH between 7.2 and 7.4 (Figure 4.4), the zeta potential was almost zero corresponding to the isoelectric point of CTAB coated LFP particles. At this concentration, the surfaces of the particles must be covered with the hydrophobic tail groups of the surfactant, so particles became unstable in aqueous solution, and started to sediment (Figure 4.2-b and Figure A.3-b). The fluctuations in the zeta potential values in this range was attributed to these instabilities. It was inferred that this region corresponds to the monolayer coverage of LFP particles with CTAB molecules (Stage [1] in Figure 4.3).

In the second region ($[\text{CTAB}] = 0.05 - 0.5 \text{ mM}$), the zeta potential continued to increase with the addition of CTAB, but with a slower rate compared to the first region. The suspension was still clear as observed in Figure 4.2-b, but its turbidity slowly increased with increasing CTAB concentration. As the CTAB concentration increased after the monolayer coverage was obtained, the tails of the additional CTA^+ molecules are expected to interact with the tails of the adsorbed CTAB molecules by turning their ionized functional groups (*i.e.*, head) toward aqueous environment (Stage [2] in Figure 4.3). This is a condition where the CTAB covered LFP particles became hydrophilic again and once this sets the stage for a potential that is repulsive enough between the particles, particles started to suspend back in solution. Redispersion of particles, therefore re-introduction of the charged units to the solution, was the potential reason of the increase in the rate of conductivity change in the second region (Figure 4.2-a). Since the additional CTAB molecules only interacted with the adsorbed CTAB molecules rather than the LFP particle surfaces, the suspension pH (Figure A.2.) did not change significantly, yet the zeta potential increased slowly to more positive values as the particles covered by positively charged CTA^+ ions, and suspensions become more turbid as the particles re-suspended with increase in their hydrophilicity. The bilayer formation was predicted to be completed at around a concentration of 0.5 mM CTAB because after this point the rate of change in the zeta potential was decreasing, that is the surface of the particles was not changing with further additions of the surfactant.

In the third region, zeta potential values did not show significant difference since probably the adsorption process reached to a saturation point, but solution conductivity kept rising as free ions were introduced to the system. After formation of bilayer coverage around LFP particles, if the CTAB concentration was further increased, additional CTAB molecules were, first, considered to move freely in suspension, then may start to form micelles if their concentration reaches to the critical micelle concentration (CMC) in the third region. A recent study of Li *et.al.*^[175] provides a supporting explanation of this phenomenon. It was stated that the cationic CTA^+ ions adsorbed on the negatively charged citrate-capped gold

nanoparticles and increasing CTAB concentration leads to formation of incomplete monolayer, complete monolayer, incomplete bilayer, and complete bilayer, consecutively. Further addition of CTAB to the suspension led to the formation of perfect bilayer along with independent micelles. It was also reported that these formations were not only dependent on the CTAB concentration, but as well as the ratio of CTAB molecules to gold nanoparticles.

Although the CMC value of CTAB was indicated around 1 mM in the literature ^[154], it was unknown in this system due to the existence of LFP. Considering the presence of LFP would increase the CMC value of the CTAB and the CTAB concentration range of the study being below this limit, micelle formation would not be expected in this system. Yet, the particle size analyses were performed based on 1 mM CTAB concentration to detect the micelle formation in LFP-free suspensions as well. As shown in Figure 4.3, the average size of CTAB (1 mM) in water was approximately 4.67 ± 1.14 nm and the average size of LFP (0.01 wt.%) particles in water was 267 nm. When the LFP particles (0.01 wt. %) were mixed with 1 mM of CTAB, the particle size measurement showed only one peak with average size of 230 nm. The absence of secondary peak at smaller dimensions supported the absence of micelles in suspension. The apparent decrease in the size of LFP particles with the existence of CTAB may be related to the better dispersion of LFP particles in water when coated with CTAB. The narrower size distribution of LFP particles compared to the case where only LFP particles present without any addition of CTAB supported this argument. It has been also observed that the contribution of free ions to the system caused an increase in the conductivity of the system, *i.e.* increased the ionic strength of the solution. In line with these results, the rise in the ionic strength which may also cause thinner electrical double layer^[187] around the particle surfaces and might have reduced the hydrodynamic radius of the system.

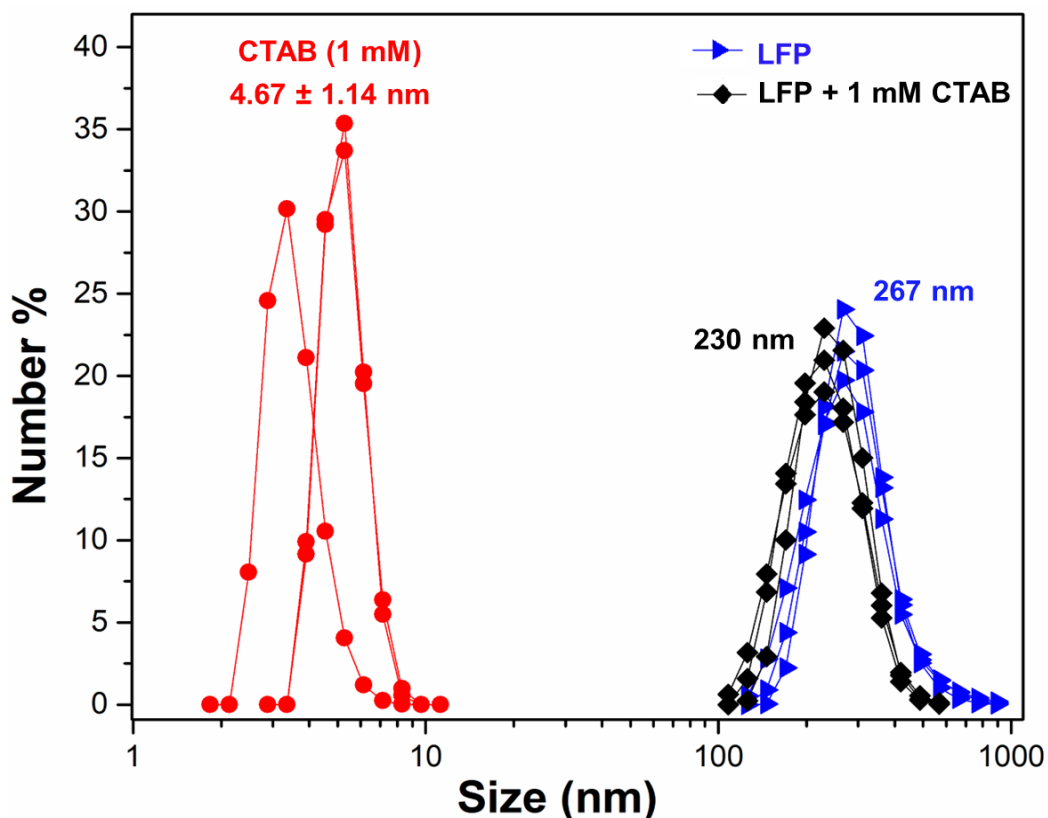


Figure 4.3. Particle size distribution of 1 mM CTAB in water, LFP (0.01 wt.%) in water, and particles suspended in the turbid part of the [LFP (0.01 wt. %) + CTAB (1 mM)] suspension after a day of sedimentation in water

When all these results were combined, the proposed mechanism was illustrated in Figure 4.4. The perfect bilayer of CTAB around LFP particles was estimated to be formed when the CTAB concentration was 0.5 mM corresponding to 1.82 g CTAB/g LFP ([2] in Figure 4.4) and further increase in CTAB concentration led to presence of free CTAB molecules in solution ([3] in Figure 4.4).

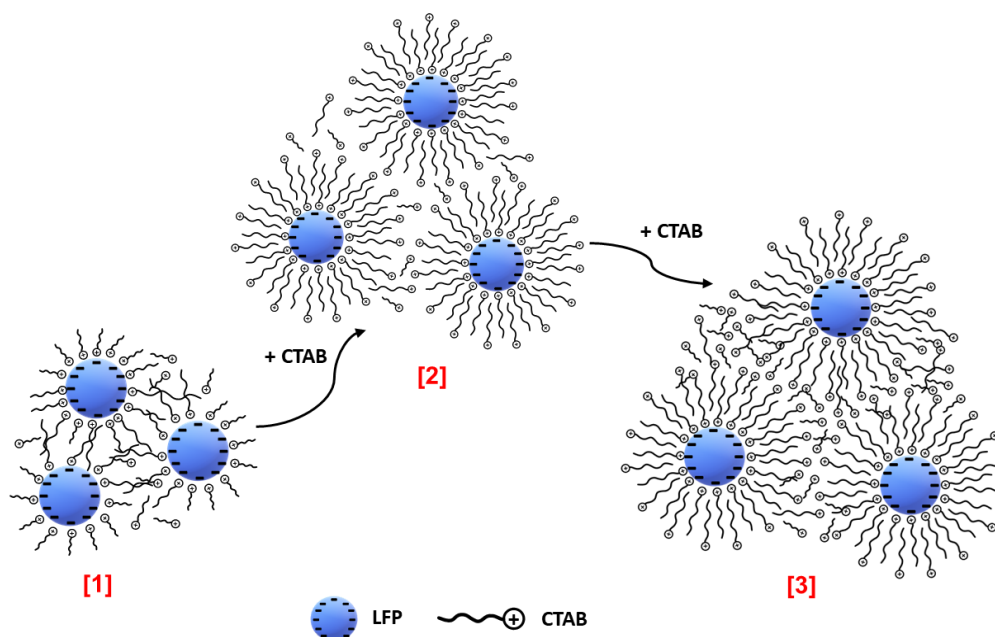


Figure 4.4. Schematics of the corresponding zeta potential stages denoted by [1] monolayer, [2] bilayer, [3] bilayer + excess free CTAB

Even though the dilute system (0.01 wt.% LFP in DIW) was helpful to understand the CTAB adsorption mechanism onto LFP particles, the concentration of the particles was too low to employ carbon coating process in useful scales. Therefore, the LFP concentration was increased 10 times (0.1 wt.% LFP in DIW) keeping the ratios between CTAB and LFP constant for each CTAB concentration (Figure 4.5, secondary x-axis on top). In order to investigate the critical concentrations, the similar analyses were employed at higher LFP concentrations.

According to the Figure 4.5, three distinct regions were detected in the concentrated suspensions based on the rate of changes in zeta potential values and solution conductivities as in the dilute case: (i) 0 – 0.1 mM CTAB, (ii) 0.1 – 5 mM CTAB, and (iii) 5 – 10 mM CTAB.

The zeta potential of the LFP particles were -60 mV at 0.1 wt.% concentration in water. With the addition of CTAB, the zeta potential moved towards positive values and the conductivity of the system kept rising as well (Figure A.1.). In the first stage,

the zeta potential changed from -60 mV to +20 mV as a result of adsorption of CTA⁺ molecules. The complete surface coverage of the particles by CTA⁺ molecules occurred between 0.05mM and 0.1 mM CTAB concentration, indicating the isoelectric point of LFP particles coated with CTAB is between pH 8 and 9. Also, at this concentration, hydrophobicity of the particles increased due to the tail groups of the CTA⁺ molecules led to sedimentation of the particles completely (Figure 4.5-b). In the second region (0.1 – 5 mM CTAB), particles were redispersed by formation of bilayers and the zeta potential of particles raised. Since the driving force between the particles were less than the first stage, the increase in the zeta potential were in a slower rate. The bilayer formation was estimated to be completed when the CTAB concentration was around 5 mM. In the third region (5 – 10 mM CTAB), the zeta potential of particle was slowly increased from +60 mV to +65 mV with further increase in CTAB amount. When the conductivity of the system was investigated, it was seen that the change in conductivity trends occurred around the same regions similar to the case of dilute suspensions. The only difference here is the amount of CTAB additions, which was as high as CMC of CTAB for each addition step, therefore, the formation of micelles could be favorable.

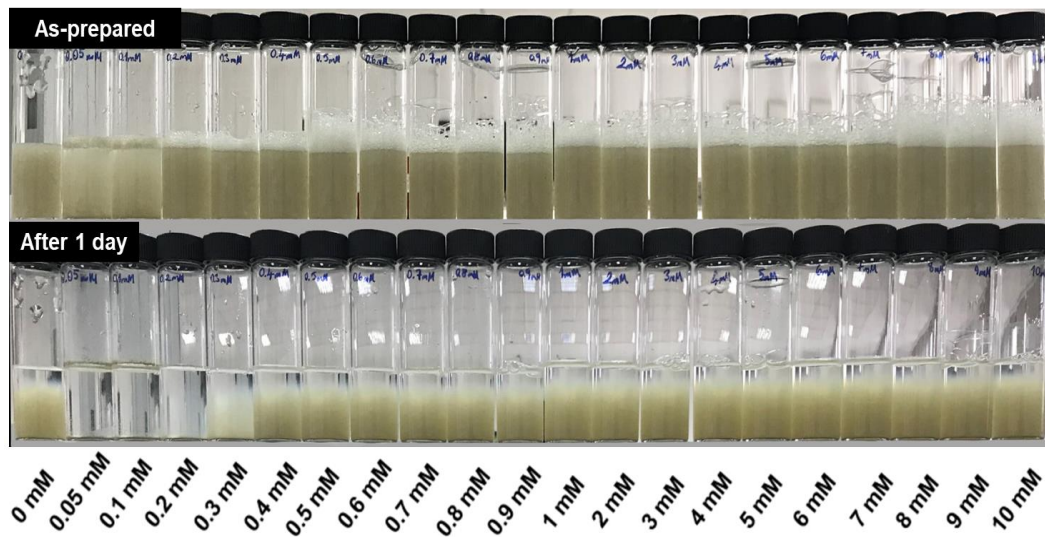
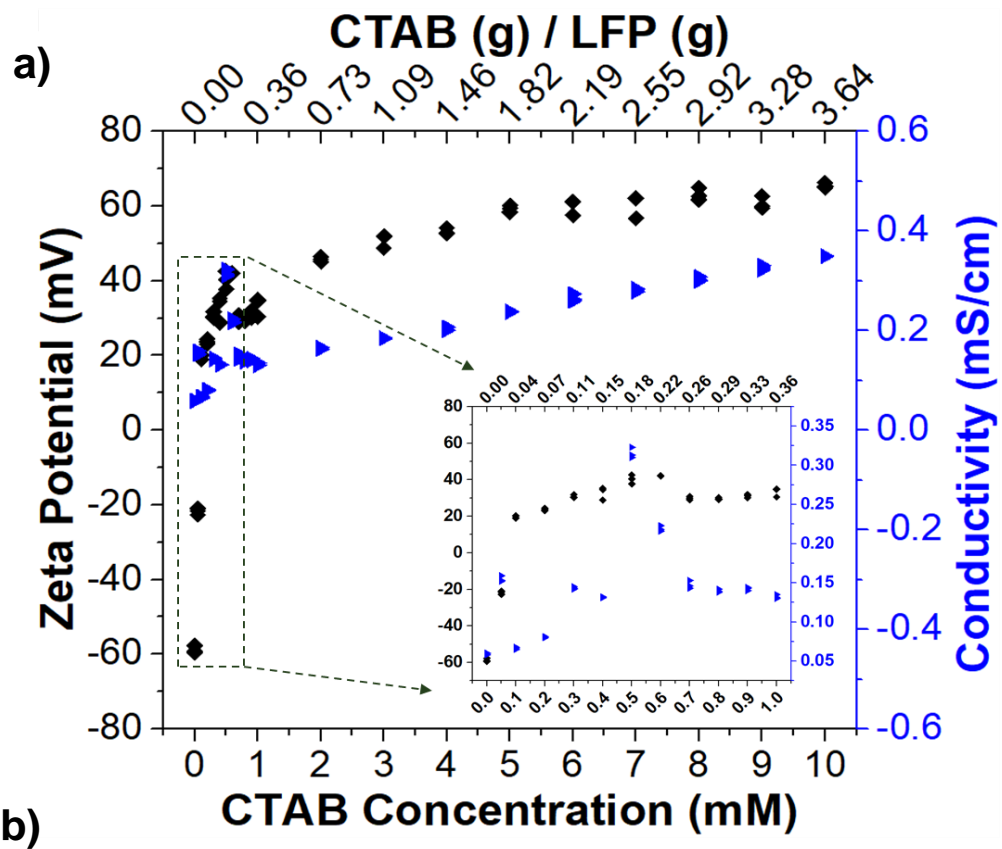


Figure 4.5. Concentrated system a) Zeta Potential and Conductivity change at different CTAB concentrations b) Sedimentation test of corresponding suspension

To check whether the micelles are formed or not at these concentrations of CTAB, particle size analyses were performed for the case where the maximum amount of CTAB was present in the systems, i.e. $[CTAB] = 10 \text{ mM}$. The average particle size of CTAB at 10 mM concentration was between 145- 200 nm and that of LFP was around 300 nm at 0.1 wt.% concentration (Figure 4.6). When the LFP and CTAB were mixed at these concentrations, the mean size of the samples prepared from the top layer of the sediment occurred after a day were around 230 nm. Compared to the LFP sample, the LFP-CTAB mixture resulted in a more homogeneous size distribution. Considering the large size of CTABs in Figure 4.6, it was difficult to comment on the presence of the individual micelles in LFP-containing suspensions. Nevertheless, the LFP particles prepared using 10 mM CTAB were labeled as excess-CTAB where “excess” indicates the CTAB amounts more than the one required for the bilayer formation whether the excess CTAB molecules were free or formed micelles.

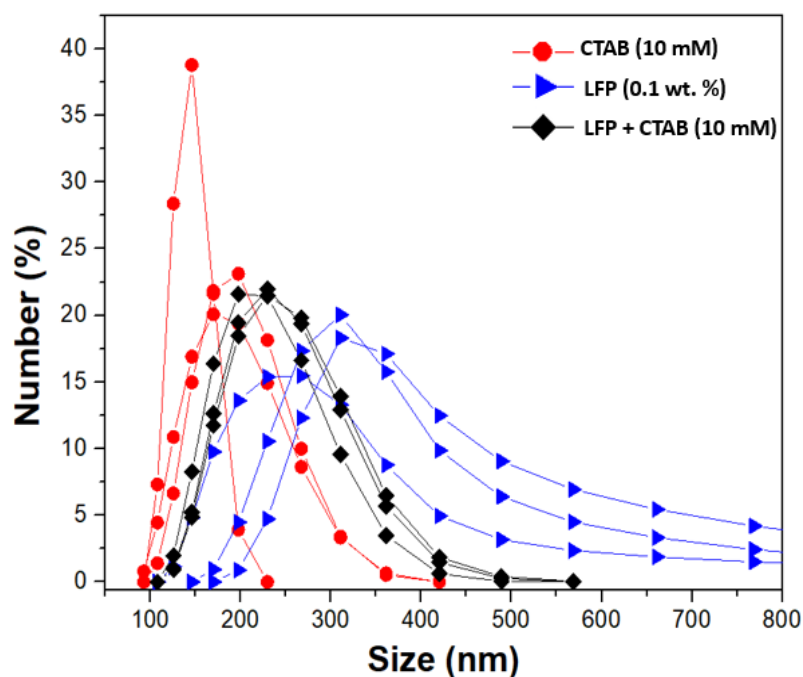


Figure 4.6. Particle size distribution of CTAB (10 mM), LFP particles (at 0.1 wt. %) and LFP (0.1 wt. %) + CTAB (10 mM) suspension in DIW, taken from the turbid part of the suspension after a day of sedimentation in water

When dilute and concentration systems were compared, even though the general behaviors were similar, the CTAB concentration at which the monolayers formed were slightly different. While the monolayer is formed at 0.05 mM [CTAB] (0.18 g CTAB/ g LFP) in dilute system, the same condition was reached at 0.1 mM [CTAB] (0.04 g CTAB/ g LFP) in the concentrated system. Although, LFP and CTAB ratio were kept constant during scale up, the required [CTAB] for the monolayer coverage in the concentrated system was less than the dilute system. The bilayers, on the other hand, were formed at the same CTAB(g) / LFP (g) ratio of ~ 1.82 , corresponding to 0.5 mM CTAB in the dilute system and 5 mM CTAB in the concentrated system.

In order to investigate the effect of LFP-CTAB structure on the carbon coating process, 5 mM and 10 mM CTAB additions to the concentrated suspensions (0.1 wt.% LFP) were selected to represent homogeneous bilayer formation and the excess CTAB conditions, respectively. The bare LFP (pristine LFP) was also used as a reference and further analyses were conducted using these three samples. The samples were labeled as LFP, LFP-B, and LFP-E for the bare LFP, the LFP coated with bilayer CTAB (5 mM CTAB), and the LFP coated with bilayer CTAB, but consisting of excess CTAB (10 mM CTAB), respectively.

The samples to be used in the carbon coating were prepared, centrifuged, and dried as described in Section 3.4, then these dry powders were used in pyrolysis experiments.

To confirm the presence of CTAB molecules on LFP particles, the dried powders were characterized by FTIR Spectroscopy (Figure 4.7). Characteristic peaks of the LFP were between 1500 and 400 cm^{-1} (fingerprint region)^[188]. The CTAB coating around LFP particles was very thin, so the transmittance peaks were not all obvious. However, the most dominant transmittance peaks of CTAB were expected between 3000-2750 cm^{-1} corresponding to C-H stretching peaks. These peaks were only present in the CTAB treated samples, but absent in the bare-LFP, proving the presence of CTABs on LFP particles when treated. On the other hand, existence of -OH and C-H/C-C stretching (between 1250-1750 cm^{-1}) in all samples drew attention

and were attributed to the organic (mainly EG^[189]) residues from the reaction medium and partially remained on particles even after washing.

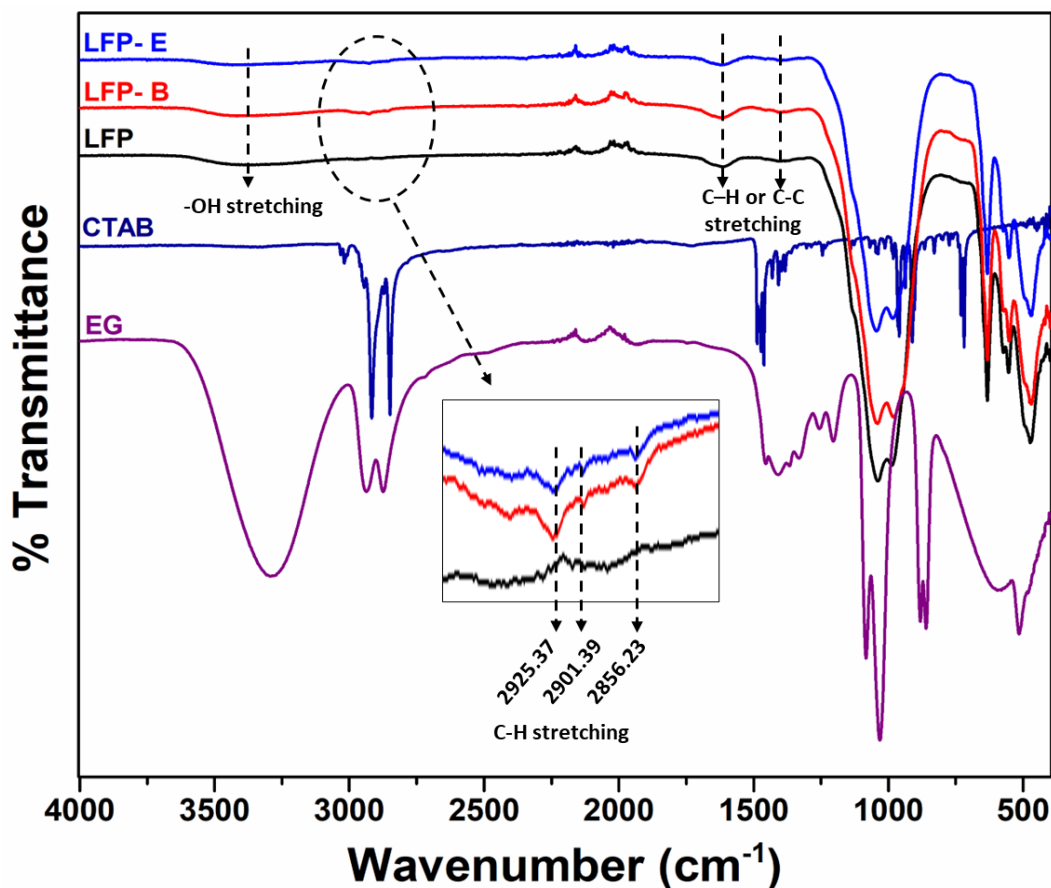


Figure 4.7. ATR - FTIR spectra of the samples: EG, CTAB, LFP, LFP-B and LFP-E

4.3 Pyrolysis of the CTAB-Coated LFP Particles

In order to pyrolyze the organic content into carbon, heat treatment was employed. First, the effects of heat treatment parameters on the CTAB-coated LFP particles were revealed using thermogravimetric analysis (TGA). Based on the results, pyrolysis parameters were determined, and the heat treatment procedure were employed at larger scale in a tube oven.

As shown in Figure 4.8, when the CTAB heated alone in a TGA oven under inert N₂ atmosphere to 500 °C, it completely decomposed to gas molecules regardless from the heating rate employed (2 °C/min or 10 °C/min) and no solid carbon residues left. While the decomposition occurred at around 250 °C when heating rate was 2 °C/min, it decomposed at 300 °C when the heating rate was 10 °C/min.

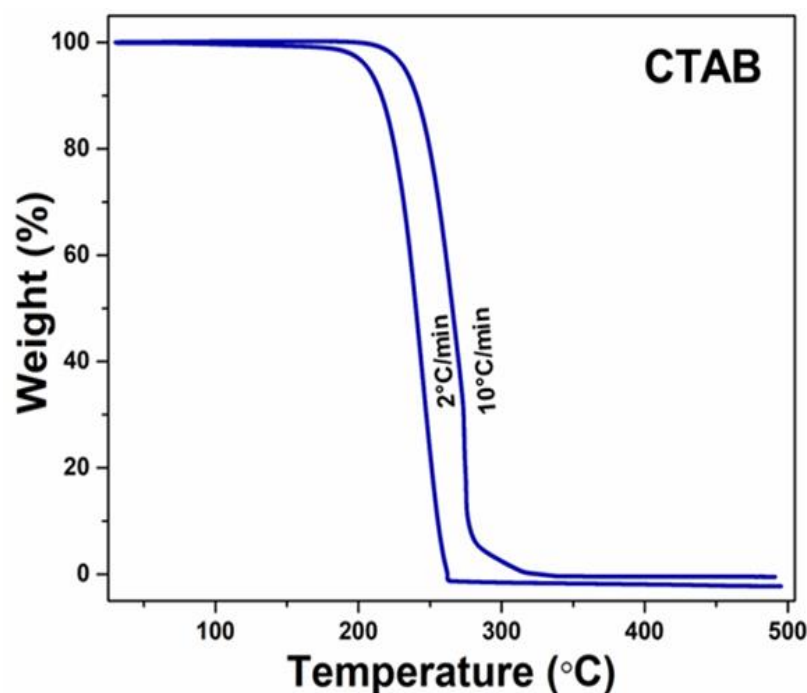


Figure 4.8. TGA of CTAB with 2 °C/min and 10 °C/min

The TGA of LFP, LFP_B and LFP_E were investigated using slow heating rate of 2 °C/min and the results were shown in Figure 4.9. There were three consecutive events in each sample, occurring with different kinetics. These events for LFP sample occurred approximately in temperature ranges of 30 – 250 °C, 250 – 450 °C, and 450 – 700 °C. The corresponding mass losses in these ranges were around 2.7 wt.%, 2.6 wt.%, and 6.3 wt.% respectively. In total ~11.6 wt.% of mass was lost up to 700 °C. For the first two events, maximum mass loss occurred at 150 °C and 200 °C, which might be equivalent to evaporation of adsorbed water^[190-192] and pyrolysis of the organic residue on the LFP surface^[193], respectively. LFP is an inorganic

material, yet it had been confirmed by FTIR analysis that the organic residues remained on its surfaces from the synthesis environment. Therefore, the mass losses occurred at temperatures higher than 150 °C was attributed to the pyrolysis of these organic residues. The mass loss occurred at temperatures higher than 450 °C was probably related to the degradation of LFP, which was also confirmed later with further analysis of the LFP powders treated under similar conditions.

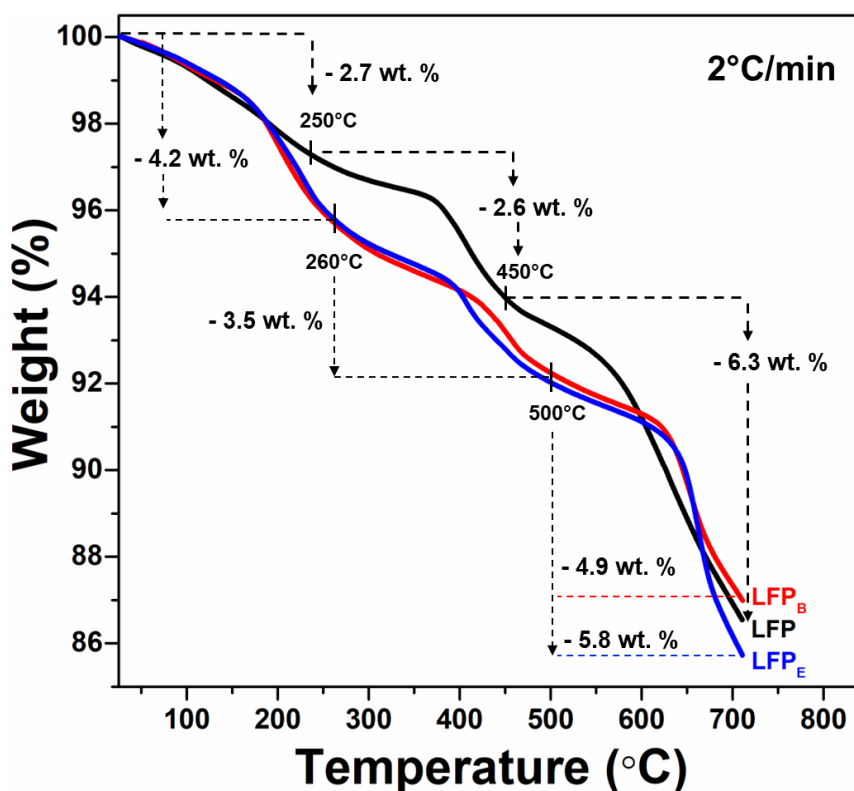


Figure 4.9. TGA of LFP, LFP_B and LFP_E samples with 2 °C/min

For CTAB treated samples (LFP_B and LFP_E), shown in Figure 4.10, three distinct events, in temperature ranges of 30 – 260 °C, 260 – 500 °C, and 500 – 700 °C, were observed as in the case of the bare-LFP particles. The presence of CTAB on the LFP (LFP_B and LFP_E), led to higher weight loss compared to the bare-LFP. While the maximum mass losses recorded during events occurring at 150 °C, 375 °C, and 600 °C in the LFP, they occurred at around 175 °C, 400 °C, and 640 °C for CTAB treated samples. The maximum mass loss happened synchronously in CTAB treated

samples, but with retarded compared to LFP. The mass losses were about 4.20 wt.%, 3.50 wt.% for the first two events, respectively, and almost same for each sample. For the third event, the values were 4.9 wt.% for LFP_B; and 5.8 wt.% for LFP_E. In total ~ 12.6 wt.% and 13.5 wt.% of mass lost in LFP_B and LFP_E, respectively.

The presence of more organic content is evident from the higher mass loss occurred during pyrolysis of CTAB-containing sample. However, it would not be realistic to calculate the amount of carbon content originated from CTAB by subtracting these values because during the CTAB coating of LFP particles, portion of the EG might exchange with CTAB. It is also interesting to realize that the CTAB could be converted to solid carbon during pyrolysis while it was known to completely decompose into carbonaceous species in gas phase in the absence of LFP particles. It can be concluded that the presence of LFP catalyzes the decomposition of CTAB during pyrolysis. It is known from the literature that catalytic carbonization of CTAB may occur due to the existence of transition metal, which is iron in LFP^{[194],[129],[195]}. Presence of transition metals or some iron compounds are known to act as catalyst in carbonization and promote the synthesis of carbon-based materials from organic carbon sources at temperatures as low as 600 °C - 700 °C. Also, ferrites are commonly used in biological processes due to the interaction between iron and carbon^[195-197].

At faster heating rate, 10 °C/min, shown in Figure 4.10., three successive events within the temperature ranges of 30 – 250 °C, 250 °C – 500 °C and 500 – 700 °C were observed similar to the case where the slower heating rate were employed. The mass losses for these three consecutive events were approximately 2.9 wt.%, 3.3 wt.%, and 5.7 wt.%, for LFP, while they were 3 wt.%, 4 wt.%, and 4.1 wt.% for LFP_B and LFP_E respectively. In total there was 11.9 wt. % mass loss in LFP and 11.1 wt.% mass loss in CTAB-treated samples. In comparison, less mass loss occurred when the heating rate increased from 2 °C/min to 10 °C/min. The maximum mass losses of the CTAB-treated samples were synchronous with each other but delayed according to LFP in the fast-heating rate.

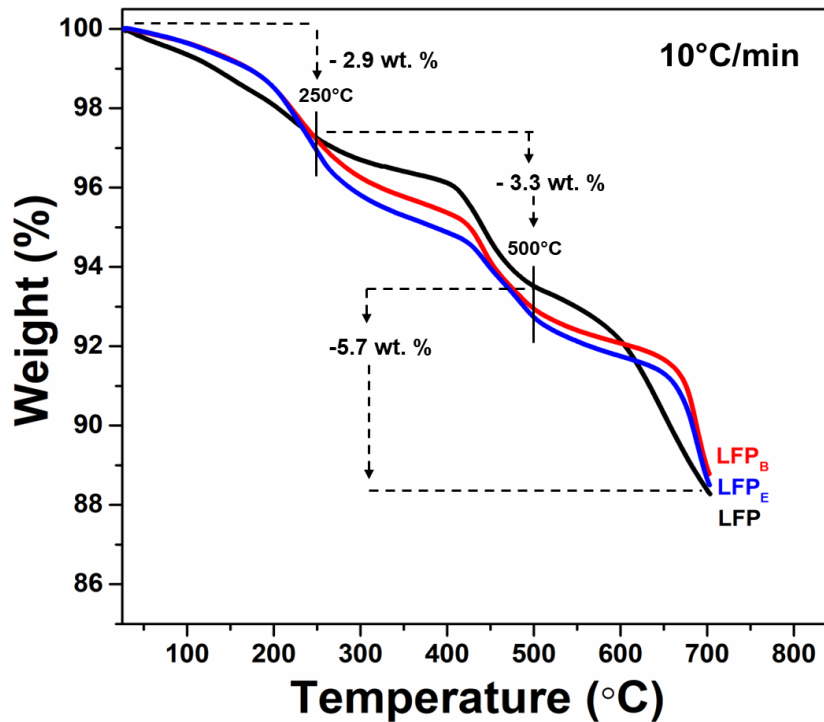
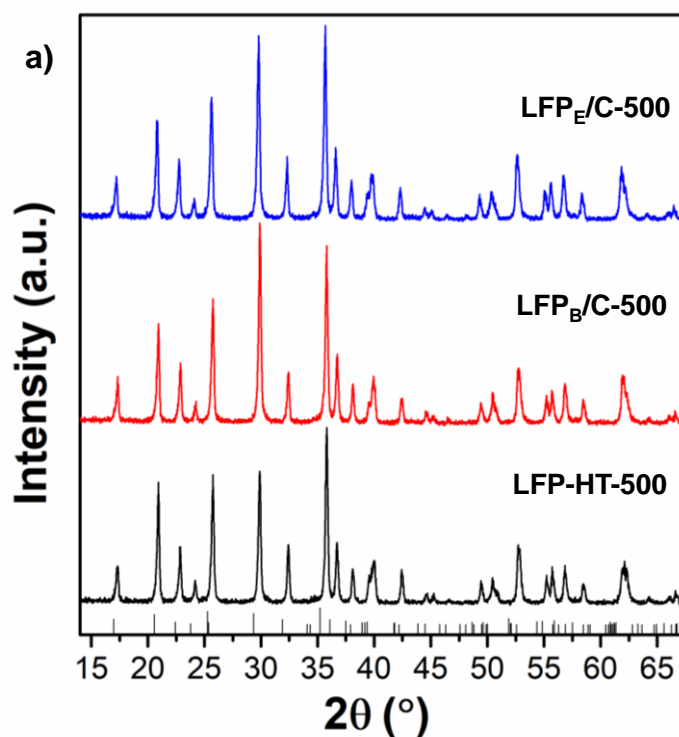


Figure 4.10. TGA of LFP, LFP_B and LFP_E samples with 10 °C/min

Based on the TGA results, the heat treatment procedure which employed in atmosphere-controlled oven was designed as following: The first event, ended around ~250 °C, regardless of the carbon content or heating rate. Because the mass loss was less when heat treatment was employed at lower heating rates, it was decided to increase the temperature first to 300 °C with slower heating rate, 2 °C/min, and the system was let to get stabilized at this temperature for an hour. The time spent at high temperatures are critical for carbon coating of LFP particles because long heat treatments at high temperatures will favor the graphitization of carbon, but it will also favor the oxidation of LFP. That is why, the second step in heat treatment procedure were decided to increase the temperature with higher heating rates, 10 °C/min, and the dwell time was fixed to three hours. Isothermal heat treatment at this stage were employed at different temperatures (500 °C, 600 °C and 700 °C), and the carbon coating characteristics and the content of LFP particles were analyzed to determine the optimum pyrolysis conditions. After the heat treatment, as-synthesized

LFP was denoted by LFP-HT and CTAB-coated samples were denoted as LFP_B/C and LFP_E/C. The temperature reached at the second stage of the heat treatment was also indicated in the label. Heating procedures employed to each sample were presented in Figure 3.1.

The purity of the powders was characterized using XRD. As shown in Figure 4.11-a, at relatively low temperature (500 °C), the powders were pure without any indication of secondary phase formation. At 600 °C, only as-synthesized LFP exhibited the secondary Li₃PO₄ phase while CTAB-containing samples did not, indicating that the presence of CTAB (or its carbonized form at these temperatures) on LFP particles inhibiting the side reactions and chemically protect the particles (Figure 4.11-b). At even higher temperature (700 °C), the secondary phase, Li₃PO₄, was present in all samples (Figure 4.12-c), indicating that even the presence of the carbonized form of CTAB was not able to protect particles from secondary reactions.



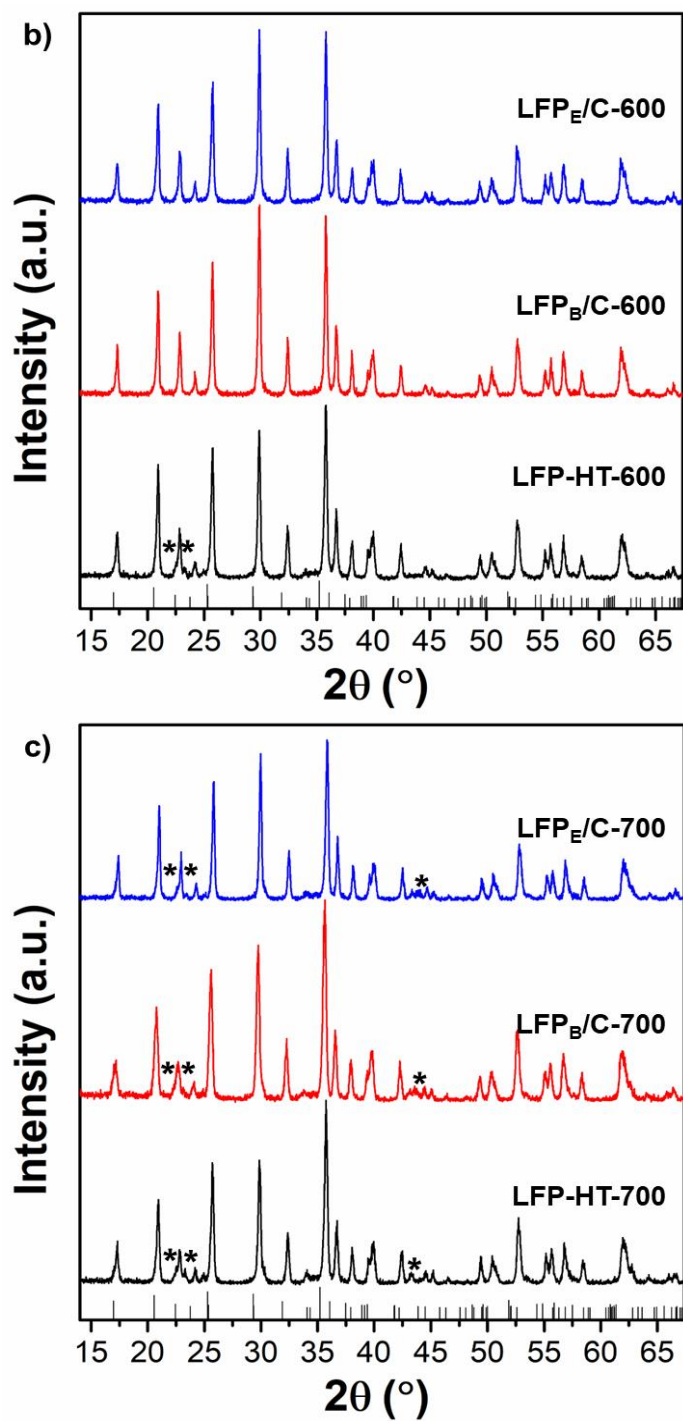


Figure 4.11. XRD patterns of samples, pyrolyzed at a) 500 °C, b) 600 °C, and c) 700 °C, indexed by LiFePO₄, JCPDS Card No: 83-2092, asterisk states the secondary phase of lithium phosphate (*: Li₃PO₄)

The detrimental effects of the presence of the secondary phases to electrochemical performance were studied in detail in the literature as discussed in the pyrolysis section of 2.2.3.1. For LFP electroactive material, the presence of Li_3PO_4 would lead to the formation of FeP and/or Fe_2P on particles surfaces^[109]. Although Li_3PO_4 were detected as a secondary phase in some samples in the XRD data, iron-based impurities were not realized.

The morphology of the particles after heat treatment were analyzed as a function of heat treatment temperature and the CTAB content. In Figure 4.12, the SEM micrographs clearly showed that increasing temperature from 500 °C to 700 °C caused morphology changes and neck formations in as-synthesized LFP particles. At 500 °C, particles preserved their shapes (Figure 4.12-a). At 600 °C, the particles seemed mostly individual, but their morphology deteriorated except from few (Figure 4.12-b). At 700 °C, on the other hand, particles completely lost their initial fusiform shapes and chemically joined to each other (Figure 4.12-.c). Considering the secondary phase formations detected in XRD analysis and the organic residues left on particles detected in FTIR, it can be concluded that morphology changes can be associated with the formation of secondary phases and/or pyrolysis of the organic residues on particles.

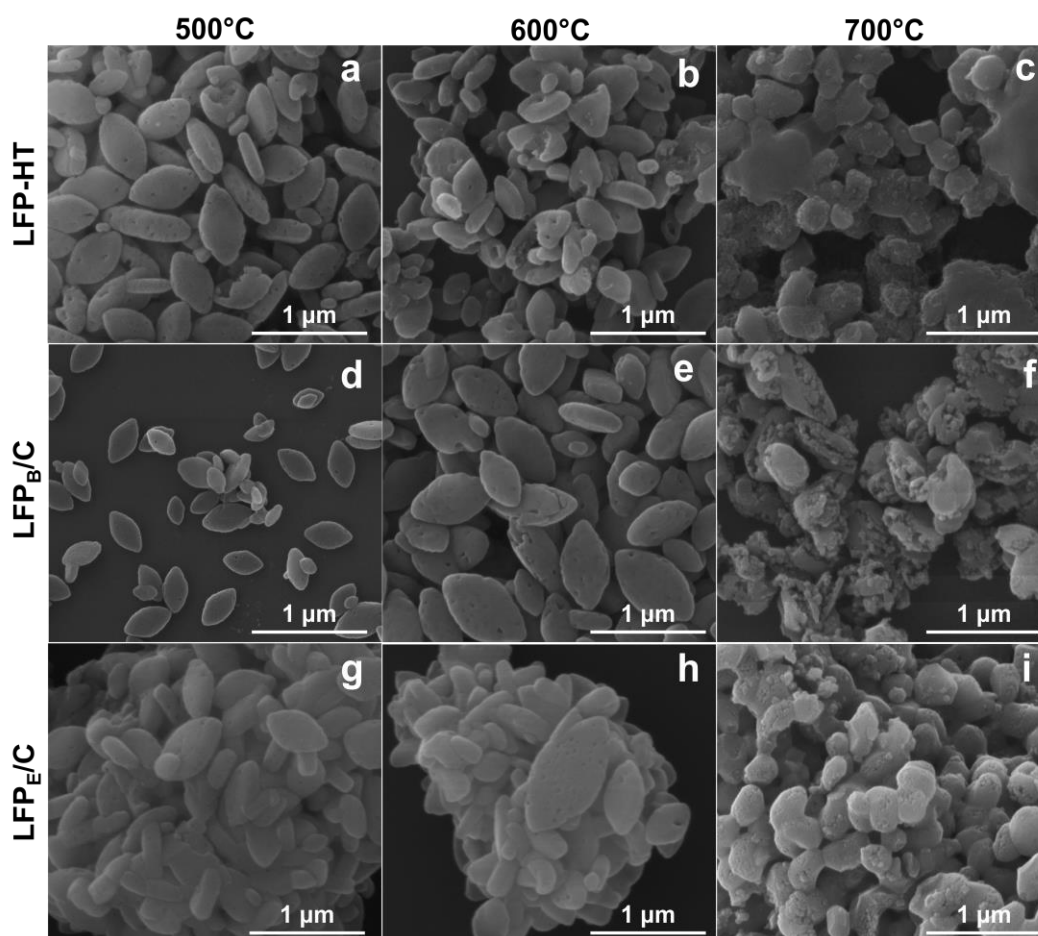


Figure 4.12. SEM micrographs of the samples at different CTAB concentration and temperature

The LFP particles coated with bilayer CTAB (LFP_B/C) was analyzed using SEM after pyrolysis. After heat treatments at 500 °C and 600 °C (Figure 4.12.d and e), the individuality and the morphology of the particles were seemed to be preserved. In line with the XRD analysis, these results supported that carbon coating formed as a result of the pyrolysis of CTAB molecules were able to chemically protect the LFP crystals. Moreover, there was no indication of neck formations between particles indicating that the particles could be coated individually. When the LFP were treated with a higher amount of CTAB (LFP_E/C), samples were aggregated and the ones staying individuals were attached onto the aggregated clusters as a result of heat

treatments at both 500 and 600 °C (Figure 4.12- g and h). At 700°C, as in other cases, samples lost their initial morphology, became severely aggregated again regardless of the carbon coating process (Figure 4.12 - c, f, and e).

In order to investigate the dispersibility of the carbon coated LFP particles, sedimentation behaviors were observed (Figure 4.13). The particles which observed to be chemically interacted with each other after heat treatment at 700 °C sedimented right after the sample preparation while all other samples stayed dispersed even after one day regardless of their carbon content. While the bare LFP had a zeta potential of -50 ± 2 mV, the zeta potential values of the samples pyrolyzed at 500 and 600 °C were measured between -42 and -46 mV and supporting the stable nature of the samples in water. After pyrolysis, samples with differing zeta potentials from the bare LFP demonstrated that the pyrolysis altered the particle surface.

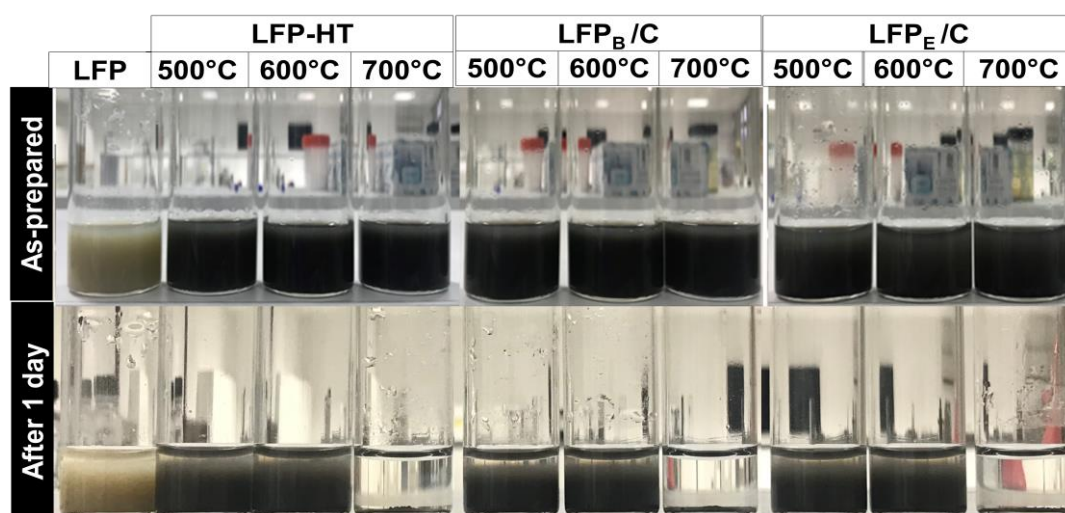


Figure 4.13. Sedimentation photos of the corresponding SEM micrographs

In order to understand the influence of carbon coating process on the electrochemical behavior of LFP particles, specific discharge capacities were measured at 0.1 C and 0.5 C current rates (Figure 4.14). Initial discharge capacity of as-synthesized LFP (LFP) started with $92 \text{ mAh}\cdot\text{g}^{-1}$ at 0.1 C and dropped to $30 \text{ mAh}\cdot\text{g}^{-1}$ at 0.5 C. When it was treated at 500 and 600 °C (LFP-HT samples), 110 and $80 \text{ mAh}\cdot\text{g}^{-1}$ were obtained respectively, indicating the improvement in discharge capacities obtained at 500 °C

even without CTAB coating. This improvement might be due to the better crystallization of LFP particles with heat treatment and/or carbonization or graphitization of the EG residue remained on LFP particle surfaces after synthesis. However, at higher temperatures, the specific discharge capacity values decreased to the levels lower than as-synthesized LFP particles. This result might be related to the presence of Li_3PO_4 phase detected in XRD analysis and/or the changes in the crystal structure observed in SEM micrographs.

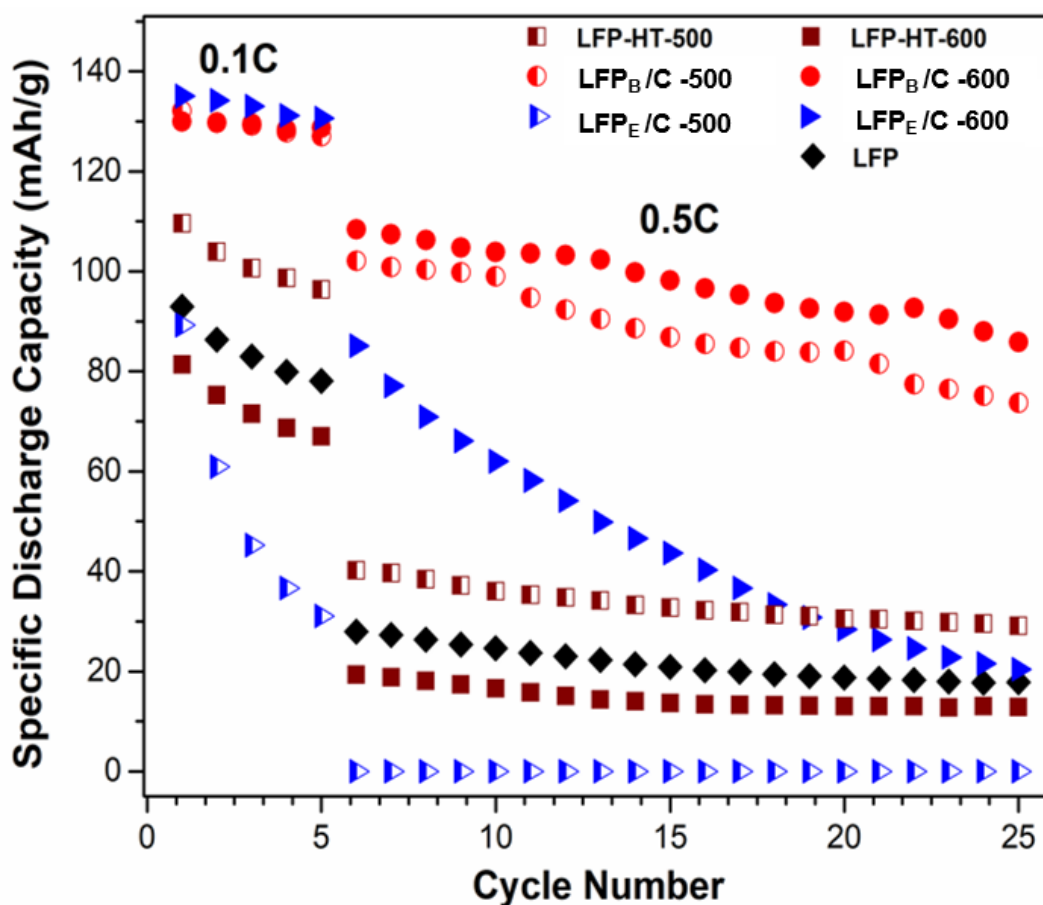


Figure 4.14. Galvanostatic charge/discharge profiles of the as-synthesized LFP and samples of 500°C and 600°C heat treatment samples

When the particles coated with CTAB bilayer (LFP_B/C) and treated at 500 and 600 °C, the initial discharge capacity were almost same and were 130 mAh·g⁻¹. The difference between two samples were observed when the discharge rate increased to 0.5 C and the sample treated at 600 °C performed slightly better than the one treated at 500 °C. Moreover, since the commercial carbon coated LFP particles had specific capacity of in the ranges of 120 -160 mAh·g⁻¹ [198], LFP_B/C, synthesized in this study exhibited appreciable electrochemical performance (130 mAh·g⁻¹).

When the LFP particles coated with excess CTAB, and the samples were treated at 500°C (labelled as LFP_E/C-500 in Figure 4.14), the specific discharge capacity values started with 95 mAh·g⁻¹ and faded quickly and became zero at 0.5 C. When the powders with same CTAB coating treated at 600 °C (labelled as LFP_E/C-600 in Figure 4.14), the best battery performance was obtained with specific discharge capacity of 130 mAh·g⁻¹ at discharge rate of 0.1 C, however, again the capacity quickly faded when the discharge rate increased to 0.5 C. In either case the samples prepared using excess CTAB could not maintain its electrochemical performance at higher discharge rates.

To better understand the influence of carbon coating of LFP particles in electrochemical performance, the conductivities of the samples were measured using Impedance Spectroscopy. In the Nyquist plot of the samples, presented in Figure 4.15, the semicircle diameter indicates the charge transfer resistance (R_{ct}) and correlated to the electrochemical reactions at the particle-particle contact and at the electrode-electrolyte interface [199-201]. The smaller the diameter of the semicircle, the lower the resistance of the system. The slope appearing at low frequency region refers to the Li⁺ ion diffusion in the bulk electrode and it is mathematically converted to the Warburg coefficient, then solid-state diffusion coefficient of Li⁺ ion can be estimated through Warburg element [202-204]. In general, higher the slope means higher the diffusion coefficient of Li⁺ ion. Accordingly, the plots in Figure 4.15-a showed that, as synthesized LFP's R_{ct} was ~260 Ω and thermal treatment increased the resistance to ~ 360 Ω. The carbon coating obtained using bilayer CTAB after heat treatment at 500 °C lowered the resistance of the system to ~230 Ω and the

coating obtained using excess CTAB and treated at 500 °C, the resistance increased back to a higher resistivity of 400 Ω. The carbon coated using bilayer concentration was expected the best Li⁺ ion diffusion kinetics. In results presented in Figure 4.15-b showed that pyrolysis of as-synthesized LFP at 600 °C (LFP-HT-600), led to decrease in the resistance more than the one observed when heat treatment was employed at 500 °C (LFP-HT-500). Similarly, the bilayer CTAB coated LFP(LFP_B/C-600) exhibited the lowest resistance whereas the presence of extra carbon (LFP_E/C-600) led to higher resistance.

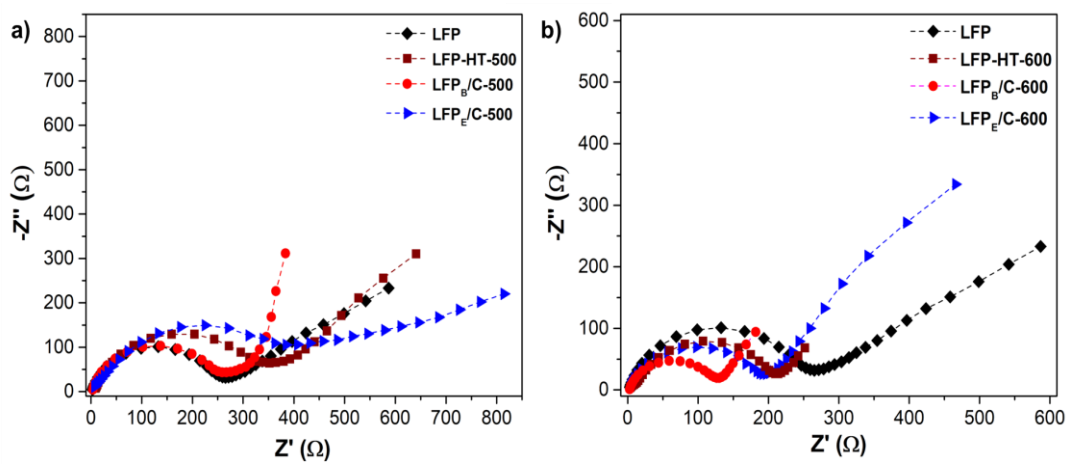


Figure 4.15. a) Electrochemical Impedance Spectroscopy of the as-synthesized LFP and samples of 500 °C and 600 °C heat treatment samples

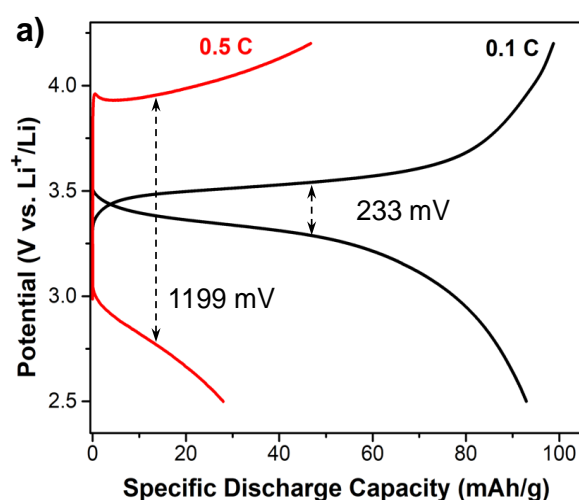
The charge and discharge voltage profiles for cells with different samples under galvanostatic cycling at a current rate of 0.1 C and 0.5 C were compared in Figure 4.16. It could be seen that the over-potential gap (difference between charge and discharge voltage at the half capacity of the first cycles^[205]) decreases with the increase of the current rate. The voltage differences between the charge and discharge curves of the samples at current rates of 0.1 C and 0.5 C were 233 and 1199 mV for LFP (Figure 4.16-a); 236 and 1077 mV for the LFP sample after heat treatment at 500 °C, respectively (Figure 4.16-b). When the LFP sample was carbon coated using bilayer CTAB concentration at 500 °C, the potential differences

decreased to 135 (0.1 C) and 660 mV (0.5 C) (Figure 4.16-d). However, when the LFP sample was carbon coated using excess CTAB concentration at 500 °C, the potential difference increased to 803 mV at 0.1 C, this difference increased significantly at 0.5 C, and the cell became dead (Fig. 4.16-f). As seen on the graphs (Figure 4.16-a, b, d, f), the voltage difference greatly increased while going from 0.1 C to 0.5 C, after heat treatment and the carbon coating at 500 °C, the potential gap between 0.1 C and 0.5 C decreased remarkably except using excess amount of carbon concentration (Figure 4.16-f).

The potential gap of LFP sample after heat treatment at 600 °C decreased and showed 351 and 1204 mV at 0.1 C and 0.5 C current rates (Figure 4.16- c), respectively. Carbon coating of the samples using pre-assumed bilayer concentration further decreased these differences such as 90.5 and 473 mV (Figure 4.16- e), while the carbon coating using excess carbon concentration increased this potential gap to 129 and 942 mV at 0.1 and 0.5 C current rates respectively (Figure 4.16- g).

The flat voltage plateaus between 3.3 and 3.6 V imply the two-phase $\text{LiFePO}_4 \leftrightarrow \text{FePO}_4 + \text{Li}^+ + \text{e}^-$ reaction^[206]. The slight voltage differences indicate the good electronic conductivity of the LFP/C composite. The increase in voltage difference implies that the resistance of the electrode increases, and the lithium diffusion becomes sluggish and electrochemical performance is deteriorated^[207]. In other words, lower over potential reflects lower internal resistance and better ion transfer capability of the electroactive material ^[173, 208]. Thus, it can be deduced that the reaction kinetics and electrical conductivity of LFP (Figure 4.16-a) were improved after heat treatment at 500 °C (Figure 4.17-b) and carbon coating at bilayer CTAB concentration (Figure 4.16-d) at 500 °C. Yet, the reaction deteriorated, and capacity faded out rapidly when LFP was carbon coated excessively at 500 °C (Figure 4.16-f). Similarly, the heat treatment and carbon coating at 600 °C led to the same response to the heat treatment and CTAB concentration. Heat treatment at 600 °C (Figure 4.16-c) enhanced the electrochemical reaction and lower over-potential than LFP (Figure 4.16-a) was observed. The carbon coating at bilayer concentration

(Figure 4.16-e) further improved the kinetics specific capacity got higher and low potential was obtained. Carbon coating at 600 °C, using excess CTAB concentration made the reaction slower and the conductivity of the carbon layer lower (Figure 4.16-g); thus, higher polarization occurred in the cell, and a higher potential gap than the bilayer concentration was noticed at this concentration. Generally, the reaction kinetics at 600 °C was further improved than at 500 °C and even lower potential gap was observed. It was noticed that the carbon coated LFP sample using bilayer concentration (Figure 4.16-e) had the best electrochemical reaction kinetics and the lowest electrode resistance and exhibited the lowest potential gap. These results were in agreement with the impedance measurements. As described above, the impedance spectra are composed of a semi-circle and an inclined line. The semi-circle is assigned to the charge-transfer impedance (R_{ct}) on the electrode, and the inclined line corresponds to the lithium-diffusion process within LFP electrodes. As shown in Figure 4.15-a and b the R_{ct} of the electrode was decreased and lithium-ion diffusion kinetics was increased with carbon coating. Accordingly, within the samples, the better cell performance delivered by LFP_B/C-600, which was consistent with the results from Figure 4.15 where LFP_B/C-600 exhibited the lowest resistance and highest ionic conductivity. Depolarization effects of the electrode were lowest at carbon coated samples using bilayer concentration at 600 °C. It can be concluded that carbon coating at a relatively optimum carbon content greatly enhance the electrochemical performance.



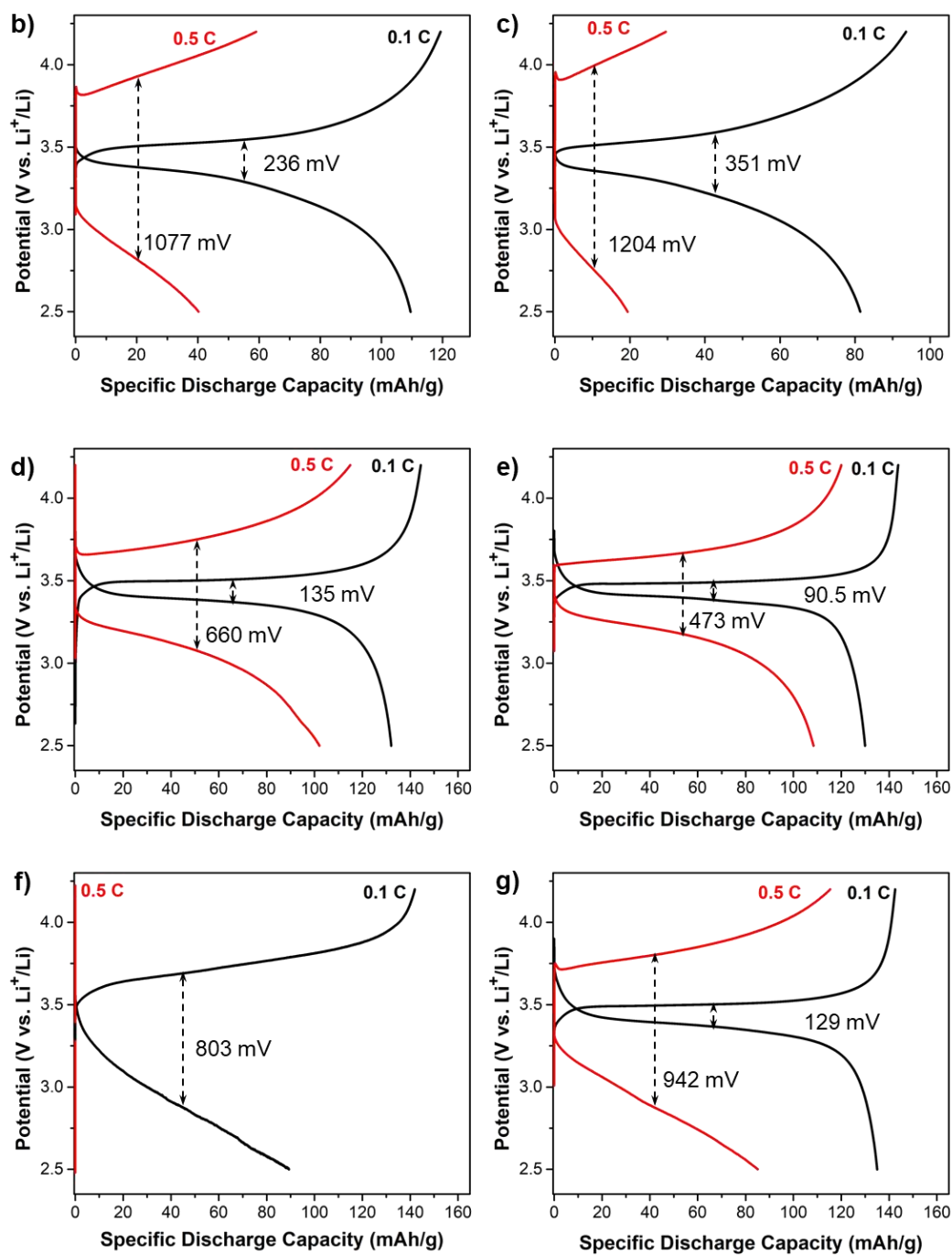


Figure 4.16. The charge/discharge voltage curves of a) LFP, and samples treated at 500 °C; b) LFF-HT-500, d) LFP_B/C-500, f) LFP_E/C-500 and 600 °C; c) LFF-HT-600, e) LFP_B/C-600, g) LFP_E/C-600

Since the LFP_E/C-600 showed better electrochemical performance and conductivity, the optimum temperature was chosen as 600 °C. Therefore, further analyses were done only with the samples of 600 °C. The carbon layer around LFP particles were further analyzed using TEM (Figure 4.17). In TEM analysis of the LFP-HT-600 sample (Figure 4.17 a and d) a thin carbon layer observed around the particle, and it was most probably originated from the EG residues remained on particles after synthesis. After pyrolysis of these samples at 600°C, the residue carbonized and formed a very thin carbon layer around particles.

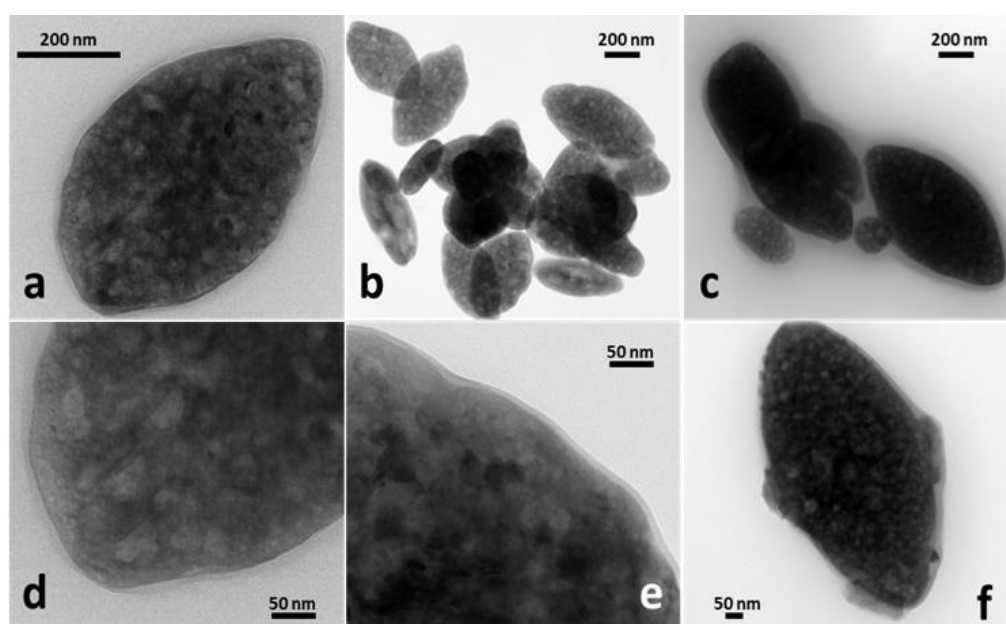


Figure 4.17. HRTEM images of the samples after 600°C heat treatment a) LFP-HT-600 b) LFP_B/C-600 c) LFP_E/C-600 d), e) and f) are corresponding high magnification images, respectively.

LFP_B/C-600 samples were dispersible, as seen in SEM micrographs and sedimentation analysis. The carbon layer was continuous and although the attachment of CTAB onto LFP surface was physical in the preparation of the suspension step, there was no gap at the interface of the particle surface and the carbon layer formed after pyrolysis. The carbon layer was uniform around the individual particles (Figure 4.17-e). Oppositely, the LFP_E/C-600 samples were

coated in clusters, the particles were buried in the carbon (Figure 4.17-c) and the necks between the particles were noteworthy. Even in the individual particles, the carbon layer was inhomogeneous (Figure 4.17-f). TEM nano-graphs clearly showed that the use of CTAB at optimum concentration was crucial to obtain homogeneous carbon coating around individual particles.

The amount of carbon content in particles was measured with a carbon-sulfur determinator as 1.38 ± 0.04 wt.% and 1.52 ± 0.04 wt.% for LFP_B/C-600 and LFP_E/C-600, respectively. The thickness of the carbon layer, seen in the TEM nanographs, showed that using CTAB at concentrations where bilayer is formed around particles led to a thinner layer whereas using excess CTAB led to a thicker one.

The amount of sulfur, on the other hand, was measured as 2.94 ± 0.23 wt.% in LFP_B/C-600 and 3.57 ± 0.07 wt.% in LFP_E/C-600 sample. The presence of sulfur in the bulk samples was attributed to FeSO₄ reagent used in the synthesis of LFP^[209]. It was also concluded that the presence of the sulfur in the samples might affect the electrochemical reaction during charging and discharging negatively^[210].

Molecular structure of the samples was investigated before and after heat treatment with ATR-FTIR analysis (Figure 4.18.) effect of the heat treatment and carbon coating on the surface of the particles were examined.

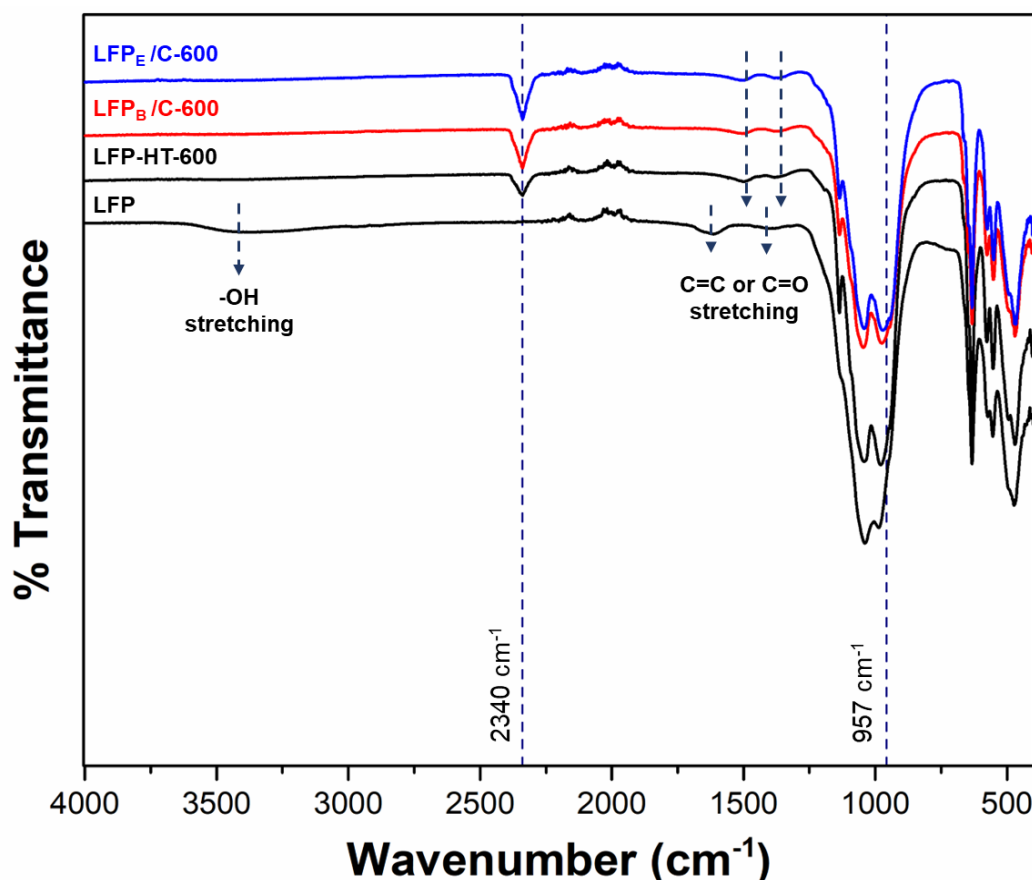


Figure 4.18. The ATR-FTIR spectra of the samples before heat treatment, LFP, and after 600°C heat treatment; LFP-HT-600 LFP_B/C-600 and LFP_E/C-600

The fingerprint region of the LFP electroactive material were between 1500 - 400 cm⁻¹ [211]. The part of the spectrum between 400 – 647 cm⁻¹ are bending modes: vibrations of symmetric and antisymmetric O-P-O and lithium [211]. The range of the spectrum between 945-1139 cm⁻¹ corresponds to the stretching mode of the (PO₄)³⁻ polyhedral units. The shift of P-O vibration around 957 cm⁻¹ towards 1000 cm⁻¹ is correlated to the lithium-iron (Li-Fe) antisite defect concentration of the LFP electroactive material [212]. As the shift was towards 1000 cm⁻¹, the antisite concentration increases and the opposite shift was reported vice versa. It was also reported that the increase in the antisite defect blocks the lithium-ion migration and reduce the electrochemical performance. In this study, it was seen observed that heat treatment of the as-synthesized LFP shifted the P-O vibration towards 957 cm⁻¹, and

carbon coating of the samples caused further shift towards 957 cm^{-1} . It was implied that antisite defect concentration of the samples were reduced with carbon coating process. The effect of the improvement of the carbon coating process were consistent with the electrochemical performance tests, it was noticed that the reaction kinetics of the samples were improved after carbon coating.

The peak, seen in the LFP sample, in the range of $3600\text{--}3100\text{ cm}^{-1}$ was assigned to the O-H stretching mode^[213] and this peak disappeared after heat treatment of LFP (LFP-HT-600). In the same sample, a new peak arose at 2340 cm^{-1} , which was attributed to $\text{C}\equiv\text{C}$ triple bond and it can be stemmed from carbonization of the ethylene glycol residue. The peaks seen at 1615 cm^{-1} and 1395 cm^{-1} was ascribed to $\text{C}=\text{C}$ or $\text{C}=\text{O}$ bonds^[214], arising from ethylene glycol used in the LFP synthesis medium. These peaks shifted towards lower wavenumber after heat treatment, as can be seen from the arrows, in Figure 4.18. The same changes were seen in the carbon coated samples (LFP_B/C-600 and LFP_E/C-600).

As stated in the introduction, the large particle size of active material has a significant negative impact on electrochemical properties due to limited lithium-ion diffusion into solid-state agglomerated particles. In the current study, similar behavior was observed; as the current rate increased, the discharge capacity decreased (Figure 4.16-b-d-f) and it might be due to the non-homogeneous distribution of agglomerated LFP particles in the cathode (supported by the SEM and TEM analyses). As a result, agglomeration state of the particles after carbon coating process played an important role in improving the electrochemical performance.

The chemical composition and valence state of LiFePO_4 and LiFePO_4/C material was confirmed by XPS analysis (Figure 4.19). In the figure, in the wide range-scanning spectrum shows peaks Li, Fe, P, O and C components confirming formation of LiFePO_4/C material. The Fe 2p spectrum exhibited two major peaks (Fe $2p_{3/2}$ and Fe $2p_{1/2}$) at binding energies of 710.9 eV and 724.2 eV indicating Fe(II) valence state which is characteristic of the olivine-type LiFePO_4 products^[215]. Due to fact that there is nitrogen in the chemical structure of CTAB, presence of nitrogen was

examined by XPS analysis in literature^[216]. However, the samples prepared in this study, nitrogen was not detected. Therefore, it can be concluded that the head group of the CTAB was decomposed during pyrolysis. Because the attachment of CTAB onto LFP was physical, losing of the head group of the CTAB was probable in pyrolysis step^[192].

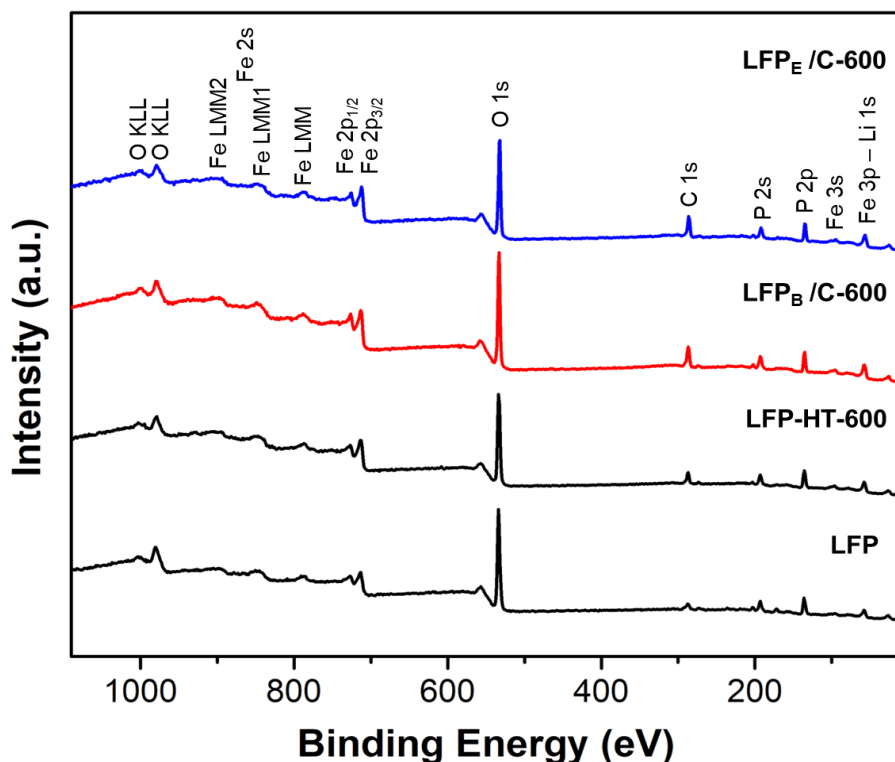


Figure 4.19. XPS spectra of the samples LFP and after 600°C heat treatment; LFP-HT-600 LFP_B/C-600 and LFP_E/C-600

Analyzing the C 1s core level spectra, the deconvolution (Figure 4.20) clearly displayed the lower binding energy featured at 284.62 eV corresponding to C-C carbon (sp^2 C) and the higher binding energy, featured around 285 eV corresponded to C-C (sp^3 C)^[217]. They were followed by C-O-C type carbon at 286 eV and a shoulder at 288.9 eV, which was typically assigned to O-C=O^[217, 218]. Graphitization degree of the samples were compared by the area under the peaks, denoted by sp^2 C and sp^3 C. The area ratio of sp^2/sp^3 was 1.06 for LFP (Figure 4.20-a), 3.07 for LFP-HT-600 (Figure 4.20-b). It was observed that the sp^2 carbon content on the as-

synthesized LFP sample was increased after heat treatment. It implied that the ethylene glycol residue on the LFP sample were graphitized after heat treatment. The samples pyrolyzed from CTAB-coated particles (LFP_B/C-600-Figure 4.20-c and LFP_E/C-600- Figure 4.20-d), on the other hand, had the area ratio of sp²/ sp³ of 8.23 and 1.01, respectively. Using CTAB at concentration to form bilayers around LFPS had higher sp² hybridization, *i.e.*, the degree of graphitization, after heat treated at 600 °C when compared to the one containing larger amount of CTAB. Even the as-synthesized forms of these samples showed the same trend. As the carbonization of CTAB was catalyzed by the presence of LFP particles according to the TGA results and the carbon is more homogeneously distributed around LFP particles according to TEM analysis, it is reasonable to conclude that the homogeneous distribution of carbon source on LFP surface led to more homogeneous distribution and better graphitization of carbon around LFP particles after the heat treatment.

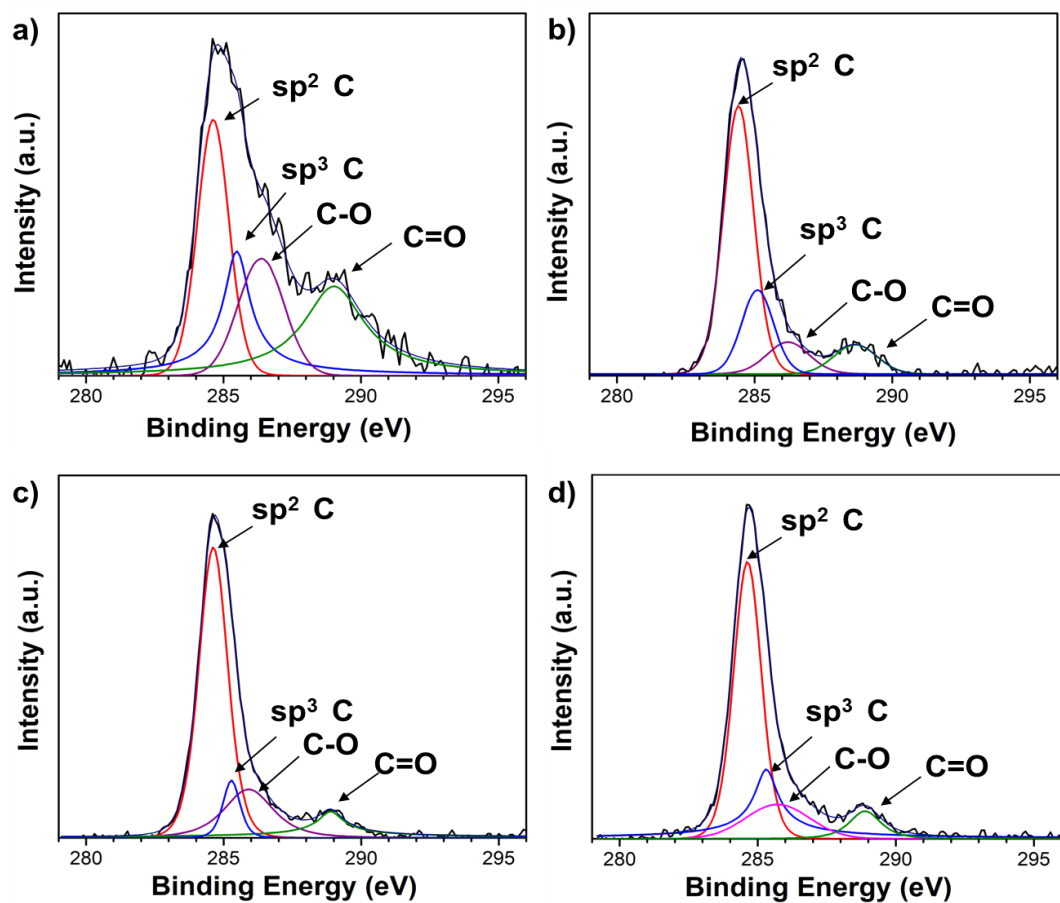


Figure 4.20. XPS spectra and deconvoluted peaks of the samples; a) LFP, b) LFP-HT, c) LFP_B/C-600 and d) LFP_E/C-600

The particles were further analyzed by Raman spectroscopy in order to investigate the nature of coated carbon Figure 4.21. The peaks appeared at 900 cm^{-1} belongs to the P-O vibration [219-221]. In Figure 4.21., while there was not any peak related to carbon, P-O vibrations were observed in the as-synthesized LFP sample. After treating these particles at 600°C , the carbon related peaks were appeared as expected from the presence of thin layer of carbon in TEM nanographs. The peaks denoted by D ($\sim 1300\text{ cm}^{-1}$) and G ($\sim 1590\text{ cm}^{-1}$) referring to the disordered and the graphitized carbon bands [116, 220-222]. As-synthesized LFP spectra did not show any carbon-related peak. After heat treatment of LFP at 600°C , D1 and G bands were observed. D1 and G bands in samples prepared using CTAB were much more intense than the as-synthesized LFP particles.

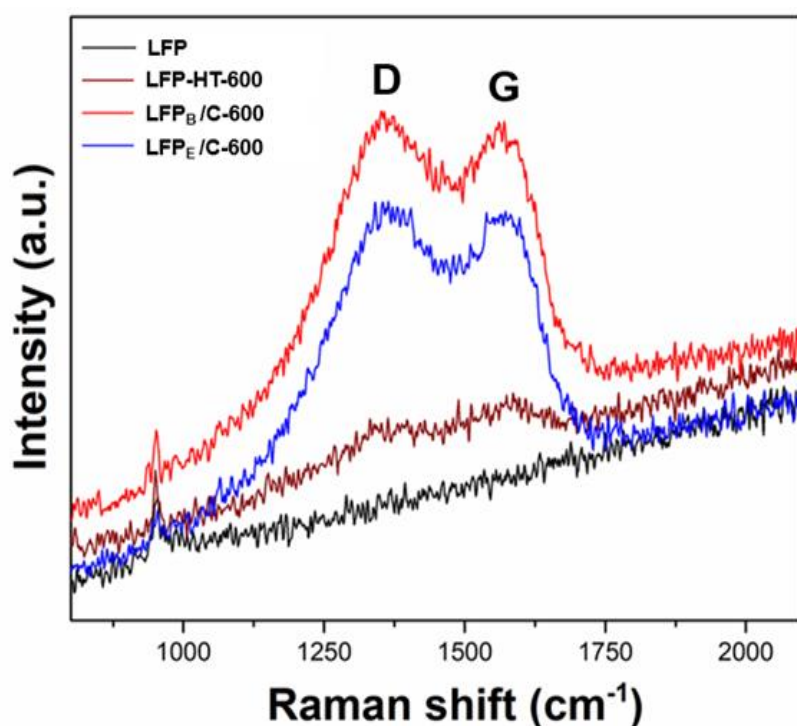


Figure 4.21. Raman analyses of the samples: LFP, LFP-HT-600, LFP_B/C -600, LFP_E/C -600

The deconvolution of the carbon peaks observed in the Raman Spectroscopy analysis presented in Figure 4.22. The Raman spectra deconvoluted into five peaks [54, 129, 223,

^{224]}. G band is related to the E_{2g} zone center mode of crystalline graphite. The D1 peak is assigned to the vibrational mode with A_{1g} symmetry of disordered graphitic lattice. The D2 band refers to highly defective graphitic lattice mode having E_{2g} symmetry. The D3 band is assigned to amorphous carbon. The D4 band is associated with diamond like carbon with short range vibrations of sp^3 carbon. The area of D1 band and G band (A_G/A_{D1}) is used to compare the degree of disorder between samples. This value was calculated as 0.87, 0.64, and 0.35 for LFP-HT-600, LFP_B/C-600 and LFP_E/C-600, respectively. It was observed that the ratio of the graphitized carbon peak area to the disordered carbon peak area was higher, *i.e.*, had larger amount of graphitized carbon, when the powders were prepared at optimum conditions, *i.e.*, using bilayer concentration of CTAB and treated at 600 °C. In line with XPS results, it can be deduced that the catalytic activity of LFP (or the iron in it) might be resulted in enhanced graphitization of carbons that were in direct contact with LFP particle surfaces. However, excess carbon that was trapped between the particles became carbonized but not sufficiently graphitized, which decreases conductivity and impairs dispersibility by resulting in neck formation. All in all, it can be concluded it is not only the carbon amount, but the graphitization degree and the distribution of carbon around particles are the critical properties what creates the difference in electrochemical performance.

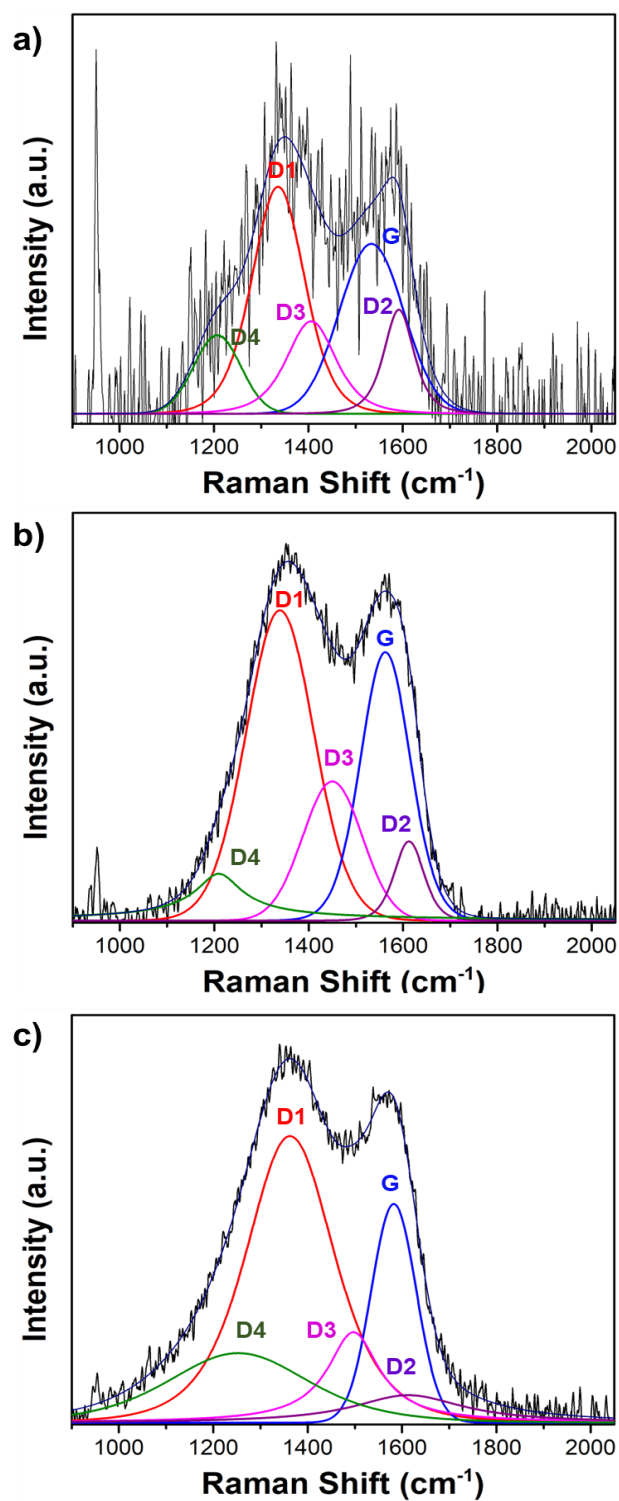


Figure 4.22. Deconvolution of Raman spectra in the wavenumber range of 900-2000 cm^{-1} for a) LFP-HT-600, b) LFP_B/C-600 and c) LFP_E/C-600

Lastly, the influence of preserving dispersibility of particles during carbon coating process on tap density of particles was investigated. As tabulated in Table 4.1, the carbon coated LFP particles using bilayer CTAB concentration ($LFP_{B/C}$) had almost the same packing as the LFP particles, whereas the carbon coated LFP particles using excess CTAB concentration ($LFP_{E/C}$) had lower packing density than LFP and $LFP_{B/C}$. Even though carbon coating process were applied to LFP particles, carbon coated particles preserved their individuality and dispersion quality when bilayer CTAB concentration was used and, carbon coated particles using excess CTAB concentration lost their dispersibility. It has been demonstrated that when the carbon coating was designed meticulously, therefore when the individually carbon-coated particles were synthesized, the carbon coating process would contribute to the chemical stability, mechanical integrity, electrical conductivity, and the electrochemical performance of the LFP particles without deteriorating its dispersibility. Increasing the electrochemical performance while keeping the tap density constant would lead to improvement in volumetric energy density in a battery system.

Table 4.1 Mean tap density values of as-synthesized LFP, carbon coated LFP samples; $LFP_{B/C}$ -600 and $LFP_{E/C}$ -600

Samples	<i>LFP</i>	<i>LFP_{B/C} -600</i>	<i>LFP_{E/C} -600</i>
Tap density (g·cm⁻¹)	1.11 ± 0.06	1.16 ± 0.08	1.01 ± 0.08

CHAPTER 5

CONCLUSIONS AND FURTHER RECOMMENDATIONS

The carbon coating process is just as significant as particle design to improve volumetric energy density of electroactive particles. In this thesis, an *ex-situ* carbon coating procedure enabling to synthesize carbon coated individual particles was developed.

To ensure full coverage and individual carbon coating, colloidal principles were utilized. To this end, cationic surfactant, CTAB, was chosen as a carbon source because it is positively charged in aqueous media, so that it preferentially interacted with the negatively charged electroactive material, LFP. Based on the changes in the colloidal behavior of particles, the mechanism of CTAB coating on LFP particles were revealed. The isoelectric point of LFP particles was reached with addition of 0.05 mM CTAB into LFP suspensions with solids loading of 0.01 wt.%, corresponding to monolayer CTAB coverage of LFP particles. At this point, particles were destabilized and separated at the bottom of the container. Further addition of CTAB into solution re-stabilized the LFP particles and homogeneous particle suspension was obtained again. Based on the behavioral changes in the zeta potential of LFP particles and the solution conductivities, the CTAB concentration at which the bilayer as formed estimated as 1.82 CTAB(g) / LFP(g) corresponding to 0.5 mM CTAB concentration. Further addition of CTAB molecules were predicted to move freely between CTAB-coated-LFP particles.

In order to increase the amount of LFP particles coated with CTAB, the system was scaled-up as an advantage of designed process, and the solids loading was increased to 0.1 wt.%. All the critical parameters were re-determined. It was realized that the monolayer coverage was obtained at the same CTAB concentration with the dilute

system, at 0.05 mM of CTAB in both dilute and concentrated system, and the bilayer coverage was obtained at the same CTAB(g) / LFP(g) ratio of 1.82, corresponding to 5 mM CTAB concentration in concentrated system. Three samples were selected to be used in the pyrolysis step: bare LFP, LFP with bilayer CTAB coverage, and LFP with excess CTAB.

The heating procedure and the pyrolysis temperatures were investigated. From TGA analysis, it was realized that CTAB completely transforms into gaseous species, when heated alone, but it carbonized when it was located on LFP surface, and the heating procedure were optimized. The heat treatment was employed in an oven tube with controlled argon atmosphere. The powders were first heated to 300 °C with heating rate of 2 °C/min, hold at this temperature for an hour, then heated to elevated temperatures with heating rate of 10 °C/min and the sample hold at this temperature for three hours. The heat treatments were employed at 500 °C, 600 °C and 700 °C, and among them 600 °C were found to be optimum based on the purity and the dispersibility of the treated samples.

According to the dispersibility of particles, carbon coating characteristics (homogeneity, the degree of graphitization, homogeneity), conductivity, electrochemical performance, and the tap density of particles, the CTAB concentration corresponding to bilayer coverage was found to be optimum to synthesize individual carbon coated particles. The excess amount of carbon source, in our case, CTAB, caused negative effects in the dispersibility, the electrochemical performance and the other properties of LFP particles. The LFP particles coated with this optimum amount of carbon, 1.38 wt.% carbon, led to the specific discharge capacity of 130 mAh·g⁻¹ in an organic electrolyte and tap density of 1.16 g·cm⁻³. The specific discharge capacity of the LFP particles were increased from 92 mAh·g⁻¹ to this value with the contribution of carbon coating. The electrochemical performance of the particles can further be improved if the initial LFP particles with designed crystal structure are used as a starting material. Moreover, sulfur was found to be present in carbon coated particles. Elimination of this sulfur content with additional washing procedure may result in further improvement in electrochemical

performance. Pyrolysis conditions can further be optimized to preserve the head group of the CTAB having nitrogen, to obtain nitrogen doped carbon layer, which was reported to exhibit specific discharge capacities close to the theoretical value. To increase the graphitization degree of the carbon layer without employing high temperatures, graphitization catalysts such as ferrocene, pyromellitic acid etc. can be introduced to the system before pyrolysis to improve the electrochemical performance of the particles. None of these recommendations possesses a threat to deteriorate the dispersibility of the particles obtained in this study.

Because particles were individually carbon coated, it was expected that using these particles would lead to lower suspension electrode viscosity and better processing of electrodes and higher volumetric energy density compared to agglomerated counterparts.

The developed *ex-situ* carbon coating methodology enabled to compare the sole effect of carbon coating and investigation of the direct influence of the carbon coating characteristics. Moreover, utilization of the colloidal principles in carbon coating enabled to determine the optimum carbon source amount and individual carbon coating of particles and there is no obvious limitation to employ such a procedure to any electroactive material.

Surfactants have a broad spectrum of functional groups and the carbon chain lengths. The presence of aromatic groups, which may provide better graphitization and adsorption ability or some elements such as nitrogen adapting the carbon electronic structure of the carbon layer is advantageous to achieve a high degree of graphitization and specific capacity. Using different surfactants with different chemistry and/or chain length has a potential to tune the thickness and other properties of the carbon coating layer. The procedure developed in this thesis can simply be tuned to further optimized the carbon coating characteristics, and thus it is robust.

REFERENCES

1. Arnold, G., et al., Fine-particle lithium iron phosphate LiFePO₄ synthesized by a new low-cost aqueous precipitation technique. *Journal of Power Sources*, 2003. 119: p. 247-251.
2. Padhi, A.K., K.S. Nanjundaswamy, and J.B. Goodenough, Phospho-olivines as positive-electrode materials for rechargeable lithium batteries. *Journal of the electrochemical society*, 1997. 144(4): p. 1188.
3. Gaines, L.L. and J.B. Dunn, Lithium-ion battery environmental impacts, in *Lithium-Ion Batteries*. 2014, Elsevier. p. 483-508.
4. Wang, J. and X. Sun, Understanding and recent development of carbon coating on LiFePO₄ cathode materials for lithium-ion batteries. *Energy & Environmental Science*, 2012. 5(1): p. 5163-5185.
5. Li, H. and H. Zhou, Enhancing the performances of Li-ion batteries by carbon-coating: present and future. *Chemical Communications*, 2012. 48(9): p. 1201-1217.
6. Zhang, W.-J., Structure and performance of LiFePO₄ cathode materials: A review. *Journal of Power Sources*, 2011. 196(6): p. 2962-2970.
7. Garg, B., *Introduction to Flow Batteries: Theory and Applications*. 2016, Stanford University: Stanford, CA, USA.
8. Jin, S., et al., A water-miscible quinone flow battery with high volumetric capacity and energy density. *ACS Energy Letters*, 2019. 4(6): p. 1342-1348.
9. Whittingham, M.S., Materials challenges facing electrical energy storage. *Mrs Bulletin*, 2008. 33(4): p. 411-419.

10. Dixit, M., et al., SolidPAC is an interactive battery-on-demand energy density estimator for solid-state batteries. *Cell Reports Physical Science*, 2022. 3(2): p. 100756.
11. Chang, B., et al., A high-tap-density nanosphere-assembled microcluster to simultaneously enable high gravimetric, areal and volumetric capacities: a case study of TiO₂ anode. *Journal of Materials Chemistry A*, 2018. 6(25): p. 11916-11928.
12. Wang, X., et al., Facile synthesis and electrochemical properties of high tap density LiFePO₄/C. *Ionics*, 2019. 25(10): p. 4589-4596.
13. Chen, Z. and J. Dahn, Reducing carbon in LiFePO₄/C composite electrodes to maximize specific energy, volumetric energy, and tap density. *Journal of the Electrochemical Society*, 2002. 149(9): p. A1184.
14. Jain, R., et al., Nanostructuring versus microstructuring in battery electrodes. *Nature Reviews Materials*, 2022: p. 1-11.
15. Oh, S.W., et al., The effect of morphological properties on the electrochemical behavior of high tap density C–LiFePO₄ prepared via coprecipitation. *Journal of the Electrochemical Society*, 2008. 155(6): p. A414.
16. Wang, L., et al., Spherical metal oxides with high tap density as sulfur host to enhance cathode volumetric capacity for lithium–sulfur battery. *ACS applied materials & interfaces*, 2020. 12(5): p. 5909-5919.
17. Xu, G., et al., Monodispersed LiFePO₄@ C core–shell nanostructures for a high power Li-ion battery cathode. *Journal of power sources*, 2014. 246: p. 696-702.

18. Sun, C., et al., Monodisperse porous LiFePO₄ microspheres for a high power Li-ion battery cathode. *Journal of the American Chemical Society*, 2011. 133(7): p. 2132-2135.
19. Qi, Z. and G.M. Koenig Jr, Flow battery systems with solid electroactive materials. *Journal of Vacuum Science & Technology B, Nanotechnology and Microelectronics: Materials, Processing, Measurement, and Phenomena*, 2017. 35(4): p. 040801.
20. Manthiram, A., An outlook on lithium ion battery technology. *ACS central science*, 2017. 3(10): p. 1063-1069.
21. Ciosek Högström, K., The Complex Nature of the Electrode/Electrolyte Interfaces in Li-ion Batteries: Towards Understanding the Role of Electrolytes and Additives Using Photoelectron Spectroscopy. 2014, Acta Universitatis Upsaliensis.
22. Xin, Y.-M., et al., A Review on Application of LiFePO₄ based composites as electrode materials for Lithium Ion Batteries. *Int. J. Electrochem. Sci*, 2021. 16: p. 210655.
23. Liu, X., K. Li, and X. Li, The electrochemical performance and applications of several popular lithium-ion batteries for electric vehicles-a review. *Advances in Green Energy Systems and Smart Grid*, 2018: p. 201-213.
24. Nitta, N., et al., Li-ion battery materials: present and future. *Materials today*, 2015. 18(5): p. 252-264.
25. Kim, T., et al., Applications of voltammetry in lithium ion battery research. *Journal of Electrochemical Science and Technology*, 2020. 11(1): p. 14-25.
26. Yaroslavtsev, A.B. and I.A. Stenina, Carbon coating of electrode materials for lithium-ion batteries. *Surface Innovations*, 2020. 9(2-3): p. 92-110.

27. Lee, W.J., et al., Nitrogen-doped carbon nanotubes and graphene composite structures for energy and catalytic applications. *Chemical Communications*, 2014. 50(52): p. 6818-6830.
28. Liu, H., et al., Doping effects of zinc on LiFePO₄ cathode material for lithium ion batteries. *Electrochemistry communications*, 2006. 8(10): p. 1553-1557.
29. Wang, D., et al., Improving the rate performance of LiFePO₄ by Fe-site doping. *Electrochimica Acta*, 2005. 50(14): p. 2955-2958.
30. Liu, N., et al., A pomegranate-inspired nanoscale design for large-volume-change lithium battery anodes. *Nature nanotechnology*, 2014. 9(3): p. 187-192.
31. Prosini, P.P., et al., Long-term cyclability of nanostructured LiFePO₄. *Electrochimica Acta*, 2003. 48(28): p. 4205-4211.
32. Bi, Z., et al., Recent advances in LiFePO₄ nanoparticles with different morphology for high-performance lithium-ion batteries. *RSC Advances*, 2013. 3(43): p. 19744-19751.
33. Nan, C., et al., Size and shape control of LiFePO₄ nanocrystals for better lithium ion battery cathode materials. *Nano Research*, 2013. 6(7): p. 469-477.
34. Shobana, M., Metal oxide coated cathode materials for Li ion batteries—A review. *Journal of Alloys and Compounds*, 2019. 802: p. 477-487.
35. Somo, T.R., et al., A comparative review of metal oxide surface coatings on three families of cathode materials for lithium ion batteries. *Coatings*, 2021. 11(7): p. 744.
36. Chen, Z., Q. Zhang, and Q. Liang, Carbon-Coatings Improve Performance of Li-Ion Battery. *Nanomaterials*, 2022. 12(11): p. 1936.

37. Zhou, L., et al., Carbon-Based Modification Materials for Lithium-ion Battery Cathodes: Advances and Perspectives. *Frontiers in Chemistry*, 2022. 10.
38. Wang, Y., et al., The design of a LiFePO₄/carbon nanocomposite with a core-shell structure and its synthesis by an in situ polymerization restriction method. *Angewandte Chemie International Edition*, 2008. 47(39): p. 7461-7465.
39. Nisar, U., et al., Valuation of surface coatings in high-energy density lithium-ion battery cathode materials. *Energy Storage Materials*, 2021. 38: p. 309-328.
40. Ahsan, Z., et al., Recent progress in capacity enhancement of LiFePO₄ cathode for Li-ion batteries. *Journal of Electrochemical Energy Conversion and Storage*, 2021. 18(1): p. 010801.
41. Gören, A., et al., State of the art and open questions on cathode preparation based on carbon coated lithium iron phosphate. *Composites Part B: Engineering*, 2015. 83: p. 333-345.
42. Park, H.-S., et al., Catalytic carbonization of an uncarbonizable precursor by transition metals in olivine cathode materials of lithium ion batteries. *Journal of Materials Chemistry*, 2012. 22(38): p. 20305-20310.
43. Kurilenko, K.A., et al., Effect of nanostructured carbon coatings on the electrochemical performance of Li_{1-x}Ni_{0.5}Mn_{0.5}O₂-based cathode materials. *Beilstein Journal of Nanotechnology*, 2016. 7(1): p. 1960-1970.
44. Piccone, A., *Designing Lithium-Ion Batteries to Charge Faster, Last Longer*. 2021, AIP Publishing LLC.

45. Qi, Z.-y., et al., Optimizing the carbon coating to eliminate electrochemical interface polarization in a high performance silicon anode for use in a lithium-ion battery. *New Carbon Materials*, 2022. 37(1): p. 245-258.
46. Yang, J., et al., Carbon-coated LiCrTiO₄ electrode material promoting phase transition to reduce asymmetric polarization for lithium-ion batteries. *Physical Chemistry Chemical Physics*, 2014. 16(7): p. 2882-2891.
47. Cao, H., et al., Application and prospects for using carbon materials to modify lithium iron phosphate materials used at low temperatures. *New Carbon Materials*, 2022. 37(1): p. 46-58.
48. Zhu, S., A. Huang, and Y. Xu, Improving Methods for better Performance of Commercial LiFePO₄/C Batteries. *International Journal of Electrochemical Science*, 2021. 16(5).
49. Wang, K.X., X.H. Li, and J.S. Chen, Surface and interface engineering of electrode materials for lithium-ion batteries. *Advanced Materials*, 2015. 27(3): p. 527-545.
50. Li, W., J.R. Dahn, and D.S. Wainwright, Rechargeable lithium batteries with aqueous electrolytes. *Science*, 1994. 264(5162): p. 1115-1118.
51. Luo, J.-Y., et al., Raising the cycling stability of aqueous lithium-ion batteries by eliminating oxygen in the electrolyte. *Nature chemistry*, 2010. 2(9): p. 760-765.
52. Recham, N., et al., Ionothermal synthesis of Li-based fluorophosphates electrodes. *Chemistry of materials*, 2010. 22(3): p. 1142-1148.
53. Subramanya, U., et al., Carbon-based artificial SEI layers for aqueous lithium-ion battery anodes. *RSC advances*, 2020. 10(2): p. 674-681.

54. Zhu, Z., F. Cheng, and J. Chen, Investigation of effects of carbon coating on the electrochemical performance of $\text{Li}_4\text{Ti}_5\text{O}_{12}/\text{C}$ nanocomposites. *Journal of Materials Chemistry A*, 2013. 1(33): p. 9484-9490.
55. Scipioni, R., et al., Electron microscopy investigations of changes in morphology and conductivity of LiFePO_4/C electrodes. *Journal of Power Sources*, 2016. 307: p. 259-269.
56. Su, L., Y. Jing, and Z. Zhou, Li ion battery materials with core-shell nanostructures. *Nanoscale*, 2011. 3(10): p. 3967-3983.
57. Zaghbi, K., et al., Surface effects on the physical and electrochemical properties of thin LiFePO_4 particles. *Chemistry of Materials*, 2008. 20(2): p. 462-469.
58. Genovese, D.B., Shear rheology of hard-sphere, dispersed, and aggregated suspensions, and filler-matrix composites. *Advances in colloid and interface science*, 2012. 171: p. 1-16.
59. Mishra, P.C., et al., A brief review on viscosity of nanofluids. *International nano letters*, 2014. 4(4): p. 109-120.
60. Kawassaki, R.K., et al., Titanium and iron oxide nanoparticles for cancer therapy: surface chemistry and biological implications. *Frontiers in Nanotechnology*, 2021. 3: p. 735434.
61. Reynolds, C.D., et al., Rheology and Structure of Lithium-Ion Battery Electrode Slurries. *Energy Technology*.
62. Wang, Y., et al., Effect of particle dispersion on the properties of LiFePO_4 slurry and the electrochemical properties of the battery. *Ionics*, 2022. 28(4): p. 1547-1558.

63. Neyhouse, B.J., et al. Modeling Electrochemical and Rheological Characteristics of Suspension-Based Electrolytes for Redox Flow Batteries. in ECS Meeting Abstracts. 2022. IOP Publishing.
64. Cao, D., et al., High Performance Aqueous Li-Ion Flow Capacitor Realized Through Microstructure Design of Suspension Electrode. *Frontiers in chemistry*, 2021: p. 213.
65. Gaberscek, M., R. Dominko, and J. Jamnik, Is small particle size more important than carbon coating? An example study on LiFePO₄ cathodes. *Electrochemistry Communications*, 2007. 9(12): p. 2778-2783.
66. Fu, F., et al., Structure dependent electrochemical performance of Li-rich layered oxides in lithium-ion batteries. *Nano Energy*, 2017. 35: p. 370-378.
67. Li, Z., et al., Controlled Hydrothermal/Solvothermal Synthesis of High-Performance LiFePO₄ for Li-Ion Batteries. *Small Methods*, 2021. 5(6): p. 2100193.
68. Zhang, L., et al., Rod-like hierarchical nano/micro Li_{1.2}Ni_{0.2}Mn_{0.6}O₂ as high performance cathode materials for lithium-ion batteries. *Journal of power sources*, 2013. 240: p. 644-652.
69. Zhou, S., et al., Crystal structural design of exposed planes: express channels, high-rate capability cathodes for lithium-ion batteries. *Nanoscale*, 2018. 10(37): p. 17435-17455.
70. Bhuvaneshwari, D. and N. Kalaiselvi, In situ carbon coated LiFePO₄/C microrods with improved lithium intercalation behavior. *Physical Chemistry Chemical Physics*, 2014. 16(4): p. 1469-1478.
71. Li, J., Q. Wu, and J. Wu, Synthesis of nanoparticles via solvothermal and hydrothermal methods, in *Handbook of nanoparticles*. 2016, Springer. p. 295-328.

72. Bresser, D., et al., Challenges of “going nano”: enhanced electrochemical performance of cobalt oxide nanoparticles by carbothermal reduction and in situ carbon coating. *ChemPhysChem*, 2014. 15(10): p. 2177-2185.
73. Qi, M., et al., Improved electrochemical performances of carbon-coated LiFePO₄ microspheres for Li-ion battery cathode. *Materials Research Express*, 2019. 6(11): p. 115520.
74. Pratheeksha, P.M., et al., Investigation of in-situ carbon coated LiFePO₄ as a superior cathode material for lithium ion batteries. *Journal of Nanoscience and Nanotechnology*, 2019. 19(5): p. 3002-3011.
75. Li, W., et al., Plate-like LiFePO₄/C composite with preferential (010) lattice plane synthesized by cetyltrimethylammonium bromide-assisted hydrothermal carbonization. *Journal of Alloys and Compounds*, 2015. 651: p. 34-41.
76. Vasu, S., et al., In-situ carbon encapsulation of LiNi_{1/3}Co_{1/3}Mn_{1/3}O₂ using pillared ethylene glycol trapped in the metal hydroxide interlayers for enhanced cyclic stability. *Electrochimica Acta*, 2017. 251: p. 363-377.
77. Bao, L., et al., Mono-dispersed LiFePO₄@ C core-shell [001] nanorods for a high power Li-ion battery cathode. *Journal of Alloys and Compounds*, 2017. 100(708): p. 685-693.
78. Miao, C., et al., A novel synthesis and characterization of LiFePO₄ and LiFePO₄/C as a cathode material for lithium-ion battery. *Journal of Power Sources*, 2014. 100(246): p. 232-238.
79. Świder, J., et al., Enhancement of electrochemical performance of LiFePO₄ nanoparticles by direct nanocoating with conductive carbon layers. *Functional Materials Letters*, 2016. 9(04): p. 1641007.

80. Huo, T., et al., Naphthalene-modulated microporous carbon layers of LiFePO₄ improve the high-rate electrochemical performance. *Journal of energy chemistry*, 2019. 30: p. 84-89.
81. Nan, C., et al., Solvothermal synthesis of lithium iron phosphate nanoplates. *Journal of Materials Chemistry*, 2011. 21(27): p. 9994-9996.
82. Yang, S., et al., Solvothermal synthesis of monodisperse LiFePO₄ micro hollow spheres as high performance cathode material for lithium ion batteries. *ACS applied materials & interfaces*, 2013. 5(18): p. 8961-8967.
83. Zhu, J., et al., Solution deposition of thin carbon coatings on LiFePO₄. *ACS applied materials & interfaces*, 2014. 6(23): p. 21550-21557.
84. Murugan, A.V., T. Muraliganth, and A. Manthiram, Comparison of microwave assisted solvothermal and hydrothermal syntheses of LiFePO₄/C nanocomposite cathodes for lithium ion batteries. *The Journal of Physical Chemistry C*, 2008. 112(37): p. 14665-14671.
85. Pei, B., et al., Hydrothermal synthesis of morphology-controlled LiFePO₄ cathode material for lithium-ion batteries. *Journal of Power Sources*, 2012. 220: p. 317-323.
86. Su, C., et al., Preparation of LiFePO₄/Carbon/PANI-CSA composite and its properties as high-capacity cathodes for lithium ion batteries. *Journal of the Electrochemical Society*, 2012. 159(3): p. A305.
87. Ding, B., et al., Ultrathin carbon nanopainting of LiFePO₄ by oxidative surface polymerization of dopamine. *Journal of Power Sources*, 2014. 265: p. 239-245.
88. Xiong, Q., et al., Controllable synthesis of NC@ LiFePO₄ nanospheres as advanced cathode of lithium ion batteries. *Journal of Alloys and Compounds*, 2018. 743: p. 377-382.

89. Buc, E.C., Review of "Fire Debris Analysis" by Eric Stauffer, Julia Dolan, and Reta Newman, Academic Press, 2007.(Hardbound, 672 pages, ISBN-10: 0-12-663971-1, USD 99.95). 2008, Springer.
90. Ramirez, A., T. Itoh, and R. Sinclair, Crystallization of amorphous carbon thin films in the presence of magnetic media. *Journal of applied physics*, 1999. 85(3): p. 1508-1513.
91. Brunner, P.H. and P.V. Roberts, The significance of heating rate on char yield and char properties in the pyrolysis of cellulose. *Carbon*, 1980. 18(3): p. 217-224.
92. Lin, C. and J.A. Ritter, Carbonization and activation of sol-gel derived carbon xerogels. *Carbon*, 2000. 38(6): p. 849-861.
93. Norinaga, K. and K.J. Hüttinger, Kinetics of surface reactions in carbon deposition from light hydrocarbons. *Carbon*, 2003. 41(8): p. 1509-1514.
94. Williams, P.T. and S. Besler, The influence of temperature and heating rate on the slow pyrolysis of biomass. *Renewable energy*, 1996. 7(3): p. 233-250.
95. Dresselhaus, M.S. and P. Avouris, Introduction to carbon materials research, in *Carbon nanotubes*. 2001, Springer. p. 1-9.
96. Sun, Z., et al., Structure and properties of hard carbon films depending on heat treatment temperatures via polymer precursor. *Diamond and related materials*, 1999. 8(6): p. 1107-1113.
97. Devi, M., S. Rawat, and S. Sharma, A comprehensive review of the pyrolysis process: From carbon nanomaterial synthesis to waste treatment. *Oxford Open Materials Science*, 2021. 1(1): p. itab014.

98. Su, D.S. and R. Schlögl, Nanostructured carbon and carbon nanocomposites for electrochemical energy storage applications. *ChemSusChem: Chemistry & Sustainability Energy & Materials*, 2010. 3(2): p. 136-168.
99. Qin, G., et al., Exploring T-carbon for energy applications. *Nanoscale*, 2019. 11(13): p. 5798-5806.
100. Cheng, L., et al., Carbon-coated $\text{Li}_4\text{Ti}_5\text{O}_{12}$ as a high rate electrode material for Li-ion intercalation. *Journal of the Electrochemical Society*, 2007. 154(7): p. A692.
101. Xi, Y. and Y. Lu, Toward uniform in situ carbon coating on nano- LiFePO_4 via a solid-state reaction. *Industrial & Engineering Chemistry Research*, 2020. 59(30): p. 13549-13555.
102. Trudeau, M., et al., In situ high-resolution transmission electron microscopy synthesis observation of nanostructured carbon coated LiFePO_4 . *Journal of Power Sources*, 2011. 196(18): p. 7383-7394.
103. Krumeich, F., O. Waser, and S.E. Pratsinis, Thermal annealing dynamics of carbon-coated LiFePO_4 nanoparticles studied by in-situ analysis. *Journal of Solid State Chemistry*, 2016. 242: p. 96-102.
104. Dixit, A., et al., Effect of Iron-based Impurities on the performance of nanostructured C- LiFePO_4 cathode material for Li ion Batteries.
105. Julien, C., et al., Nanoscopic scale studies of LiFePO_4 as cathode material in lithium-ion batteries for HEV application. *Ionics*, 2007. 13(6): p. 395-411.
106. Liu, Y., et al., Formation of size-dependent and conductive phase on lithium iron phosphate during carbon coating. *Nature communications*, 2018. 9(1): p. 1-8.

107. Wang, J., et al., Size-dependent surface phase change of lithium iron phosphate during carbon coating. *Nature communications*, 2014. 5(1): p. 1-8.
108. Wang, J., et al., Interaction of carbon coating on LiFePO₄: a local visualization study of the influence of impurity phases. *Advanced Functional Materials*, 2013. 23(7): p. 806-814.
109. Rho, Y.-H., et al., Surface chemistry of LiFePO₄ studied by Mössbauer and X-ray photoelectron spectroscopy and its effect on electrochemical properties. *Journal of the Electrochemical Society*, 2007. 154(4): p. A283.
110. Saroha, R. and A.K. Panwar, Effect of in situ pyrolysis of acetylene (C₂H₂) gas as a carbon source on the electrochemical performance of LiFePO₄ for rechargeable lithium-ion batteries. *Journal of Physics D: Applied Physics*, 2017. 50(25): p. 255501.
111. Asoro, M., D. Kovar, and P. Ferreira, Effect of surface carbon coating on sintering of silver nanoparticles: in situ TEM observations. *Chemical Communications*, 2014. 50(37): p. 4835-4838.
112. Rahaman, M.N., *Ceramic processing and sintering*. 2017: CRC press.
113. Shongwe, M., et al., Effect of starting powder particle size and heating rate on spark plasma sintering of FeNi alloys. *Journal of Alloys and compounds*, 2016. 678: p. 241-248.
114. Broitman, E. and L. Hultman, *Advanced carbon-based coatings*. 2014.
115. Kim, M.-A., et al., Strengthened PAN-based carbon fibers obtained by slow heating rate carbonization. *Scientific reports*, 2016. 6(1): p. 1-7.
116. Goers, D., et al., Raman spectroscopic and structural studies of heat-treated graphites for lithium-ion batteries. *Ionics*, 2003. 9(3): p. 258-265.

117. Mauger, A. and C. Julien, Surface modifications of electrode materials for lithium-ion batteries: status and trends. *Ionics*, 2014. 20(6): p. 751-787.
118. Basu, P., Biomass gasification, pyrolysis and torrefaction: practical design and theory. 2018: Academic press.
119. Tang, M.M. and R. Bacon, Carbonization of cellulose fibers—I. Low temperature pyrolysis. *Carbon*, 1964. 2(3): p. 211-220.
120. Denis, Y., et al., Impurities in LiFePO₄ and their influence on material characteristics. *Journal of The Electrochemical Society*, 2008. 155(7): p. A526.
121. Wu, S.-h., J.-J. Shiu, and J.-Y. Lin, Effects of Fe₂P and Li₃PO₄ additives on the cycling performance of LiFePO₄/C composite cathode materials. *Journal of Power Sources*, 2011. 196(16): p. 6676-6681.
122. Kang, B. and G. Ceder, Battery materials for ultrafast charging and discharging. *Nature*, 2009. 458(7235): p. 190-193.
123. Zhao, S.-X., et al., Improving rate performance of LiFePO₄ cathode materials by hybrid coating of nano-Li₃PO₄ and carbon. *Journal of Alloys and Compounds*, 2013. 566: p. 206-211.
124. Salah, A.A., et al., Reduction Fe³⁺ of impurities in LiFePO₄ from pyrolysis of organic precursor used for carbon deposition. *Journal of the Electrochemical Society*, 2006. 153(9): p. A1692.
125. Kim, D.-K., et al., Effect of synthesis conditions on the properties of LiFePO₄ for secondary lithium batteries. *Journal of Power Sources*, 2006. 159(1): p. 237-240.
126. Herle, P.S., et al., Nano-network electronic conduction in iron and nickel olivine phosphates. *Nature materials*, 2004. 3(3): p. 147-152.

127. Jiang, W., et al., Variation of carbon coatings on the electrochemical performance of LiFePO₄ cathodes for lithium ionic batteries. RSC advances, 2017. 7(70): p. 44296-44302.
128. Doeff, M.M., et al., Impact of carbon structure and morphology on the electrochemical performance of LiFePO₄/C composites. Journal of Solid State Electrochemistry, 2008. 12(7): p. 995-1001.
129. Wilcox, J.D., et al., Factors influencing the quality of carbon coatings on LiFePO₄. Journal of the Electrochemical Society, 2007. 154(5): p. A389.
130. Yoon, S., et al., Conductive surface modification of LiFePO₄ with nitrogen-doped carbon layers for lithium-ion batteries. Journal of Materials Chemistry, 2012. 22(11): p. 4611-4614.
131. Zhu, G.-N., C.-X. Wang, and Y.-Y. Xia, A comprehensive study of effects of carbon coating on Li₄Ti₅O₁₂ anode material for lithium-ion batteries. Journal of the Electrochemical Society, 2010. 158(2): p. A102.
132. Li, C.-C., S.-J. Chang, and C.-A. Chen, Effects of sp²-and sp³-carbon coatings on dissolution and electrochemistry of water-based LiFePO₄ cathodes. Journal of Applied Electrochemistry, 2017. 47(9): p. 1065-1072.
133. Li, C.-C., C.-A. Chen, and M.-F. Chen, Gelation mechanism of organic additives with LiFePO₄ in the water-based cathode slurries. Ceramics International, 2017. 43: p. S765-S770.
134. Tsai, F.-Y., et al., Dispersion, agglomeration, and gelation of LiFePO₄ in water-based slurry. Journal of Power Sources, 2016. 310: p. 47-53.
135. Tsai, J.-C., et al., Gelation or dispersion of LiFePO₄ in water-based slurry? Journal of power sources, 2013. 241: p. 400-403.

136. Cheng, F., et al., Functional materials for rechargeable batteries. *Advanced materials*, 2011. 23(15): p. 1695-1715.
137. Tao, H., et al., Reality and future of rechargeable lithium batteries. *The Open Materials Science Journal*, 2011. 5(1).
138. Flatt, R., Towards a prediction of superplasticized concrete rheology. *Materials and Structures*, 2004. 37(5): p. 289-300.
139. Jin, Y., et al., High-tap density LiFePO₄ microsphere developed by combined computational and experimental approaches. *CrystEngComm*, 2018. 20(42): p. 6695-6703.
140. Oh, S.W., et al., Double carbon coating of LiFePO₄ as high rate electrode for rechargeable lithium batteries. *Advanced materials*, 2010. 22(43): p. 4842-4845.
141. Zhong, M. and Z. Zhou, Preparation of high tap-density LiFePO₄/C composite cathode materials by carbothermal reduction method using two kinds of Fe³⁺ precursors. *Materials Chemistry and Physics*, 2010. 119(3): p. 428-431.
142. Amidon, G., P. Meyer, and D. Mudie, Chapter 10-Particle, Powder, and Compact Characterization. *Developing Solid Oral Dosage Forms*, 2017: p. 271-293.
143. Liu, Z., X. Zhang, and L. Hong, Preparation and electrochemical properties of spherical LiFePO₄ and LiFe_{0.9}Mg_{0.1}PO₄ cathode materials for lithium rechargeable batteries. *Journal of applied electrochemistry*, 2009. 39(12): p. 2433-2438.
144. Gan, J. and A. Yu, DEM simulation of the packing of cylindrical particles. *Granular Matter*, 2020. 22(1): p. 1-19.

145. Jia, X. and R.A. Williams, A packing algorithm for particles of arbitrary shapes. *Powder technology*, 2001. 120(3): p. 175-186.
146. Rueda, M.M., et al., Rheology and applications of highly filled polymers: A review of current understanding. *Progress in Polymer Science*, 2017. 66: p. 22-53.
147. Paoella, A., et al., Etched colloidal LiFePO₄ nanoplatelets toward high-rate capable Li-ion battery electrodes. *Nano letters*, 2014. 14(12): p. 6828-6835.
148. German, R.M., *Particle packing characteristics*. 1989.
149. Smith, L. and P. Midha, Computer simulation of morphology and packing behaviour of irregular particles, for predicting apparent powder densities. *Computational materials science*, 1997. 7(4): p. 377-383.
150. Donev, A., et al., Unusually dense crystal packings of ellipsoids. *Physical review letters*, 2004. 92(25): p. 255506.
151. Chang, Z.-R., et al., Synthesis and characterization of high-density LiFePO₄/C composites as cathode materials for lithium-ion batteries. *Electrochimica Acta*, 2009. 54(20): p. 4595-4599.
152. Panduro, E.A.C., et al., A review of the use of nanofluids as heat-transfer fluids in parabolic-trough collectors. *Applied Thermal Engineering*, 2022: p. 118346.
153. Matusiak, J. and E. Grządka, Stability of colloidal systems-a review of the stability measurements methods. *Annales Universitatis Mariae Curie-Sklodowska, sectio AA-Chemia*, 2017. 72(1): p. 33.
154. Fritz, G., et al., Electrosteric stabilization of colloidal dispersions. *Langmuir*, 2002. 18(16): p. 6381-6390.

155. Wei, W., et al., The effect of graphene wrapping on the performance of LiFePO₄ for a lithium ion battery. *Carbon*, 2013. 57: p. 530-533.
156. Bijlard, A.C., et al., Functional colloidal stabilization. *Advanced Materials Interfaces*, 2017. 4(1): p. 1600443.
157. Farn, R.J., *Chemistry and technology of surfactants*. 2008: John Wiley & Sons.
158. Rosen, M.J. and J.T. Kunjappu, *Surfactants and interfacial phenomena*. 2012: John Wiley & Sons.
159. Tadros, T.F., *Applied surfactants: principles and applications*. 2006: John Wiley & Sons.
160. Tiwari, S., C. Mall, and P. Prakash Solanki, Surfactant and its applications: A review. *Int. J. Eng. Res. Appl*, 2018. 8(9): p. 61-66.
161. Kresheck, G.C., *Surfactants, in Water a comprehensive treatise*. 1975, Springer. p. 95-167.
162. Salager, J.-L., *Surfactants types and uses. FIRP booklet*, 2002. 300.
163. Kong, H., et al., Surfactant modification of banana trunk as low-cost adsorbents and their high benzene adsorptive removal performance from aqueous solution. *RSC advances*, 2016. 6(29): p. 24738-24751.
164. Wulandari, R. and D. Siswanta, Adsorption of sodium dodecylbenzene sulfonate (DBS) by c-3, 4-di-methoxyphenylcalix [4] resorcinarene triphenylphosphonium chloride. *Jurnal Riset Teknologi Pencegahan Pencemaran Industri*, 2018. 9(1): p. 1-8.
165. Soleimani Zohr Shiri, M., W. Henderson, and M.R. Mucalo, A review of the lesser-studied microemulsion-based synthesis methodologies used for

preparing nanoparticle systems of the noble metals, Os, Re, Ir and Rh. *Materials*, 2019. 12(12): p. 1896.

166. Prince, S.J., Stability and sorption characteristics of alkylbenzyltrimethylammonium chlorides used for ophthalmic and topical formulations. 1996: The University of Oklahoma Health Sciences Center.
167. Liu, G., et al., Application of surfactants in commercial crop production for water and nutrient management in sandy soil. 2014.
168. Li, Q., et al., Surfactants assisted synthesis of nano-LiFePO₄/C composite as cathode materials for lithium-ion batteries. *Journal of Materials Chemistry A*, 2015. 3(5): p. 2025-2035.
169. Di Lupo, F., et al., Surfactant-assisted mild solvothermal synthesis of nanostructured LiFePO₄/C cathodes evidencing ultrafast rate capability. *Electrochimica Acta*, 2015. 156: p. 188-198.
170. Gao, Y., et al., Surfactant assisted solvothermal synthesis of LiFePO₄ nanorods for lithium-ion batteries. *Journal of energy chemistry*, 2017. 26(3): p. 564-568.
171. Huang, Y., et al., Tween40 surfactant effect on the formation of nano-sized LiFePO₄/C powder via a solid state reaction and their cathode properties. *Solid State Ionics*, 2013. 249: p. 158-164.
172. Khan, S., et al., Surfactant-mediated and morphology-controlled nanostructured LiFePO₄/carbon composite as a promising cathode material for Li-ion batteries. *ChemistryOpen*, 2020. 9(1): p. 23-31.
173. Luo, W.-B., et al., Self-assembled graphene and LiFePO₄ composites with superior high rate capability for lithium ion batteries. *Journal of Materials Chemistry A*, 2014. 2(14): p. 4927-4931.

174. Atkin, R., et al., Mechanism of cationic surfactant adsorption at the solid–aqueous interface. *Advances in colloid and interface science*, 2003. 103(3): p. 219-304.
175. Li, R., et al., Study on the assembly structure variation of cetyltrimethylammonium bromide on the surface of gold nanoparticles. *ACS omega*, 2020. 5(10): p. 4943-4952.
176. Kim, J. and O.J. Martin, Surfactants Control Optical Trapping near a Glass Wall. *The Journal of Physical Chemistry C*, 2021. 126(1): p. 378-386.
177. Lim, J., et al., Surface modification of citrate-capped gold nanoparticles using CTAB micelles. *Bulletin of the Korean Chemical Society*, 2014. 35(8): p. 2567-2569.
178. Tyrode, E., M.W. Rutland, and C.D. Bain, Adsorption of CTAB on hydrophilic silica studied by linear and nonlinear optical spectroscopy. *Journal of the American Chemical Society*, 2008. 130(51): p. 17434-17445.
179. Wang, W., et al., Adsorption and structural arrangement of cetyltrimethylammonium cations at the silica nanoparticle– water interface. *The Journal of Physical Chemistry B*, 2004. 108(45): p. 17477-17483.
180. Clogston, J.D. and A.K. Patri, Zeta potential measurement, in *Characterization of nanoparticles intended for drug delivery*. 2011, Springer. p. 63-70.
181. Larsson, M., A. Hill, and J. Duffy, Suspension stability; why particle size, zeta potential and rheology are important. *Annual transactions of the Nordic rheology society*, 2012. 20(2012): p. 6.
182. Lunardi, C.N., et al., Experimental methods in chemical engineering: Zeta potential. *The Canadian Journal of Chemical Engineering*, 2021. 99(3): p. 627-639.

183. Lowry, G.V., et al., Guidance to improve the scientific value of zeta-potential measurements in nanoEHS. *Environmental Science: Nano*, 2016. 3(5): p. 953-965.
184. Castillo, G., Z. Garaiova, and T. Hianik, *New Technologies for Nanoparticles Detection in Foods*. *Advances in Food Diagnostics*, 2017: p. 305-341.
185. Wojdyr, M., Open source GPL'd peak profiling program Fityk. *J Appl Crystallogr*, 2010. 43: p. 1126-1128.
186. Hunter, R.J., *Zeta potential in colloid science: principles and applications*. Vol. 2. 2013: Academic press.
187. Doroszkowski, A., *The physical chemistry of dispersion*. *Paint and Surface Coatings*; Elsevier: Amsterdam, The Netherlands, 1999: p. 198-242.
188. Berthomieu, C. and R. Hienerwadel, Fourier transform infrared (FTIR) spectroscopy. *Photosynthesis research*, 2009. 101(2): p. 157-170.
189. Çabuk, H., Y. Yılmaz, and E. Yıldız, A vortex-assisted deep eutectic solvent-based liquid-liquid microextraction for the analysis of alkyl gallates in vegetable oils. *Acta Chimica Slovenica*, 2019. 66(2): p. 385-394.
190. Kaewprasit, C., N. Abidi, and J.-P. Gurlot. Effect of adsorbed water on the specific surface area of some standards cotton. 1999.
191. Świder, J., et al., A novel concept for the synthesis of nanometric LiFePO₄ by co-precipitation method in an anhydrous environment. *Procedia Engineering*, 2014. 98: p. 36-41.
192. Zhang, L. and J. Cao, Pyrolysis and its mechanism of organomontmorillonite (OMMT) influenced by different functional groups. *Journal of Thermal Analysis and Calorimetry*, 2019. 137(1): p. 1-10.

193. Gim, J., et al., Pyro-synthesis of functional nanocrystals. *Scientific reports*, 2012. 2(1): p. 1-6.
194. Maldonado-Hódar, F., et al., Catalytic graphitization of carbon aerogels by transition metals. *Langmuir*, 2000. 16(9): p. 4367-4373.
195. Saravanan, M., et al., Ultrasonically controlled release and targeted delivery of diclofenac sodium via gelatin magnetic microspheres. *International journal of pharmaceutics*, 2004. 283(1-2): p. 71-82.
196. Fischer, K.E., et al., Biomimetic nanowire coatings for next generation adhesive drug delivery systems. *Nano letters*, 2009. 9(2): p. 716-720.
197. Vivero-Escoto, J.L., et al., Photoinduced intracellular controlled release drug delivery in human cells by gold-capped mesoporous silica nanosphere. *Journal of the American Chemical Society*, 2009. 131(10): p. 3462-3463.
198. Lung-Hao Hu, B., et al., Graphene-modified LiFePO₄ cathode for lithium ion battery beyond theoretical capacity. *Nature communications*, 2013. 4(1): p. 1-7.
199. Instruments, G., Basics of electrochemical impedance spectroscopy. G. Instruments, *Complex impedance in Corrosion*, 2007: p. 1-30.
200. Li, J., et al., In-situ growth of graphene decorations for high-performance LiFePO₄ cathode through solid-state reaction. *Journal of Power Sources*, 2014. 249: p. 311-319.
201. Liu, W., et al., Optimized performances of core-shell structured LiFePO₄/C nanocomposite. *Journal of Power Sources*, 2011. 196(18): p. 7728-7735.
202. Chen, R., Y. Wu, and X.Y. Kong, Monodisperse porous LiFePO₄/C microspheres derived by microwave-assisted hydrothermal process

- combined with carbothermal reduction for high power lithium-ion batteries. *Journal of Power Sources*, 2014. 258: p. 246-252.
203. Chen, Z., et al., Morphology control of lithium iron phosphate nanoparticles by soluble starch-assisted hydrothermal synthesis. *Journal of Power Sources*, 2014. 272: p. 837-844.
204. Ma, Z., et al., Tunable morphology synthesis of LiFePO₄ nanoparticles as cathode materials for lithium ion batteries. *ACS Applied Materials & Interfaces*, 2014. 6(12): p. 9236-9244.
205. Phadke, S., E. Coadou, and M. Anouti, Catholyte formulations for high-energy Li-S batteries. *The Journal of Physical Chemistry Letters*, 2017. 8(23): p. 5907-5914.
206. Wei, W., et al., Hierarchical LiFePO₄/C microspheres with high tap density assembled by nanosheets as cathode materials for high-performance Li-ion batteries. *Nanotechnology*, 2012. 23(47): p. 475401.
207. Li, Z., et al., [100]-Oriented LiFePO₄ nanoflakes toward high rate Li-ion battery cathode. *Nano letters*, 2016. 16(1): p. 795-799.
208. Iarchuk, A.R., et al., Influence of carbon coating on intercalation kinetics and transport properties of LiFePO₄. *ChemElectroChem*, 2019. 6(19): p. 5090-5100.
209. Wang, Y., et al., High-Rate LiFePO₄ Electrode Material Synthesized by a Novel Route from FePO₄·4H₂O. *Advanced Functional Materials*, 2006. 16(16): p. 2135-2140.
210. Lang, X., et al., The influence of treatment in a sulfur environment on the electrochemical performance of LiFePO₄ as a cathode material for lithium-ion batteries. *Journal of Alloys and Compounds*, 2018. 739: p. 536-541.

211. Salah, A.A., et al., FTIR features of lithium-iron phosphates as electrode materials for rechargeable lithium batteries. *Spectrochimica Acta Part A: Molecular and Biomolecular Spectroscopy*, 2006. 65(5): p. 1007-1013.
212. Huang, X., et al., Reaction mechanisms on solvothermal synthesis of nano LiFePO₄ crystals and defect analysis. *Industrial & Engineering Chemistry Research*, 2017. 56(38): p. 10648-10657.
213. Caccamo, M. and S. Magazù, Thermal restraint on PEG-EG mixtures by FTIR investigations and wavelet cross-correlation analysis. *Polymer Testing*, 2017. 62: p. 311-318.
214. Shukla, N., et al., FTIR study of surfactant bonding to FePt nanoparticles. *Journal of Magnetism and Magnetic materials*, 2003. 266(1-2): p. 178-184.
215. Orliukas, A.F., et al., SEM/EDX, XPS, and impedance spectroscopy of LiFePO₄ and LiFePO₄/C ceramics. *Lithuanian Journal of Physics*, 2014. 54(2).
216. Jegal, J.-P., et al., A lithium iron phosphate/nitrogen-doped reduced graphene oxide nanocomposite as a cathode material for high-power lithium ion batteries. *Journal of Materials Chemistry A*, 2014. 2(25): p. 9594-9599.
217. Cabán-Huertas, Z., et al., Aqueous synthesis of LiFePO₄ with fractal granularity. *Scientific reports*, 2016. 6(1): p. 1-9.
218. Rigamonti, M.G., et al., LiFePO₄ spray drying scale-up and carbon-cage for improved cyclability. *Journal of Power Sources*, 2020. 462: p. 228103.
219. Burba, C.M. and R. Frech, Raman and FTIR spectroscopic study of Li_xFePO₄ (0 ≤ x ≤ 1). *Journal of the Electrochemical Society*, 2004. 151(7): p. A1032.

220. Kretschmer, K., et al., Scalable Preparation of LiFePO₄/C Nanocomposites with sp²-Coordinated Carbon Coating as High-Performance Cathode Materials for Lithium-Ion Batteries. *ChemElectroChem*, 2015. 2(12): p. 2096-2103.
221. Wu, X.-L., et al., LiFePO₄ nanoparticles embedded in a nanoporous carbon matrix: superior cathode material for electrochemical energy-storage devices. *Adv. Mater*, 2009. 21(25-26): p. 2710-2714.
222. Claramunt, S., et al., The importance of interbands on the interpretation of the Raman spectrum of graphene oxide. *The Journal of Physical Chemistry C*, 2015. 119(18): p. 10123-10129.
223. Nakamura, T., et al., Structural and surface modifications of LiFePO₄ olivine particles and their electrochemical properties. *Journal of the Electrochemical Society*, 2006. 153(6): p. A1108.
224. Zheng, Z., et al., Porous Li₂FeSiO₄/C nanocomposite as the cathode material of lithium-ion batteries. *Journal of Power Sources*, 2012. 198: p. 229-235.

APPENDIX

A. Suspension Properties of the Dilute (0.01 wt. % LFP) and Concentrated (0.1 wt. % LFP) LFP-CTAB Systems

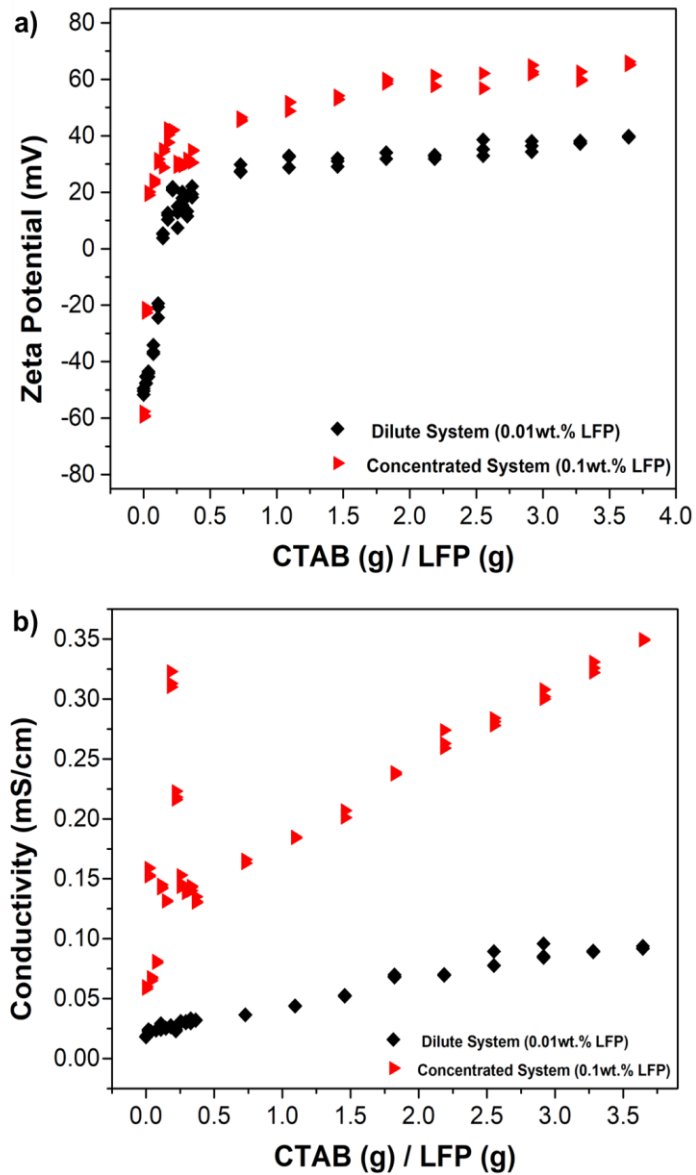


Figure A.1. Changes in a) Zeta Potential and b) Conductivity of the Dilute (0.01 wt.% LFP) and Concentrated (0.1 wt. % LFP) LFP-CTAB Suspension System



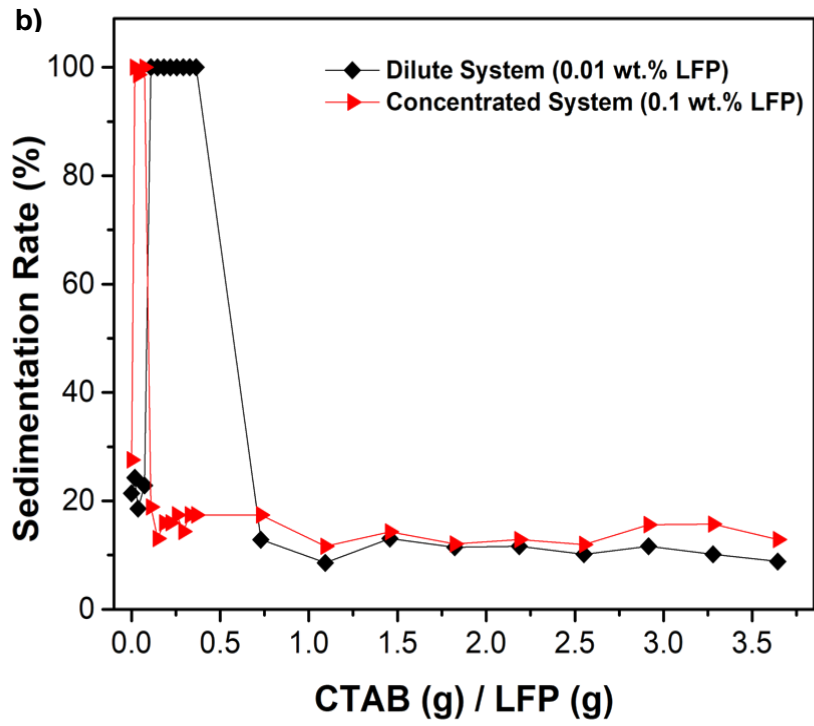


Figure A.2. a) Measurement of Sedimentation Length using ImageJ Software, b) Sedimentation Rate of the Dilute (0.01 wt.% LFP) and Concentrated (0.1 wt. % LFP) LFP-CTAB Suspension System

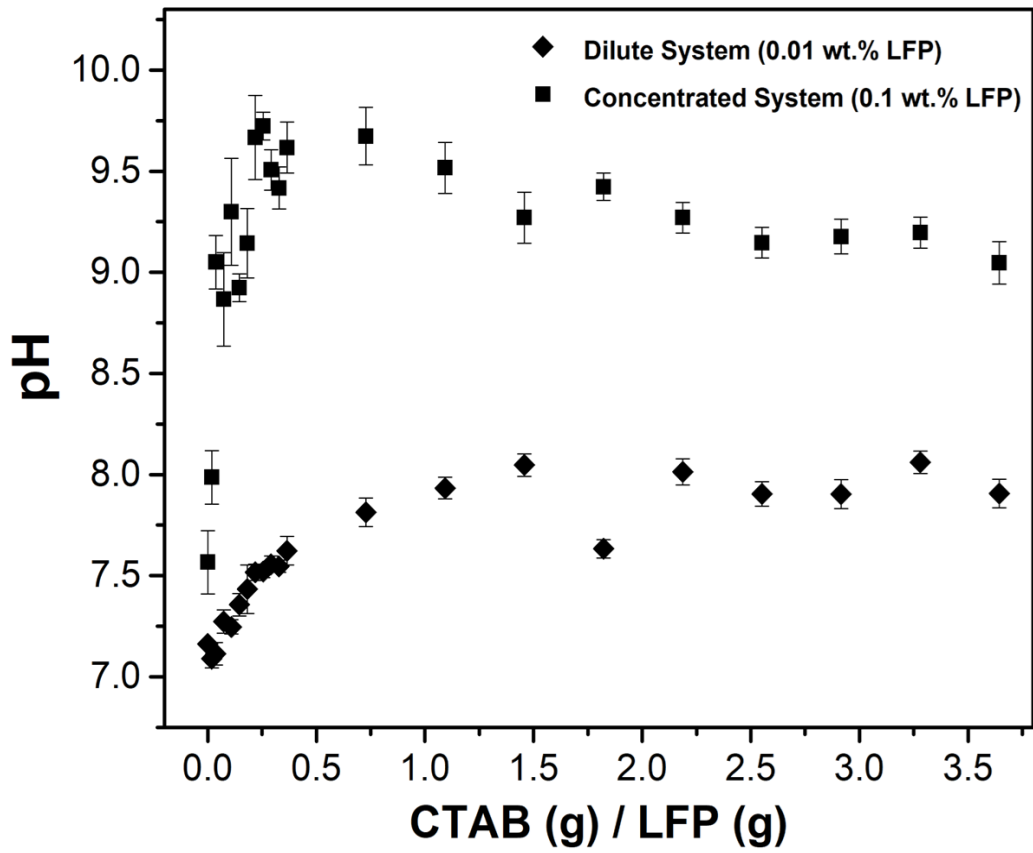


Figure A.3. pH changes in the Dilute (0.01 wt.% LFP) and Concentrated (0.1 wt. % LFP) LFP-CTAB Suspension System